Diss. ETH No. 20953

Interaction between quantum dots and superconducting microwave resonators

A dissertation submitted to
ETH ZURICH

for the degree of
Doctor of Sciences

presented by

Tobias Sebastian Frey

MSc ETH Physics
born June 15, 1983
citizen of Germany

accepted on the recommendation of:

Prof. Dr. Klaus Ensslin, examiner
Prof. Dr. Andreas Wallraff, co-examiner
Prof. Dr. Gerd Schön, co-examiner
Prof. Dr. Thomas Ihn, co-examiner

January 2013

Abstract

The realization of circuit quantum electrodynamics has created significant progress in the control and the coupling of microwave photons and superconducting qubits by trapping photons in an on-chip cavity. At the same time, research on quantum dots has led to an increase of the understanding and the possibility of manipulating single charge and spin states in experiments in a solid state environment.

In this thesis the coupling between the electromagnetic field of a superconducting coplanar waveguide resonator and semiconductor quantum dots is explored in detail. We discuss the design of the chip layout and present the development of the sample processing using different micro- and nanometer fabrication techniques for our samples, combining these two systems on one chip. A setup is built for the measurements, performed at cryogenic temperatures, to investigate the sample both at microwave frequencies and in the sub-kHz regime.

In a first experiment, the dependence of the transport properties through the quantum dot on the microwave field in the resonator is used to characterize the resonator with the quantum dot signal.

Furthermore a double quantum dot is investigated by measuring the transmission signal of the microwave resonator while varying gate voltages. The coupling to the resonator is used to record the double dot charge stability diagram, normally obtained with direct current measurements through the quantum dot or with charge detection techniques.

The interaction between the quantum dot system and the microwave resonator also allows us to explore finite frequency specific quantum dot physics. Using the GHz frequency resonator as a probe, we are able to characterize the complex admittance of a quantum dot coupled to its lead. We find that the sign of the reactance changes depending on the ratio between the excitation frequency and the tunnel coupling strength. The interpretation of the observations is based on a scattering matrix model.

We investigate the resonator quantum dot system in the vicinity of an interdot charge transfer line for different detunings and tunnel coupling strengths between the charge states of the quantum dots. Along the interdot charge transfer line two quantum dot energy levels are degenerate and an additional electron is either in the bonding or anti-bonding state of the double quantum dot forming the principal building block for a charge qubit. The measurements can be well described with master equation simulations based on the Jaynes-Cummings Hamiltonian. The modelling of the experimental results allows us to evaluate the coupling strength between the two systems and to estimate the dissipation and dephasing rates of the charge states.

Zusammenfassung

Die Realisierung der Quantenelektrodynamik basierend auf elektrischen Schaltkreisen hat bedeutenden Fortschritt in der Kontrolle und der Kopplung von Mikrowellenphotonen und supraleitenden Qubits gebracht. Dazu wurden auf dem gleichen Chip Qubits und Resonatoren für die Photonen realisiert. Zur gleichen Zeit hat die Forschung an Quantenpunkten zu einer Zunahme des Verständnisses einzelner Ladungs- und Spinzustände in einem Festkörper geführt und ermöglicht sie im Experiment gezielt zu beeinflussen.

In der vorliegenden Doktorarbeit wird die Kopplung zwischen einem solchen Resonator und einem Halbleiterquantenpunkt im Detail untersucht. Die Anordnung und das Aussehen der einzelnen Komponenten der Chips und die Entwicklung der zugehörigen Fabrikationsprozesse, die für unsere Proben verschiedene Mikrometer- und Nanometer- Fabrikationstechniken umfassen, um die beiden Systeme auf einem Chip zu realisieren, wird beschrieben.

Im Zuge der Doktorarbeit ist ein Messplatz gebaut worden, um die Proben sowohl im Mikrowellenfrequenzbereich als auch im sub-kHz Bereich zu untersuchen.

In einem ersten Experiment benutzen wir die Abhängigkeit der Transporteigenschaften durch den Quantenpunkt vom Mikrowellenfeld im Resonator, um den Resonator mit Hilfe des Quantenpunktsignals zu charakterisieren.

Des Weiteren wird ein Quantenpunkt mit Hilfe des Resonatortransmissionssignals untersucht. Die Kopplung zum Resonator wird verwendet, um das Ladungsstabilitätsdiagramm zu messen, das normalerweise durch die Aufzeichnung des Stroms durch den Quantenpunkt oder mittels Ladungsdetektionstechniken erhalten wird.

Die Wechselwirkung zwischen einem Quantenpunkt und dem Mikrowellenresonator erlaubt uns auch Eigenschaften des Quantenpunkts bei endlicher Frequenz zu untersuchen. So können wir mit Hilfe des Resonators die komplexe Impedanz eines Quantenpunkts, der an seine Zuleitung tunnelgekoppelt ist, charakterisieren. Als Ergebnis finden wir, dass das Vorzeichen des Blindwiderstandes sich in Abhängigkeit des Verhältnisses zwischen Anregungsfrequenz und Tunnelkopplungsstärke ändert. Die Interpretation der Beobachtungen basiert auf einem Streumatrixmodell.

Wir untersuchen das Quantenpunkt-Resonator-System in der Umgebung der Interdottunnelkopplungslinie für unterschiedliche Verstimmungen zwischen den Energieniveaus der Quantenpunkte und für unterschiedliche Tunnelkopplungsstärken zwischen den Quantenpunkten. Entlang der Interdottunnelkopplungslinie sind zwei Ladungszustände in den Quantenpunkten entartet und ein zusätzliches Elektron befindet sich entweder im bonding oder anti-bonding Zustand des Doppelquantenpunkts, was die Grundlage eines Ladungsqubits bildet. Die Messungen können sehr gut mit Hilfe einer Mastergleichungssimulation, die auf dem Jaynes-Cummings Hamilton Operator beruht, beschrieben werden. Die Modellierung der experimentellen Resultate erlaubt uns, die Kopplungsstärke zwischen den beiden Systemen und die Dissipations- und Dephasierungsraten des Ladungszustandes abzuschätzen.

Contents

Lists of symbols

Abbreviation	Explanation
2DEG	two dimensional electron gas
AC	alternating current
ADC	analog to digital converter
AFM	atomic force microscope
AWG	arbitrary waveform generator
BW	bias window
C	top gate contact
D	drain contact
DC	direct current
FPGA	field programmable gate array
HEMT	high electron mobility transistor
IVC	current to voltage converter
LAO	local anodic oxidation
LD	left quantum dot
LO	local oscillator
MBE	molecular beam expitaxy
MWG	microwave generator
MX	microwave mixer
M,N	M electron in LD and N in RD
O	ohmic contact
PAT	photon assisted tunneling
PCB	printed circuit board
QD	quantum dot
QED	cavity quantum electrodynamics
QPC	quantum point contact
R	microwave resonator
RD	right quantum dot
RF	radio frequency
RWA	rotating wave approximation
S	source contact
SP	microwave splitter

Symbol	Explanation
$\hat{\cdot}$	operator
α_{x}	lever arm of gate x
γ	tunneling coupling energy between dot and lead
γ_1	energy relaxation rate
γ_{φ}	pure dephasing rate
Δ	detuning between the resonator and the two level system
δ	energy detuning between the two quantum dots
$\delta\nu$	full width at half maximum
ε	mean energy of the two quantum dots
$\sigma_{\mathrm{x,y,z}}$	Pauli matrices
κ	line width of the resonator
λ	wavelength
l_{ϕ}	phase coherence length
ϕ	phase of the microwave signal
Υ	single particle level spacing
μ	electrochemical potential
ν	frequency
ν_{x}	resonance frequency of the x^{th} mode
ν_{q}	transition frequency between double dot charge states
ω	angular frequency
A	microwave signal amplitude
C_{Σ}	self-capacitance
C_{x}	capacitive coupling of gate x
c	capacitance per length
D	drain contact
d	diameter
E_{c}	charging energy
E_{IC}	interdot charging energy
G	conductance
g	coupling strength between resonator and two level system
I	current, microwave field quadrature
L	length
L_0	insertion loss
Q	microwave field quadrature
Q_{L}	loaded quality factor
Q_{ext}	external quality factor
Q_{int}	internal quality factor

Symbol	Explanation
r	radius
R_t	tunneling resistance
S	density spectrum, source contact
s	scattering matrix
T	system temperature
T_e	electron temperature
t	interdot tunneling coupling energy
V	voltage

physical constants	explanation
a_B	Bohr radius
$\mathrm{e}> 0$	elementary charge
ϵ	dielectric permittivity
ϵ_0	vacuum dielectric constant
$h = 2\pi\hbar$	Planck's constant
k_B	Boltzmann constant

Chapter 1

Introduction

> *"Zwei Dinge erfüllen das Gemüt mit immer neuer und zunehmender Bewunderung und Ehrfurcht, je öfter und anhaltender sich das Nachdenken damit beschäftigt: Der gestirnte Himmel über mir und das moralische Gesetz in mir."*
>
> Immanuel Kant: Kritik der praktischen Vernunft (1788).

Research on semiconductor nanostructures has contributed significantly to the understanding of the physics of charges and spins in a solid state environment [1–3].

Experiments on transport measurements through quantum dots [4, 5] revealed shell structure, as known from atomic physics, when adding electrons one by one to the dot [6]. Quantum dots are therefore often referred to as artificial atoms. They were also used to study the interaction of light and charge being one of the most fundamental processes in physics. In this context, resonant absorption of photons by electrons localized in a quantum dot has been explored in transport measurements of photon assisted tunneling (PAT) [7, 8].

As individual electrons do not only carry charge but also spin, quantum dots allow the study of spin physics [3]. For example experiments manipulating and reading out single spins gave insight into their coherence properties [9, 10]. Spin dephasing times exceeding 200 μs using a spin-echo sequence could be achieved in quantum dots fabricated on GaAs heterostructures [11] proving the large amount of control on a single spin embedded in a solid state environment.

Cavity quantum electrodynamics (QED), the study of the coupling of matter to light confined in a cavity [12], is traditionally studied with atoms. The spectrum of the light is given by the quantized eigenstates of the field modes and depends on the confinement caused by the cavity. If the energy of one of these field modes is close to or at the transition energy of two states in the atom, the interaction between the two systems can be investigated. The different field modes are well described by a set of harmonic oscillators with different energies and the behavior of the two involved states of the atom can be mapped to that of a spin. Thus in essence cavity

QED physics deals with phenomena related to the interaction between spins and oscillators [13].

In the literature experiments for two distinct parameter settings, named the strong coupling and the perturbative regime of cavity quantum electrodynamics, are discussed [13]. In the strong coupling regime the coupling strength between the quantized electromagnetic field and the atom is larger than the decay and dephasing rates of the quantum mechanical state of the atom and the decay rate of the photons from the cavity. This allows the observation of vacuum Rabi mode splitting [14]. In the perturbative coupling regime the coupling strength between the atom and the photons is smaller than at least one of the other relaxation parameters in the system. Here effects like the increase of the spontaneous decay rate of the atom state inside the cavity, the Purcell effect, was studied [15].

Cavity QED has not only been studied with atoms but has also been investigated in solid state systems such as self-assembled quantum dots [16]. The strong coupling regime could be achieved with quantum dots of this kind and cavities for photons in the nm regime [17, 18].

Furthermore, the realization of circuit QED [19], in which a single microwave photon is trapped in an on-chip cavity and coherently coupled to a quantum two-level system, has led to major advances in the study and control of the interaction between microwave photons and superconducting qubits. In this field of research experiments related to quantum computing were performed [20–23], but also quantum optics experiments on a chip [24] were demonstrated. Combining the ideas developed for circuit QED experiments with semiconductor quantum dots opens up the possibility to explore and engineer the interaction between single electrons or even single spins with single microwave photons in a solid state environment.

In this thesis, we describe the design, fabrication and investigation of devices in which semiconductor quantum dots are coupled to a GHz-frequency high-quality transmission line resonator. So far laterally defined quantum dots have typically been investigated by direct current (DC) transport measurements [4] or by using quantum point contacts for charge sensing [25]. Large bandwidth and low noise detection are harnessed by using radio frequency (RF) techniques, e.g., for charge sensing [26–29] or quantum capacitance measurements [30].

Our novel approach of combining semiconductor quantum dots with superconducting microwave resonators allows us to characterize the properties of the double quantum dot by measuring both its dispersive and dissipative interaction with the resonator. In addition to providing a new readout mechanism, this architecture has the potential to isolate the dots from the environment and to provide long distance coupling between spatially separated dots. These features are expected to improve the feasibility of a quantum information processor [31] consisting of hybrid systems. They have the potential advantage to allow the combination of the best features of every system, such as a long relaxation time e.g. of spin qubits [32, 33] and interaction between distant qubits mediated by a superconducting resonator as previously demonstrated in circuit QED experiments [34, 35]. A number of proposals to use microwave frequency techniques for scaling of quantum information processing architectures based on quantum dots have been put forward recently [36–39].

Quantum dot-resonator samples are however not only suitable to work towards hybrid quantum computing, but also to address basic topics of physics related to the tunneling of a particle through a potential barrier which is a fundamental consequence of quantum mechanics [40]. Research on transport experiments in semiconductor quantum dots relies on the tunnel effect as a requirement to measure a charge current through these devices. The transmission of the tunnel barriers themselves can be investigated in detail over orders of magnitude e.g. by counting electrons entering and leaving the quantum dot with a nearby charge detector [26, 41]. The properties of quantum dots coupled via a tunnel barrier to the leads can not only be studied with direct current (DC) bias [42], but also at finite frequency, measuring the complex admittance [43, 44]. This gives information about the dynamics of the electrons in the system. In this thesis we use the microwave resonator as a meter to study the dynamics of an electron wavefunction in the quantum dot which is tunnel coupled to the lead. In particular we investigate the relation between the quantum dot lead coupling strength and the measurement frequency.

This thesis is structured in 8 chapters and the appendix. We start with a discussion about the basic properties of single and double quantum dot physics in chapter 2. The fabrication of the samples and the design and construction of a new setup for the characterization of the devices are presented in chapter 3. In addition to the quantum dots, superconducting microwave resonators are the second key component of our chips and their development and characteristics on a GaAs substrate are presented in chapter 4. In chapter 5 first measurements of the interaction between the two systems are discussed. The coupling is used to characterize the microwave resonator with the nearby quantum dot. The following two chapters discuss the measurements of quantum dot properties with the on-chip microwave resonator. In chapter 6 we focus on the coupling between a lead and the quantum dot, measure the complex admittance and discuss the data using a scattering matrix approach. In chapter 7 the interdot coupling is investigated in detail with the microwave resonator. The data is interpreted using the Jaynes-Cummings model with the double quantum dot considered as a two level system and the microwave resonator as a harmonic oscillator with a single mode. The final chapter 8 summarizes the work, relates it to other experiments and gives an outlook for future experiments. In the appendix we discuss three sets of preliminary results obtained in this thesis. First microwave measurements of double quantum dots at finite bias are presented followed by microwave measurements of the double dot charge stability diagram for very small tunnel coupling to the leads. At last we discuss first measurements and design considerations which were already undertaken towards future experiments with single electron double quantum dots and resonators.

Chapter 2

Basic concepts and theoretical background

In this chapter the basic concepts of quantum dot physics, required for the understanding of the thesis, are explained. In particular the focus is on lateral quantum dots defined by nanofabrication techniques and investigated by charge transport measurements. In section 2.1 a brief introduction of single quantum dots is given comprising a discussion of the relevant energy scales in these systems. This elucidation is followed up by section 2.2 dealing with the properties of double quantum dots. As research with quantum dots has a large variety of aspects only the relevant basics are covered in this chapter. The interested reader is referred to review articles [2, 4, 5] and books [1, 45] for more details which also served as reference for this chapter.

2.1 Single quantum dots

Quantum dots are formed by confining electrons in all three spatial dimensions on a small island coupled only weakly to the surrounding environment. Typical diameters for lateral quantum dots defined by nanofabrication techniques, which are used in this thesis, are on the order of 100 nm. Quantum dots can display a variety of phenomena, e.g. the loading of an additional electron on the island is detectable, and in the following the conditions under which they arise are presented.

We begin by discussing the electric circuit representation of a single quantum dot as shown in Fig. 2.1 (a) to get an intuitive picture allowing us to understand the basic phenomena arising in transport measurements through quantum dots. The quantum dot is modeled as an island connected to the source (S) and drain contact (D) via two tunnel barriers which allow exchange of electrons. The tunnel barriers are modeled as a combination of a resistor and a capacitor and their characteristics like the transmission are tunable with voltages (V_L and V_R). In addition, the electrostatic potential on the dot can be tuned with a gate voltage (V_PG) represented in Fig. 2.1 (a) with a capacitor connected to the dot.

If we apply a small source-drain voltage (V_{SD}) and measure the current through the sample as a function of the gate voltage (V_{PG}), a discrete set of peaks in the current can be observed (Fig. 2.1 (b)). The current peaks are named conductance resonances and the spaces in between are caused by Coulomb blockade arising due to Coulomb interaction between the electrons on the islands.

In order to be able to measure such current traces, two requirements have to be fulfilled. First the charging energy $E_{\mathrm{C}} = e^2/C_\Sigma$ (C_Σ is the self-capacitance of the dot) when adding one electron on the dot has to be much larger than the thermal energy ($k_{\mathrm{B}}T_{\mathrm{e}}$) of the electrons

$$e^2/C_\Sigma \gg k_{\mathrm{B}}T_{\mathrm{e}}. \tag{2.1}$$

Here the charging energy E_{C} is introduced as the difference in energy between adding an extra electron onto the quantum dot island being already occupied with N or $N-1$ electrons respectively, following the definition used in Ref. [1].

Second the coupling to the leads has to be small enough, for resolving the quantization of charges on the island,

$$R_{\mathrm{t}} \gg \frac{h}{e^2}, \tag{2.2}$$

where R_{t} is the tunneling resistance.

If the current as a function of the plunger gate voltage (Fig. 2.1 (b)) is measured for several different source-drain voltages, so-called Coulomb diamonds are obtained as shown in Fig. 2.1 (c). In Fig. 2.1 (d-g) sketches of the energy levels of the dot (μ_{N}) with respect to the leads for different positions in the Coulomb diamond diagram are displayed. Note that for simplicity we do not consider the temperature broadening of the Fermi distribution function here.

At position (d) the Fermi energy in the two leads ($\mu_{\mathrm{S}}, \mu_{\mathrm{D}}$) is aligned with one of the energy levels in the quantum dot, allowing one electron at a time to tunnel from either lead into the dot and out again. In situation (e) however, located inside a diamond, no energy level for adding an electron to the quantum dot is available in the energy range spanned by the difference of the two Fermi distribution functions of the electrons in the source and drain lead. In this situation the dot is in the so-called Coulomb blockade. The difference between the two Fermi distribution functions is termed bias window (BW) as indicated in Fig. 2.1 (f). In the same sketch the Fermi level of the drain lead (μ_{D}) is aligned with an energy level in the quantum dot (μ_{N}). This configuration ($\mu_{\mathrm{D}} = \mu_{\mathrm{N}}$) forms one of the boundaries of the diamond pattern. The other limit of the diamond pattern is reached when the Fermi level in the source contact (μ_{S}) is aligned with a dot energy level (μ_{N}) as depicted in part (g) of Fig. 2.1.

The extent of the diamonds in source-drain voltage is a direct measure of the charging energy (E_{C}). The voltage difference (ΔV_{PG}) between two Coulomb resonances can be converted into an energy using the corresponding lever arm of the

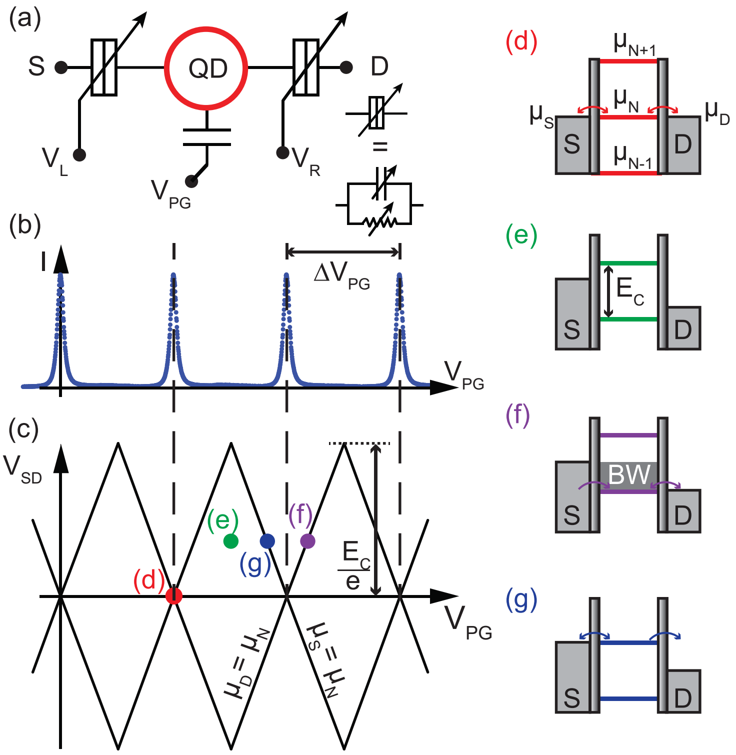

Figure 2.1: (a) Electric circuit representation of a single quantum dot. The tunnel barriers are modeled using resistors and capacitors tunable with gate voltages V_L, V_PG and V_R. Source contact (S) and drain contact (D) allow the measurement of a charge current through the quantum dot. (b) Schematic of Coulomb resonances in dependence on applied plunger gate voltages (V_PG). (c) Schematic of Coulomb diamonds typical for the charge stability diagram of a single quantum dot. E_C labels the charging energy. μ_S, μ_N and μ_D are the chemical potentials of the source lead, the quantum dot and the drain lead respectively. (d-g) Schematics of the single quantum dot for different gate voltage settings. Arrows indicate tunneling processes of electrons. (d) Coulomb resonance situation at zero source-drain bias. (e) Coulomb blockade setting with a small bias applied. (f, g) Finite bias situation for $\mu_\mathrm{N} = \mu_\mathrm{D}$ (f) and $\mu_\mathrm{N} = \mu_\mathrm{S}$ (g). *BW* labels the so called bias window which is the difference in energy spanned by μ_S and μ_D.

plunger gate (α_PG) which is defined as:

$$\alpha_\mathrm{PG} = \frac{|V_\mathrm{SD}|}{|\Delta V_\mathrm{PG}|}. \tag{2.3}$$

Another energy scale which was not discussed so far is the single-particle level spacing Υ. Energy levels with a spacing of Υ arise because of the confinement of the electrons on the island. A requirement to be able to resolve charge transport through excited states is that the thermal energy of the electrons ($k_\mathrm{B}T_\mathrm{e}$) is much smaller than the single particle level spacing.

Whether the charging energy or the single-particle level spacing is dominant depends on the size of the quantum dots. The crossover can be estimated to be at a radius (r) of approximately 10 nm [1] for circular dots in GaAs. If the radius of the dot is much larger than this value the charging energy dominates whereas in the opposite case it is the single-particle level spacing. For the samples investigated in this thesis the charging energy is always larger than the single-particle level spacing. The presence of single-particle levels in the dot can be observed in transport measurements as additional steps in the current outside the diamonds. These current steps as a function of the applied voltages are also parallel to one of the boundaries of the Coulomb diamond.

2.2 Double quantum dots

After having dealt with the basic concepts within single quantum dot physics, we now proceed to discuss the properties of two quantum dots connected in series for zero source-drain voltage. First the emergence of the hexagon pattern in the charge stability diagram is discussed (Fig. 2.2 (a-c)), where in the top of each sub-figure (a-c) the electric circuit representation of the particular double quantum dot model is displayed and the corresponding charge stability diagram below. The presentation of the origin of the features in the charge stability diagram is followed by an investigation of the different quantum dot level configurations along the hexagon boundaries (Fig. 2.2 (d)).

We start with two single quantum dots with only a resistive connection between them as shown in the electric circuit representation in the top of Fig. 2.2 (a). The individual dots are tunnel coupled to either the source (S) or drain (D) contact and the electrostatic potential on each dot can be tuned by applying a voltage to the corresponding plunger gates (V_{LP}, V_{RP}). The charge stability diagram for this model treatment of the double quantum dot as a function of the two plunger gate voltages is displayed in Fig. 2.2 (a). It consists of vertical and horizontal lines. Along the horizontal lines a quantum dot energy level in the right dot (RD) is resonant with the drain lead whereas along the vertical lines the left dot (LD) is in resonance with the source lead. Only at the crossing of the two lines highlighted by red circles an energy level in the left dot is aligned with an energy level in the right dot and resonant electron transport can occur through the double quantum dot. These points are called triple-points. Within each rectangle the number of charge carriers is fixed indicated by the number (M,N).

As mentioned above, quantum dots are small objects on the order of 100 nm. Therefore the left (right) plunger gate has not only an electrostatic influence on the left (right) dot, but there is also a so-called cross-capacitance which tunes the right (left) dot at the same time, as indicated in Fig. 2.2 (b). The consequence for the charge stability diagram is that the horizontal and vertical lines are tilted and the slope is a measure for the cross coupling strength.

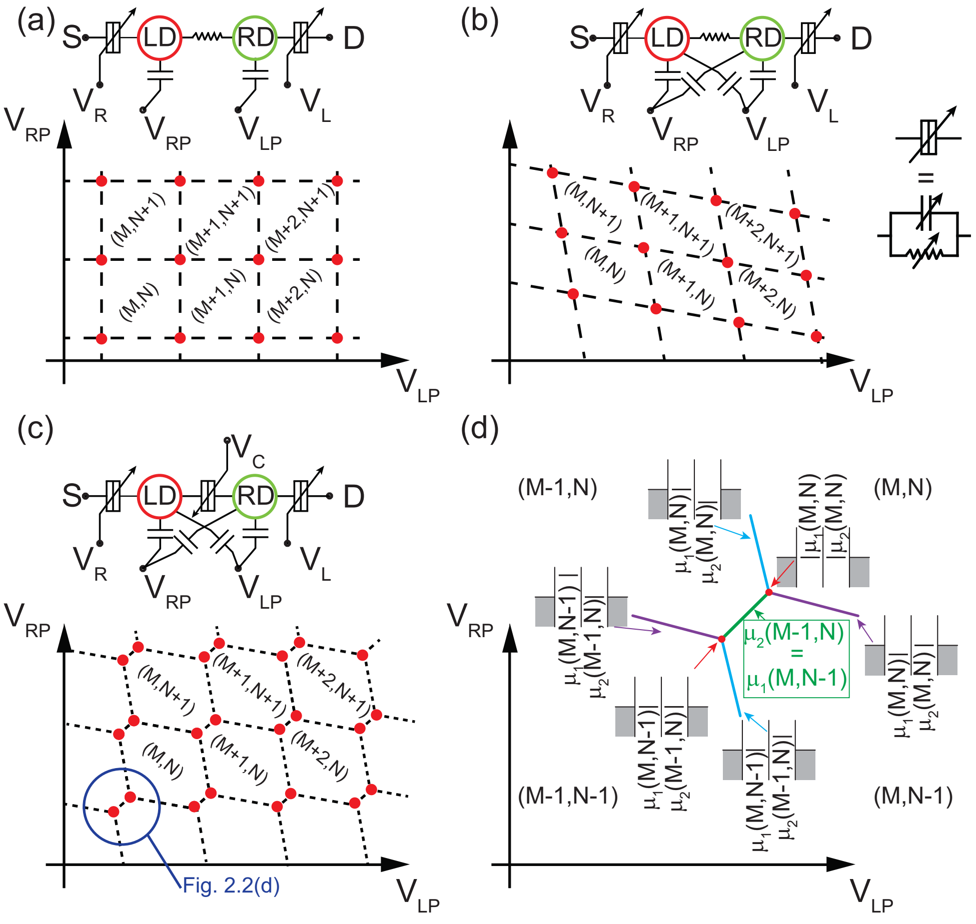

Figure 2.2: (a-c) Circuit representations of different double quantum dot models and schematics of the corresponding charge stability diagrams as a function of the two plunger gate voltages V_{LP} and V_{RP} . Red points label gate voltage configurations where elastic electron transport is possible. (M,N) label stable charge configurations. (a) Each dot is only capacitively coupled to its gate. (b) Each dot is capacitively coupled to both gates. (c) Both dots are capacitively coupled to each other. (d) Schematic of the charge stability diagram of a double dot for (M,N) electrons close to the two triple points as a function of V_{LP} and V_{RP}.

In reality it is not adequate to model the connection between the two quantum dots with a resistor because there is also a capacitive coupling between the two dots as depicted in Fig. 2.2 (c). As a result a new energy scale, the interdot charging energy (E_{IC}), comes into play in double quantum dot physics. If we consider the situation in which an energy level in the right and left dot each are resonant both with each other and the leads, and an extra electron is loaded into the left dot, then the interdot charging energy (E_{IC}) has to be overcome before it is possible to also load an electron into the right dot at the same time. The different electrostatic effects of the gates on the dots and the coupling between the dots lead to double dot charge stability diagrams consisting of hexagon structures (Fig. 2.2 (c)).

In Fig. 2.2 (d) a detailed view around two triple points, highlighted in red, is shown for zero source-drain voltage. Along the green line connecting the two triple points and referred to as the interdot charge transfer line, two quantum dot energy levels, one in each dot, are resonant with each other but not with the leads. Therefore transport is blocked here. In the case of a small tunnel coupling between the two dots ($\Gamma \ll k_{\mathrm{B}} T_{\mathrm{e}}$) the length of the interdot charge transfer line is set by the interdot charging energy. Along one set of parallel boundary lines (cyan lines in Fig. 2.2 (d)), the left dot is resonant with its neighboring lead, the source contact, but the right quantum dot is detuned from the drain contact as indicated with sketches in Fig. 2.2 (d). Correspondingly, for the other set of parallel lines (purple lines in Fig. 2.2 (d)) the right dot is resonant with its lead (drain contact) but the left dot is detuned from the source contact. In transport experiments these lines are often referred to as cotunneling lines. Along these lines, due to energy conservation, only higher order tunneling processes referred to as cotunneling [46] can take place in order for a current to flow through the double quantum dot. We come back to cotunneling processes in chapter 6.

For the case of a non-zero source-drain voltage, a bias window is opened in which current can flow through the double quantum dot. As a consequence a current through the double quantum dot can be measured not only at the triple points in the charge stability diagram but also within so called finite bias triangles developed around the triple points. The origin of the finite bias triangles is explained in more detail in Ref. [2] and corresponding data is presented in the appendix A.

Chapter 3

Sample fabrication and measurement setup

In order to realize experiments in which we study DC transport properties of quantum dots as well as the coupling between quantum dots and a microwave resonator (for details on the physics of resonators see chapter 4) we need to bring together the quantum dot device characteristics and the corresponding measurement setup with the technology used for superconducting microwave circuits. This involves developing fabrication methods for processing the 'hybrid' devices, as well as a measurement setup that allows to investigate these chips at microwave frequencies and in the sub-kHz regime.

In this chapter, we first discuss the different micro- and nanotechnology techniques used for the sample fabrication in this thesis. The rest of the chapter is devoted to the presentation of the different parts of the measurement setup.

3.1 Sample fabrication

In this section we describe the different fabrication steps required for the resonator quantum-dot samples. Optical lithography is the predominant technology used for the processing. The quantum dot structure itself, however, has to be defined with different means. Two methods for quantum dot processing implemented successfully for samples presented in this thesis are discussed: atomic force microscope (AFM) lithography and electron-beam defined split gate technology. The detailed fabrication instruction is given in the appendix D.

3.1.1 Optical lithography part of the chip processing

A typical example of a sample is shown in Fig. 3.1. It is designed to implement a quantum dot defined by AFM lithography. The position of the quantum dot, indicated with a red circle in Fig. 3.1, is chosen to be at an antinode of the electric field of a microwave transmission-line resonator. The chip is realized on a molecular

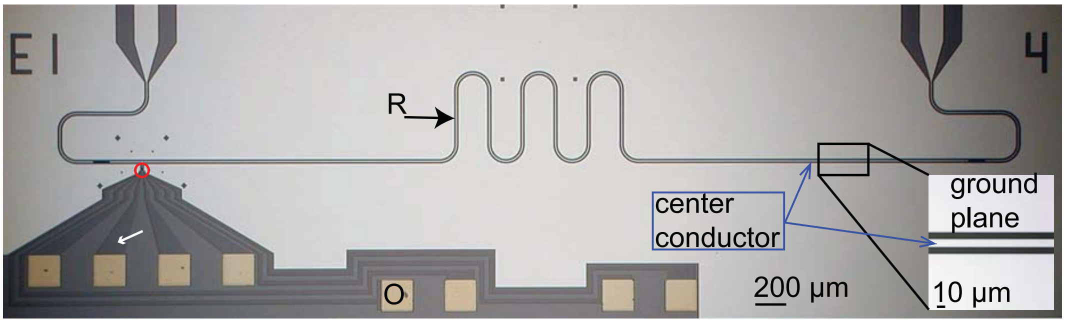

Figure 3.1: Optical image of a hybrid quantum device, consisting of a microwave resonator (R) and a mesa to define a quantum dot with atomic force microscope lithography, see text for details. Dark brown parts (example indicated with a white arrow) mark mesa regions with the two-dimensional electron gas (2DEG) present. Golden squares are ohmic contacts (O). Red circle indicates the position of the quantum dot. Inset: Zoom around the center conductor of the microwave resonator.

beam epitaxy (MBE) grown $Al_xGa_{1-x}As$ heterostructure [11] with a two-dimensional electron gas (2DEG) residing at the heterointerface about 35 nm below the surface referred to as shallow 2DEG in the following. All the experiments in this thesis are conducted using shallow 2DEGs except the measurement data shown in the appendix C. Here different wafer material with the 2DEG at a depth of around 90 nm from the surface is used.

To fabricate a sample such as the one shown in Fig. 3.1 we start with three stages of optical lithography. In the first lithography step, the mesa [47] for the quantum dot (dark brown parts, indicated with a white arrow in Fig. 3.1) is defined with a wet etching process. The etchant is a diluted piranha solution which is a mixture of water, sulfuric acid and hydrogen peroxide. The two-dimensional electron gas only remains at the position where later the quantum dot will be defined and at the connecting lines between the quantum dots and the contacts. In the rest of the chip it is removed by the etchant. The presence of the 2DEG everywhere on the chip would otherwise strongly dampen the resonator due to the interaction between the photons and the electrons in the 2DEG.

In the second stage the ohmic contacts (labeled O in Fig. 3.1) are fabricated by depositing a multilayer consisting of gold, germanium and nickel. In the following annealing step metal diffuses into the wafer material and contacts the 2DEG.

In the third stage the microwave resonator (R) is realized in coplanar waveguide technology [48] consisting of the center conductor, separated by two gaps from the ground plane (see inset in Fig. 3.1). The width of the center conductor (10 μm) and the gaps (7.1 μm) are chosen so that the microwave line has an impedance of 50 Ω and the length of the resonator ($\approx$ 8273 μm) to have the fundamental resonance frequency (ν_0) at around 7 GHz. The resonator is coupled to the input/output lines by two planar capacitors. We use a lift off process including a deposition of a bilayer of 3 nm titanium (Ti) and 200 nm aluminum (Al) for the fabrication of the resonator. More details on the design of the resonators are discussed in chapter 4. Note that for samples designed to implement a quantum dot using electron-beam defined split gate technology an additional optical lithography step is required to define the connecting lines for the split gates. An example of such a sample is shown in Fig. 6.1.

3.1.2 Quantum dot fabrication techniques

The principle of AFM lithography is the local oxidation of the wafer [41, 49, 50] resulting in a depletion of the underlying two-dimensional electron gas. A prerequisite for this method to work is a humidity in the AFM chamber of around 40% so that a thin water film is formed on the surface of the wafer. A negative voltage is applied to the tip of the AFM which was brought close to the surface of the wafer before. This leads to a local electrically conducting connection between the wafer and the tip mediated by the water film. Thus a current can flow between the AFM tip and the surface of the wafer causing local anodic oxidation (LAO) of the wafer surface. The AFM tip is moved along a predefined pattern to create semiconductor nanostructures. An AFM image of a single quantum dot defined with AFM lithography is shown in Fig. 3.2 (a). The yellowish lines are the oxide lines, separating the quantum dot from the four in-plane gates (G1-G4) which are used to tune the quantum dot electrostatically. Confining the 2DEG with oxide lines to small channels allows the formation of tunnel barriers which separate the source (S) and drain (D) contacts from the quantum dot. In Fig. 3.2 (b) a linecut through one of the oxide

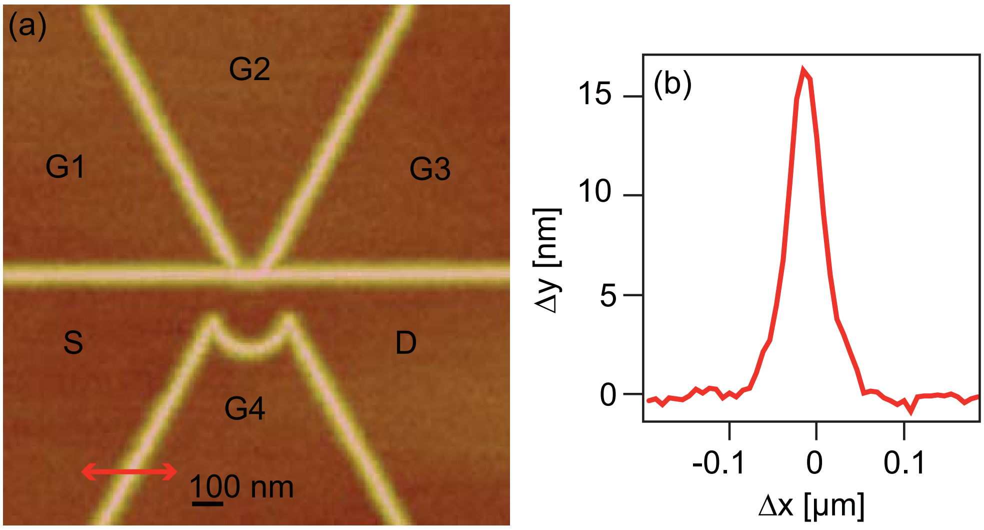

Figure 3.2: (a) Atomic force microscope (AFM) image of a single quantum dot with source (S) and drain (D) contacts and four gates (G1-G4). The bright lines are caused by the oxidation of the sample surface. (b) Height profile of an oxide line along the red arrow indicated in (a).

lines is shown. The typical height of the oxide lines achieved for the samples used in this thesis is around 15 nm. Approximately the same amount of material is also oxidized in the wafer and the 2DEG is depleted locally. The oxide lines typically start to leak when a voltage difference between 250 − 350 mV is applied.

The other nanolithography method applied in this thesis uses electron-beam lithography to fabricate split-gate defined quantum dots [51–53]. Here the quantum dot structure is defined using electron beam lithography in combination with a lift-off process depositing 3 nm of titanium (Ti) followed by 25 nm of gold (Au). An example of a split-gate defined double quantum dot is shown in Fig. 3.3. The appropriate potential to form the double quantum dot is achieved by applying negative voltages to the gate electrodes which leads to a depletion of the two dimensional electron gas (2DEG) underneath them and in their vicinity.

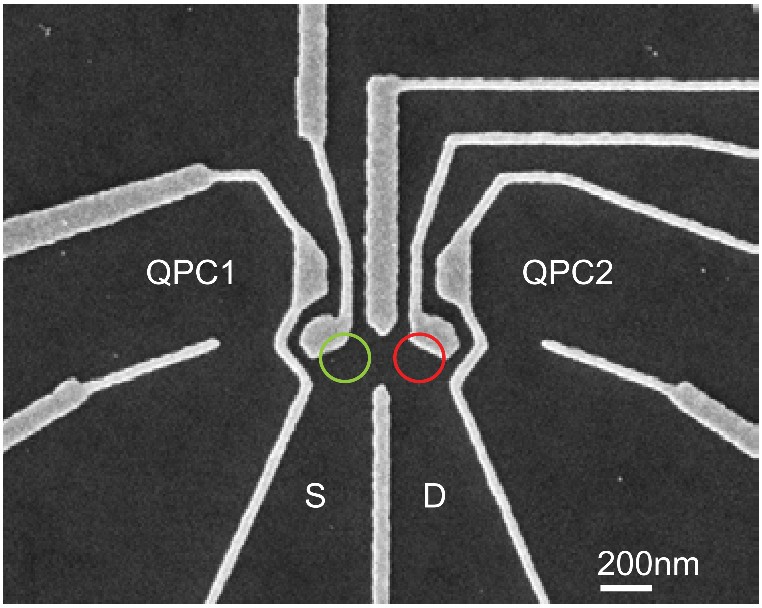

Figure 3.3: Scanning electron microscope picture of a double quantum dot sample (approximate locations of dots indicated by a red and a green circle). Metal gates are used to deplete the electron gas underneath the electrodes to form the potential landscape for a double quantum dot. The charge stability diagram of the double quantum dot can be recorded either by direct transport measurement through the source (S) and drain (D) contact or with charge detection techniques using one of the two quantum point contacts (QPC1, QPC2).

3.2 Measurement setup

In this section we describe the various parts of the measurement setup consisting of different microwave components that allow transmission measurements of the resonator and DC voltage sources, and current to voltage converters (IVCs) to characterize the sample with standard transport techniques. All experiments are performed in a dilution refrigerator [54] with a base temperature of around $10 - 20$ mK. The low temperature is necessary to be able to operate the resonator in its ground state ($k_{\mathrm{B}}T < \hbar\omega$) and to reach an electron temperature (T_{e}) as low as possible in order to minimize thermal broadening of the conductance resonances of the quantum dot. More details than presented in this section about the microwave components are found in Ref. [55] and a more detailed description of similar microwave setups can be found in Refs. [56, 57].

3.2.1 Printed circuit board

We designed printed circuit boards (PCBs) to mount the hybrid chips in the measurement setup. They serve as a link between the sample and the cabling in the fridge. Two photographs of the same printed circuit board from two different perspectives are shown in Fig. 3.4 (a,b). The printed circuit boards consist of a low loss dielectric (Ad1000, Arlon) sandwiched between two copper layers covered with a gold finish. The many vias, a conducting connection between the front and the backside of the PCB, assure a proper grounding. The sample is glued in the cut-out in the middle of the PCB and then bonded to the ground and the contacts of the PCB. The designed printed circuit boards enable us to connect up to five microwave lines. Microwave connectors are soldered to the board at two out of the possible five spots shown in Fig. 3.4 (a,b). In addition twelve direct current (DC) voltage

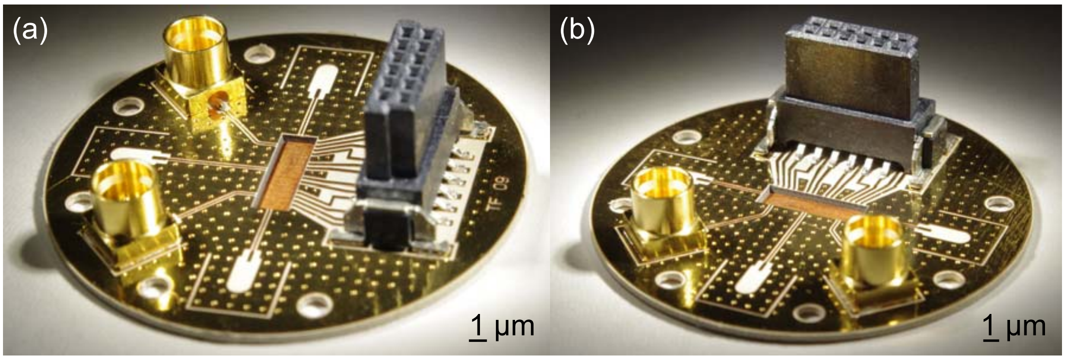

Figure 3.4: (a,b) Photographs of the printed circuit board (PCB) used to measure the hybrid quantum dot resonator chips. The PCB allows the connection of 12 direct current (DC) sources via the black plug. Moreover up to 5 microwave lines can be used for the microwave measurements. Here only two microwave connectors are soldered to the PCB. The quantum dot resonator chip is glued in the cutout in the middle of the PCB and then bonded.

lines are available on the printed circuit board via the black connector soldered to the board. The printed circuit boards were used with the connector configuration as shown in Fig. 3.4 (a,b) for all of the measurements in this thesis.

3.2.2 Cryogenic setup

The PCB is connected to the lid of a copper box (Fig. 3.5(b)) using screws to put the sample in the fridge. Then the lid is attached in the mount as shown in (Fig. 3.5(a)). In Fig. 3.5 (c) a side view of the closed copper box is shown. In

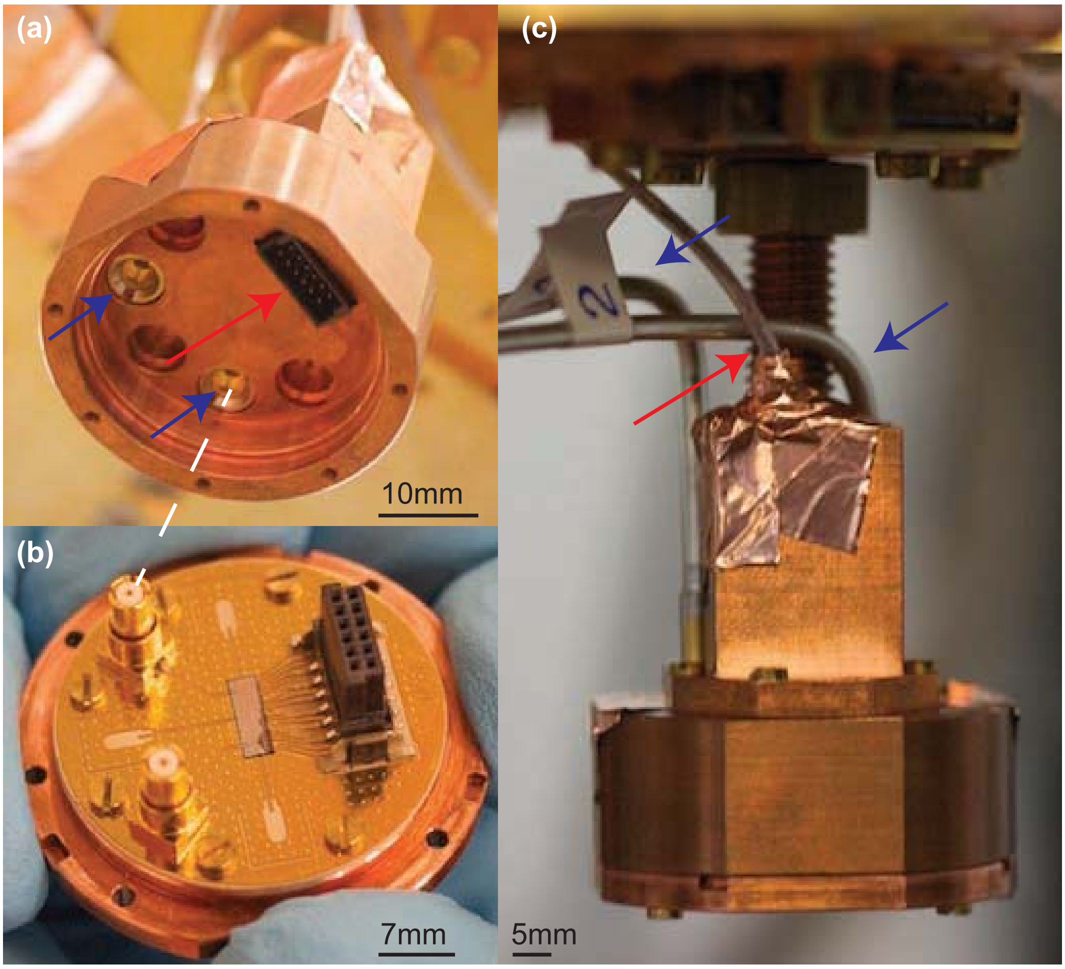

Figure 3.5: (a) Top part of the copper box used to shield the sample from electromagnetic radiation. Two microwave cables indicated by blue arrows and the 12 pin DC plug (red arrow) are fed through the lid. (b) Mount of the PC board with glued and bonded chip. White dashed line indicates the orientation of the mounting of the PCB in the lid. (c) Closed copper box with sample mounted inside, attached to the base plate of a dilution refrigerator. Blue arrows indicate the two semi-rigid microwave cables used to measure the transmission of the microwave resonator, red arrow marks the DC cables used to tune the quantum dot electrostatically.

our experiments two semi-rigid microwave cables (indicated with blue arrows in Fig. 3.5 (a,c)) and six twisted pairs of manganin wires (highlighted with a red arrow in Fig. 3.5 (a,c)) are connected to the sample inside the box. The purpose of the copper box designed for the hybrid resonator quantum dot devices is to shield the sample from electromagnetic radiation. This sample holder is mounted to the base plate of a dilution refrigerator for the experiments.

In Fig. 3.6 the microwave cabling in the fridge for one of the setups for the quantum dot resonator project is shown. In (b) the open fridge is displayed with its different temperature stages indicated. The microwave cables are attenuated by 20 dB at the 4 K stage, the cold plate (CP) and the mixing chamber (MC) to thermally anchor the semi-rigid microwave cables and to strongly attenuate Johnson-Nyquist noise [1] from higher temperature stages, especially from room temperature, before reaching the sample [57].

In Fig. 3.6 (a) a zoom near the attenuators is shown. Three of the four cables are attenuated and thermally anchored. One of these cables is used to drive the resonator, the other two are for future experiments. The fourth cable is the measurement line, used for signals which are transmitted through the cavity and is not attenuated, only the outer conductor is thermally anchored. Attenuating the signal on the measurement line would decrease the signal to noise ratio. An isolator (shown in Fig. 3.6 (d)) is mounted on the mixing chamber plate to prevent thermal radiation from the stages at higher temperatures and the input noise of the first amplifier, implemented in the measurement line, to reach the sample via the coaxial cable. The working principle of the isolator is that it routes the measuring signal from the sample towards the amplifier but guides the radiation coming from the amplifier towards the sample to a 50 Ω terminated port inside the isolator. The fridge in which our setup is built-in, is also used for other experiments using magnetic fields. Therefore our isolator is equipped with a double magnetic shield to prevent is from being damaged.

As the smallest microwave measurement signals used in the experiment contain on average less than the energy of a single 7 GHz photon per bandwidth of the resonator, the signal has to be strongly amplified before it can be recorded. We use a low noise high electron mobility transistor (HEMT) as a first amplifier as already briefly mentioned above. It is specified to have a gain of around 33 dB in the band of approximately $4 - 12$GHz and is mounted on the 4 K plate (Fig. 3.6 (c)).

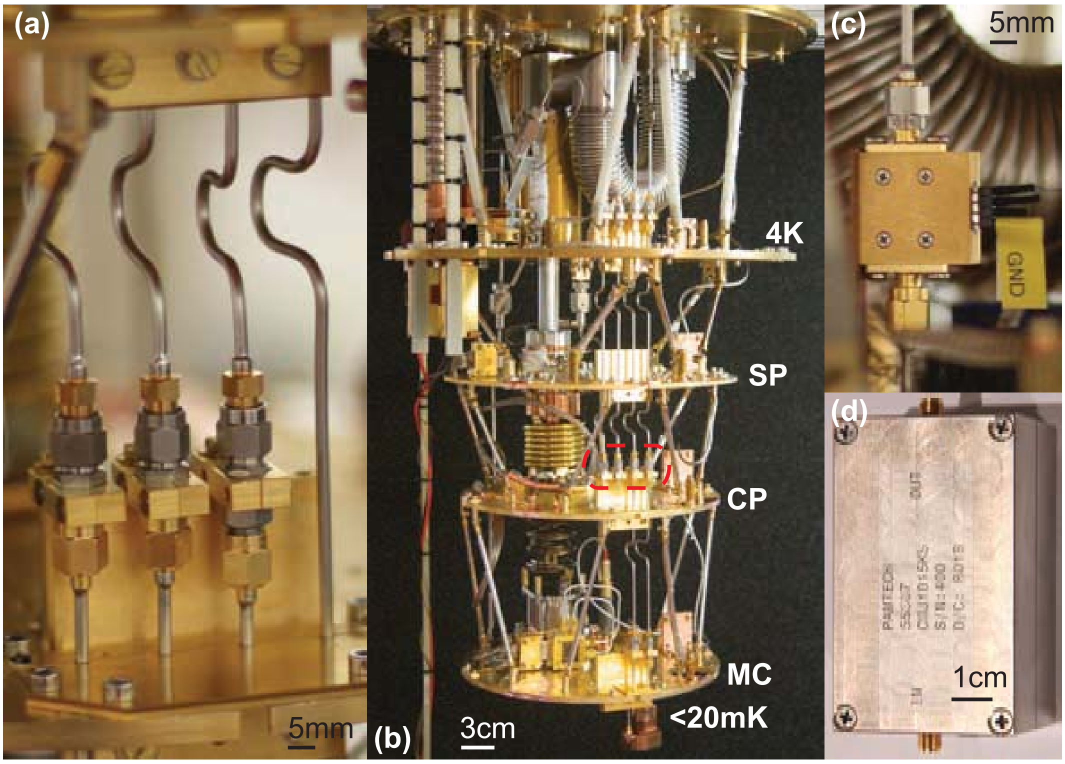

Figure 3.6: (a) Thermal anchoring of the microwave attenuators in the fridge. (b) Photograph of the open fridge. White letters indicate the different temperature stages in the fridge, 4 K stage, still plate (SP), cold plate (CP) and mixing chamber plate (MC). The inner conductors of the microwave cables which can be used to drive resonators are thermally anchored at the 4 K, the cold plate and the mixing chamber plate. Red dashed oval indicates the position of the zoom shown in (a). Note that between recording the pictures (a) and (b) the amplifier and the isolator were implemented in the setup. (c) Low noise amplifier mounted at the 4 K stage. (d) Picture of the isolator with double magnetic shield which is attached for the experiment to the mixing chamber plate and part of the measurement line coming from the sample.

3.2.3 Room temperature microwave signal processing

In this section we explain how to extract amplitude and phase information contained in the transmission signal of the resonator in a heterodyne detection scheme. In Fig. 3.7 (a-c) photographs of the different components of the microwave setup are shown, complemented by the electric circuit diagram in (d). The colored frames link the photos to the corresponding components in the schematic. The colored arrows indicate the propagation direction of the signal and relate the position in the schematic with the corresponding one in the photographs.

Two generators (SMB100a, Rhode & Schwarz), one for driving the resonator ((MWG1) Fig. 3.7 (c)) and one for the local oscillator (LO) ((MWG2) Fig. 3.7 (c)) are used for the transmission measurements. They are 25 MHz detuned. First the measurement tone is divided into two signals (DS1, DS2) of equal strength with a microwave splitter (SP) and the same is done with the LO (LO1, LO2). DS1 is sent through the resonator (see subsection 3.2.2 for details) and after coming out of the fridge further amplified and bandpass filtered (Fig. 3.7 (a)). The bandpass filters are implemented to decrease the level of the background noise within the bandwidth of the amplifiers but are chosen to have no effect within the measurement bandwidth. The measurement signal is multiplied with the LO1 in an IQ mixer (MX) in order to downconvert it to 25 MHz because we cannot directly digitize a 7 GHz electromagnetic wave due to the limited bandwidth of the digital to analog converters (ADCs) used in our experiments. Before being digitized, the signal is amplified again and lowpass filtered and then averaged on a field programmable gate array (FPGA).

The FPGA board has a second ADC. With this ADC we record the result of mixing DS2 with LO2. This signal is used as reference signal as it did not pass the fridge and its phase only depends on the generators and the length of the microwave lines. From the I and Q quadratures of the two signals we extract the amplitude (A) and the phase (ϕ) information as $Ae^{i\phi} = I + iQ$. The reference signal is needed as the generators start with an arbitrary phase for each measurement. To determine this phase and obtain the relative phase of the transmitted signal, the phase of the reference signal is subtracted from the transmission phase.

The remaining components shown in Fig. 3.7 (c) that have not been mentioned so far are the rubidium frequency standard (clock) which is used to synchronize the two generators, the arbitrary waveform generator (AWG) and the FPGA. The AWG triggers the FPGA for the measurements. More details on the different microwave components can be found in Ref. [57], where a similar setup is described.

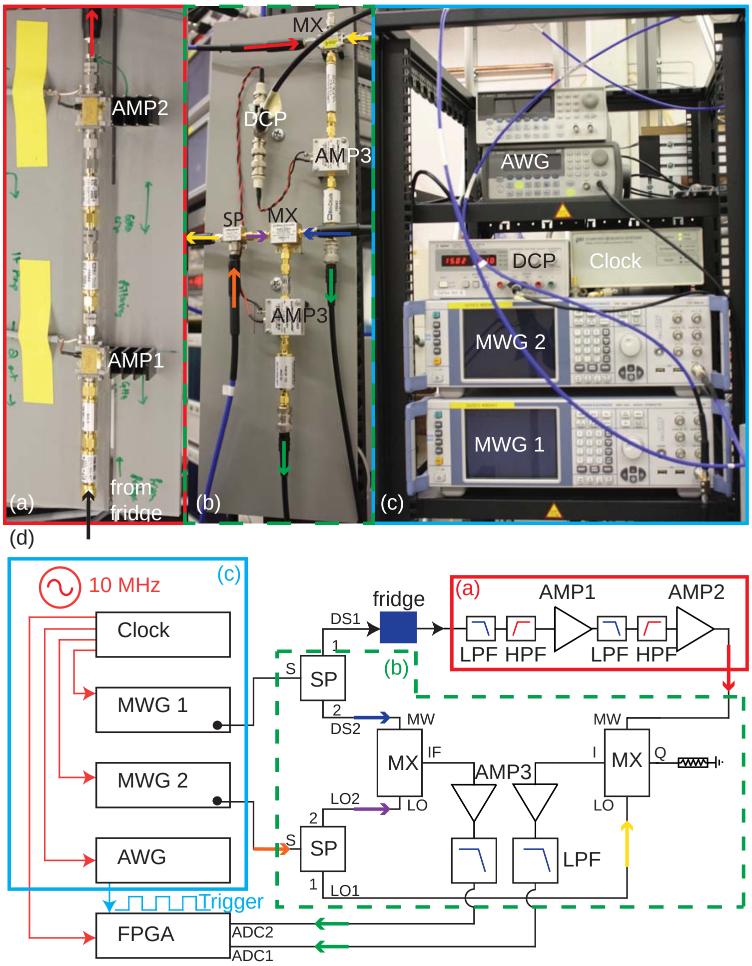

Figure 3.7: Measurement of the microwave field. (a) Pictures of the warm amplifier part of the setup. Black (red) arrow indicates where the microwave signal enters (exits) the room temperature amplifier circuit. (b) Photograph of the downconversion board. Colored arrows indicate the direction of the different microwave signals and are also seen in the schematic plot in (d). DCP stands for direct current power for the amplifiers, other abbreviations listed in (d). (c) Picture of the rack with the microwave equipment used for the measurements. It consists of a rubidium frequency standard (clock) to synchronize the different measurement devices. Two microwave generators (MWG1, MWG2) are used: one for measuring the resonator transmission, and the second one to downconvert the resulting signal. The arbitrary waveform generator (AWG) is used to trigger the field programmable gate array (FPGA) circuit. (d) Schematic of the microwave part of the measurement system. It consists of microwave generators (MWG1, MWG2), a clock and an AWG. For the processing of the signal it is passed through splitters (SP) dividing the signal into two signals of equal strength, amplified (AMP1, AMP2, AMP3), low and high pass filtered (LPF, HPF) and mixed (MX) with the LO to downconvert the signal. Encircled parts correspond to the pictures (a-c) respectively. For more details see text.

3.2.4 Room temperature direct current measurement setup

Our setup can also be used to perform standard transport measurements through quantum dot samples in the sub-kHz regime. In this section we briefly discuss the different components required, along with the schematics of the most relevant parts (Fig. 3.8) and show photographs of the setup (Fig. 3.9).

For the current measurements through our samples we use home-built current to voltage converters (IVCs) based on operational amplifier (op-amp) circuits [58] . A simplified circuit diagram of the current to voltage converters is shown in Fig. 3.8 (a). It consists of two operational amplifiers operated in the negative feedback mode. The resistors R_f set the amplification of the incoming signals hooked up to the ports labeled I_in1 and I_in2. The sample is connected between I_in1 and I_in2. The resistors R_1 and R_2 serve as voltage dividers for the voltage V_DC which is used to apply a bias voltage across the sample. In fact in an additional circuit (not shown) the voltage V_DC is split and one part is inverted for one of the operational amplifiers. This leads to a symmetric bias around 0 V across the sample. The voltage division is used to increase the voltage resolution in the measurements and to increase the signal to noise ratio. The use of two operational amplifiers for the current measurements provides the possibility to record the current flowing into the sample at the same time as the current leaving the sample and therefore allows the detection of leakage currents.

In addition the double IV converter design enables the use of a pair of twisted measurement cables to connect the sample and the IVCs for sensitive current measurements reducing the unwanted coupling to electromagnetic radiation present in the lab. With a design consisting of only one IV converter the ground connection of the setup serves as one contact for the measurements. This potentially leads to a decrease of the signal to noise ratio. Another reason for using two IVC circuits is to minimize the change of the bias voltage due to temperature dependent drifts of the operational amplifiers. The two operational amplifiers are located on two different integrated circuit chips. The two chips are thermally coupled in our designs to prevent the occurrence of small temperature differences between them as the integrated circuits heat up in operation. We observe that the operational amplifiers tend to drift in the same direction with temperature resulting in a reduction of the change of the bias voltage. A more detailed investigation of the electric properties of a similar setup for the DC transport measurements as used in this thesis can be found in Ref. [59].

In Fig. 3.8 (b) the schematic of the circuit is shown which is used in the context of the voltages set to the gates to tune the electrostatics in the sample. The circuit allows the addition of two voltages V_in1 and V_in2. The voltage on input 1 (V_in1) is divided by a factor of around 20 and the voltage on input 2 (V_in2) by around 20000. The idea of the circuit is to increase the 1 mV resolution of the SIM 928 SRS voltages sources which we had available for the experiment by combining two of the sources and divide their outputs differently. We are aware that the overall output voltage

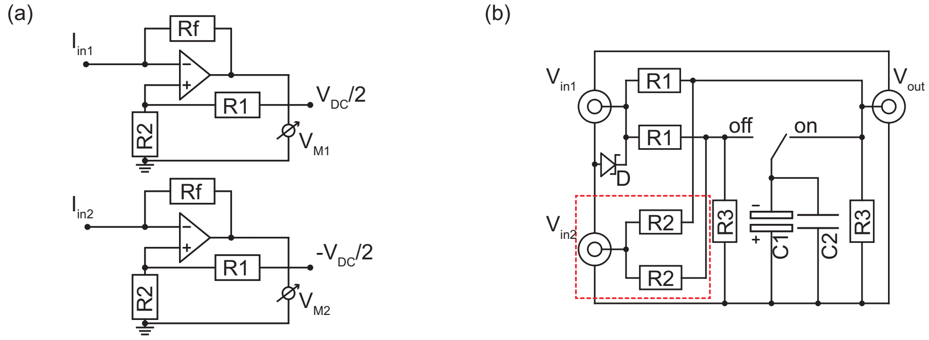

Figure 3.8: (a) Simplified schematic of the current to voltage converter (IVC) circuit. It consists of two operational amplifiers wired to resistors R_f setting the amplification. A sample would be hooked up between I_in1 and I_in2. A voltage V_DC is applied to provide a potential difference across the sample. The ratio between V_DC and the potential difference across the sample depends on the ratio between R_1 and R_2. The circuit allows to monitor the current that flows into and out of the sample at the same time and is measured by recording the voltages V_M1 and V_M2. (b) Circuit schematic of the boxes shown in Fig. 3.9 (a) containing the low frequency electronics used with the gate voltages applied to the sample. The circuit consists of resistors ($R_1 \approx 19$ kΩ, $R_2 \approx 20$ MΩ, $R_3 \approx 1$ kΩ), two capacitors $C_1 \approx 100$ nF, $C_2 \approx 2200$ μF and a diode D. The circuit allows to add the voltages $\approx V_\mathrm{in1}/20$ and $\approx V_\mathrm{in2}/20000$. The output voltage can optionally be low pass filtered. Both presented circuit designs were mainly developed by Paul Studerus.

is only stable within the time scale set by the voltage noise on V_in1 and depends on the stability of the digital to analog converter of the corresponding voltage source. The circuit shown in Fig. 3.8 (b) offers the possibility to add capacitors in parallel to the output voltage (V_out) for low pass filtering to decrease low frequency noise on our voltage signal. The low cut off frequency ($f_\mathrm{g} \approx 72$ mHz) chosen for our circuits increases the waiting time between setting the voltage and the recording of the measurement result. Therefore a switch is implemented to connect or disconnect the capacitors to the output voltage, allowing low noise and fast sweep measurements. The network of resistors is realized twice in the box in order to have the capacitors always at the same voltage as the measurement voltage to reduce voltage fluctuations on V_out when the capacitors are connected. To reach such low cut off frequencies f_g an electrolytic capacitor (labeled C_1 in Fig. 3.8) has to be implemented and the second small capacitor C_2 is added to improve the low pass filtering in the MHz regime. The didode D is implemented to protect the capacitor C_1 which would be harmed when the wrong voltage polarity is applied to the input port. For our measurements we additionally implemented simpler circuits which only divide the incoming voltage and offer the possibility to filter the output voltage. The corresponding schematic is the same as the one shown in Fig. 3.8 leaving away the parts encircled with the dashed red rectangle.

A photograph of the box containing the IV converter circuits and the interface box (IB) between the fridge and the BNC cables is shown in Fig. 3.9 (a). The boxes for the resistive voltage dividers (F) which include a switch to turn on low pass filtering as described above are also seen. Fig. 3.9 (b) shows the rack containing all the devices used for the transport measurements, consisting of voltages sources (Yokogawas and SRS battery-powered sources), multimeters to record output values of the current to voltage converters and lockin-amplifiers for direct dI/dV conductance measurements.

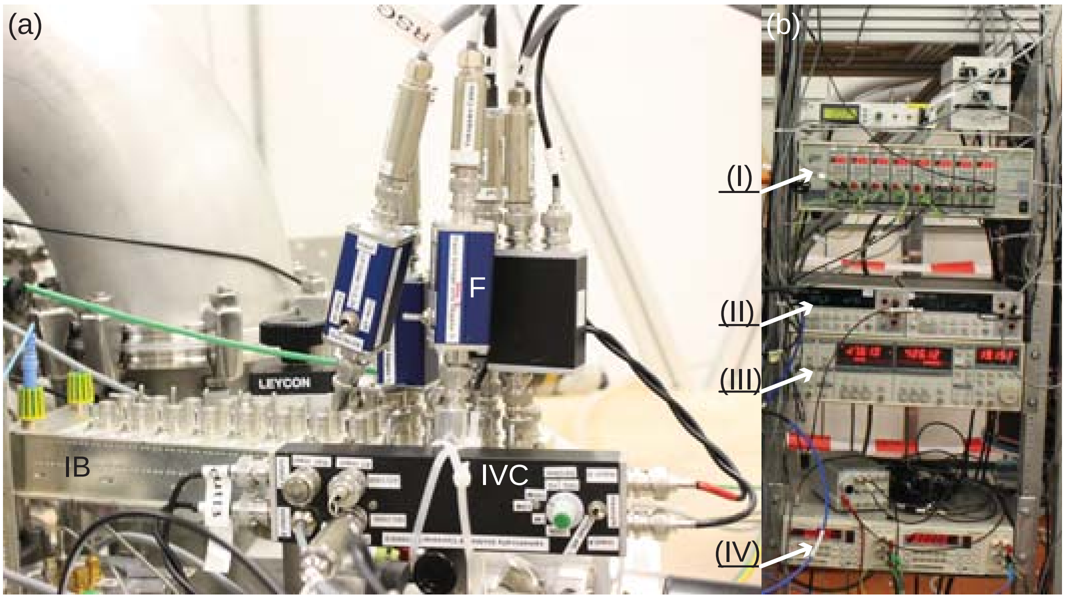

Figure 3.9: (a) Top view of the fridge showing the interface box (IB) between the fridge and the BNC cables, boxes containing voltage dividers with included filters (F) and IVC labels the box containing the current to voltage converter circuits used for the transport measurements. (b) Rack for the DC measurements with the following equipment: (I) SIM 928 SRS voltage sources, (II) Agilent HP 34410A multimeter, (III) SR 830 lock-in amplifiers, (IV) Yokogawa voltage sources.

Chapter 4

Superconducting microwave resonators on GaAs

In this chapter $\lambda/2$ and $\lambda/4$ microwave resonators are introduced for exploring the properties and suitability of semi-insulting (SI) GaAs as a dielectric material. GaAs is investigated as a substrate because it is the basic material for MBE grown GaAs heterostructures used for quantum dot experiments. For these investigations, preceding the fabrication of the hybrid devices containing the resonator and the quantum dot, SI-GaAs as obtained from the manufacturer is used. The wafers have a resistivity larger than $8 \cdot 10^7$ Ωcm at 22 °C, and the crystal orientation is $[1, 0, 0]$. Aluminum is used as the superconducting metal for all the resonators. Details on the resonator fabrication can be found in section 3.1.

The structure of the chapter is as follows: we start with a section on $\lambda/2$ resonators discussing the design considerations and characterization parameters. A similar description is done for the $\lambda/4$ resonators. The chapter is concluded with a presentation of the properties of GaAs as a dielectric substrate for high-quality microwave resonators. For comparison, a detailed analysis of microwave resonators on a silicon substrate can be found in Ref. [60].

4.1 Half-wavelength resonators

4.1.1 Design considerations

In Fig. 4.1 (a) a photograph of a PCB with two wire bonded $\lambda/2$ resonators is shown. They are realized using a coplanar waveguide transmission line capacitively coupled to an input and output line (Fig. 4.1 (b)) allowing for transmission measurements. At the fundamental frequency (ν_0) the length of the resonator is equal to half a wavelength ($\lambda/2$), forming a standing wave profile with voltage antinodes at the input and output of the resonator. The gap (7.1 μm) and the width of the center conductor (10 μm) are chosen to form a transmission line of 50 Ω wave impedance. The calculation for the length and the width were performed using the freeware transmission line calculating software $TX - Line$® [61] but can also be done analytically [48]. The coupling capacitance increases with decreasing distance between the center conductor and the feed lines and with increasing area of the resonator facing the coupling lines (Fig. 4.1 (c)). This way the coupling strength can be engineered specifically for every particular experiment. The coupling capacitors simulated with a finite element model software *Maxwell*® [62] range from approximately 0.7 fF to about 45 fF for our different designs. Note that the larger the size of the coupling capacitance is chosen the smaller the quality factor of the resonator is.

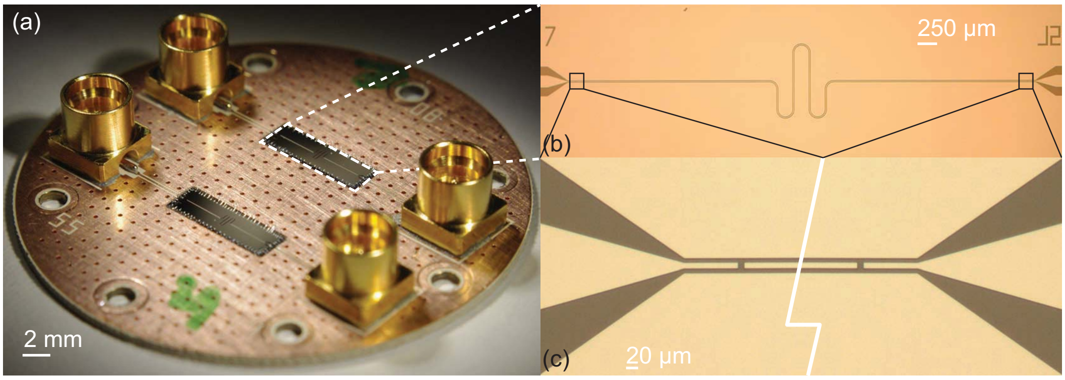

Figure 4.1: (a) Photograph of a printed circuit board with two microwave resonators made of aluminum mounted. (b) Optical image of one of the $\lambda/2$ resonators. (c) Zoom of coupling capacitors at each end of the resonator.

4.1.2 Resonator characterization and parameter extraction

The microwave resonators are characterized by measuring their transmission spectrum. The samples are cooled down in a dilution refrigerator with a millikelvin (mK) base temperature well below the critical temperature of the aluminum to minimize resistive loss. The transmission is recorded using a vector network analyzer. A typical transmission spectrum of a $\lambda/2$ resonator is plotted on a logarithmic scale (dB) in Fig. 4.2. It can be fitted well with a Lorentzian line shape (red line) with the full width at half maximum ($\delta\nu$), and the resonance frequency (ν_0) indicated. The loaded quality factor (Q_L) is defined as [60]:

$$Q_\mathrm{L} = \frac{\nu_0}{\delta\nu}, \tag{4.1}$$

which relates to the linewidth κ of the resonator

$$\kappa = 2\pi\frac{\nu_0}{Q_\mathrm{L}}. \tag{4.2}$$

Near the resonance frequency the resonator can be mapped to a lumped LCR circuit and the loaded quality factor Q_L can be expressed as a function of the internal Q_int

and the external Q_{ext} quality factor [60]

$$\frac{1}{Q_{\mathrm{L}}} = \frac{1}{Q_{\mathrm{int}}} + \frac{1}{Q_{\mathrm{ext}}}. \tag{4.3}$$

The internal quality factor is related to loss channels caused inside the resonator e.g. due to two-level fluctuators [63] or vortices [64], the external quality factor depends on the coupling strength to the measurement lines.

The insertion loss (L_0) (Fig. 4.2) is a measure of the relation between internal (Q_{int}) and external (Q_{ext}) quality factor. It is defined as [60]

$$L_0 = -20\log\left(\frac{Q_{\mathrm{int}}}{Q_{\mathrm{int}} + Q_{\mathrm{ext}}}\right)\mathrm{dB}. \tag{4.4}$$

If Q_{int} is much larger than Q_{ext} ($Q_{\mathrm{int}} \gg Q_{\mathrm{ext}}$) the transmission on resonance is 1 (0 dB). For $Q_{\mathrm{int}}/Q_{\mathrm{ext}} < 1$ the resonator is said to be undercoupled. These designs are suitable to characterize the internal properties of the resonator like the quality factor of the dielectric or the metallic film. The situation with $Q_{\mathrm{int}}/Q_{\mathrm{ext}} > 1$ is called overcoupled and improves the signal to noise ratio as more photons are detected on the measuring line than being lost through other channels in the resonator. The difficulty in determining the insertion loss is calibrating the measuring lines to correct for their losses. The properties of the lines are recorded at room temperature but losses decrease when they are cooled down. For our setup this can result in a systematic error in the insertion loss of up to about 2.5 dB and therefore the values we obtain for the insertion loss are too small.

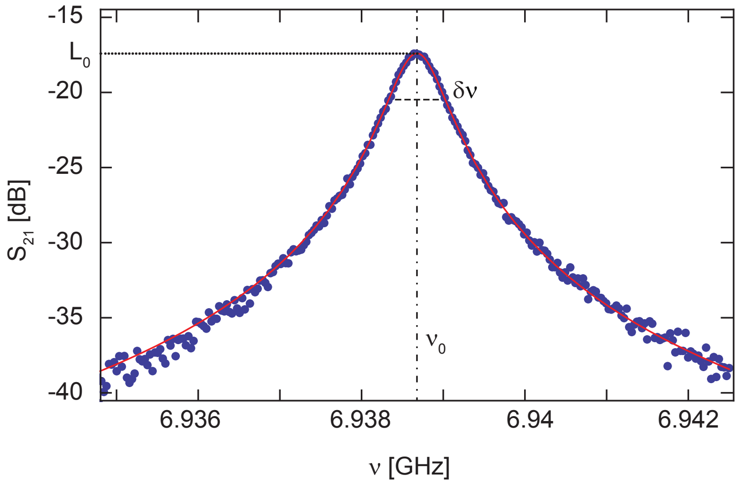

Figure 4.2: Microwave amplitude transmission measurement of a $\lambda/2$ resonator, with resonance frequency ν_0, full width at half maximum $\delta\nu$ and insertion loss L_0 indicated. The red line is a fit of a Lorentzian lineshape to the data.

4.2 Quarter-wavelength resonators

4.2.1 Design considerations

The second design consists of $\lambda/4$ microwave resonators with different resonance frequencies that are capacitively coupled at one end to a transmission line and grounded at the other end (Fig. 4.3 (a-d)). The electric field distribution inside the resonator has an antinode at the end of the resonator facing the transmission line and a node on the grounded end. At the fundamental resonance frequency (ν_0) a quarter of a wavelength ($l = \lambda/4$) fits inside the resonator.

The coupling strength to the transmission line depends on the distance between the resonator and the transmission line used for driving the resonator and the length over which the two are coupled to each other. This length should however be much smaller than the wavelength at resonance to avoid effects caused by the standing

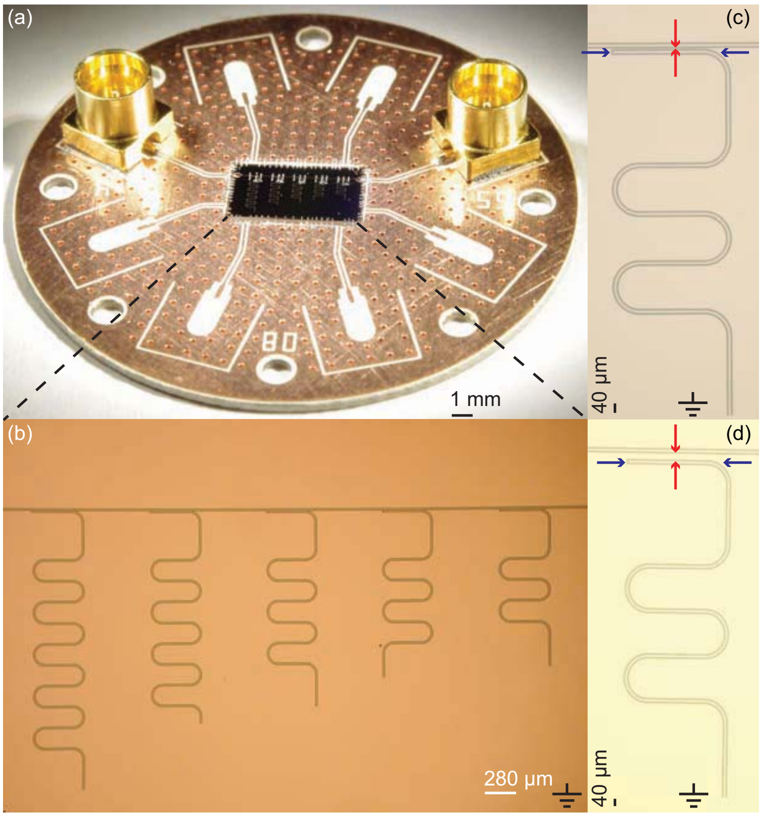

Figure 4.3: (a) Photograph of a printed circuit board with a $\lambda/4$ resonator chip made of aluminum mounted. (b) Optical image of the chip containing five $\lambda/4$ resonators with different resonance frequencies capacitively coupled to a transmission line. (c,d) Enlarged view of individual resonators with different coupling strengths to the transmission line. Red arrows indicate the distance between the resonator and the transmission line used for driving the resonators (feedline). Blue arrows indicate the distance of the coupling length between resonator and the feedline.

wave profile (Fig. 4.3 (c,d)).

The $\lambda/4$ resonators in particular were investigated for two main reasons. With our $\lambda/4$ resonator chips five resonators at several different resonance frequencies could be investigated in one single fridge run. Exact calibration which was a problem when investigating $\lambda/2$ resonators is not necessary as the calibration can be done by defining the transmission of the line as unity for frequencies detuned by several resonator linewidths (κ) from the resonance frequencies.

In Fig. 4.4 two individual non-calibrated S_{21}-parameter [55] measurements of the same chip (Fig. 4.3 (b)) are displayed on a logarithmic dB-scale. Both measurements show the same pattern. This suggests that the observed features are related to the resonators capacitively coupled to the transmission line and not due to noise. Dips in the transmission can be identified to match with the fundamental modes of the resonators at around 4 GHz, 5 GHz, 6 GHz, 7 GHz, 8 GHz (labeled with (a-e) in Fig. 4.4). Moreover, the first harmonic modes for the three lowest resonators in frequencies at three times their fundamental modes can be observed at 12 GHz, 15 GHz and 18 GHz. All other dips are suspected to be related to spurious resonances which are attributed to standing waves and whispering gallery modes in the sample mount [65]. The overall background is due to a frequency dependent microwave loss of the cabling. A discussion of the background is given in section 4.2.2.

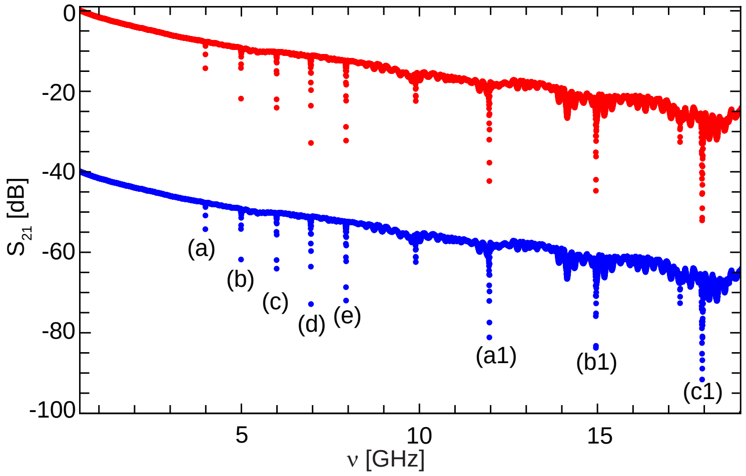

Figure 4.4: Raw data of a microwave S_{21}-parameter measurement of a transmission line capacitively coupled to $\lambda/4$ resonators. (a-e) indicate the resonance frequency of the different resonators. (a1-c1) label higher harmonic modes of the resonators. The two measurement curves are offset for a better visibility.

4.2.2 Resonator characterization - parameter extraction

When transmission measurements are performed it turns out that the resonances display a variety of complicated line shapes. This can be attributed to the setup, e.g. standing waves due to impedance mismatches could cause such lineshapes. Similar observations are made in Ref. [66] but are not discussed. To still quantitatively characterize the $\lambda/4$ resonators in the presence of these effects, a phenomenological model is proposed. It consists of a transmission line capacitively coupled to a $\lambda/4$ resonator and takes the impact of the setup into account by introducing the two rectangles labeled *bg* for background (see Fig. 4.5) whose properties are discussed in detail further below. The complex $S_{21}(\nu)$ parameter for a measurement of the transmission line near a resonance can be approximated as [67]

$$S_{21}(\nu) = \frac{S_{21}^{\text{min}} + 2iQ_{\text{L}}\delta x}{1 + 2iQ_{\text{L}}\delta x}, \tag{4.5}$$

with $S_{21}^{\text{min}} = Q_{\text{ext}}/(Q_{\text{ext}} + Q_{\text{int}})$, $1/Q_{\text{L}} = 1/Q_{\text{ext}} + 1/Q_{\text{int}}$ and $\delta x = (\nu - \nu_0)/\nu_0$. As defined above Q_{int} stands for the internal quality factor, Q_{ext} for the external quality factor and Q_{L} for the loaded quality factor. The applied frequency is labeled as ν and the resonance frequency as ν_0.

We now consider the effects caused by the setup. Depending on the applied frequency, an additional change in phase due to the finite optical length of the cables of the setup is acquired

$$e^{i\cdot(v\cdot\delta x+\Theta)}, \tag{4.6}$$

where v is related to the optical length of the setup. The term Θ takes into account that the frequency sweep starts with an arbitrary phase.

The semi-rigid microwave cables cause damping which we approximate as having a constant part (a) plus a term that depends linearly on frequency (b)

$$a + b \cdot \delta x. \tag{4.7}$$

The last correction term is a constant offset ($I_{\text{c}} + iQ_{\text{c}}$) in the complex plane for frequency independent power that is transmitted from one port of the network analyzer to the other without crossing the sample.

The equation for our model including the effects caused by the setup then reads

$$S_{21,\text{meas}} = (a + b \cdot \delta x)S_{21}(\nu)e^{i(v\cdot\delta x+\Theta)} + (I_{\text{c}} + iQ_{\text{c}}). \tag{4.8}$$

This equation is used to fit the I and Q quadratures in the complex IQ plane. In Fig. 4.6 (a) a raw data-set (black points) of a $\lambda/4$ resonator capacitively coupled to a transmission line plus the fit (red line) using Eq. 4.8 is shown in the complex plane. In Fig. 4.6 (d) the effects of the setup are subtracted for the same dataset. From the I and Q quadratures the amplitude and phase response can be calculated. These are shown in Fig. 4.6 (b,e) for the amplitude and in Fig. 4.6 (c,f) for the phase. We observe that with our modeling of the background we can locally reproduce the background which we assume to be causing the asymmetry of the peak shape. A fit using Eq. 4.5 would not result in a satisfying result.

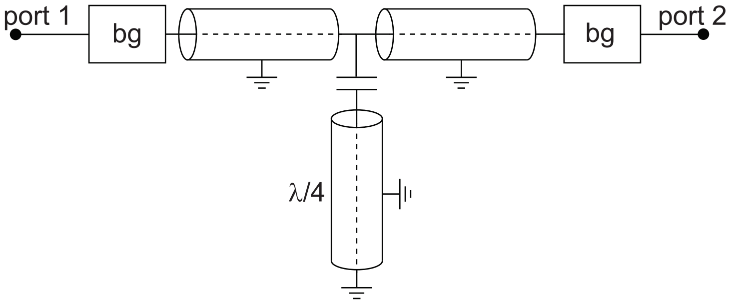

Figure 4.5: Model of a single $\lambda/4$ resonator capacitively coupled to a transmission line. The effect of the setup is modeled with the two boxes labeled *bg* for background taking into account frequency dependent phase shifts and damping. Details of the background treatment are discussed in the text.

4.3 Quality factors of microwave resonators on GaAs

In this section the results of the resonator characterization measurements are summarized. The SI-GaAs wafers [68] used as substrate for the resonators are specified to have a resistivity larger than $8 \cdot 10^7$ Ωcm at 22 °C. They are undoped and the crystal orientation is $[1, 0, 0]$.

For undercoupled $\lambda/2$ resonators ($Q_{\mathrm{L}} \approx Q_{\mathrm{int}}$) at approximately 7 GHz, a maximum value for the internal quality factor Q_{int} of around 10^4 was achieved. This value does not depend on power down to the few photon regime as shown in Fig. 4.7. This excludes two-level systems as reported in [63] as the main limiting factor for the quality of our microwave resonators.

We also dipped the GaAs into hydrochloric acid (HCl) to remove the natural oxide right before the evaporation of the aluminium and found out that its presence underneath the center-conductor and the ground plane is also not the limiting factor of the quality. In the gaps between the center conductor and the ground plane the oxide regrows, hence we could not check its influence on the quality factor.

We changed the orientation of the resonators on the GaAs wafer with respect to the crystal orientation. In dependence on the crystal orientation the coupling strength to surface acoustic waves [69] should change, but no clear dependence of the orientation on the quality factor could be detected.

For a set of $\lambda/4$ resonators the fundamental resonance frequency in the range of $2-7$ GHz is plotted versus the internal quality factor (Fig. 4.8). A different color is assigned to each sample. The green points are a reference measurement using the same design on a sapphire substrate to exclude geometry properties and the quality of the aluminum films. The other data points were obtained from measurements on samples with the SI-GaAs substrate described above.

Comparing the two wafer materials we observe that the internal quality factor

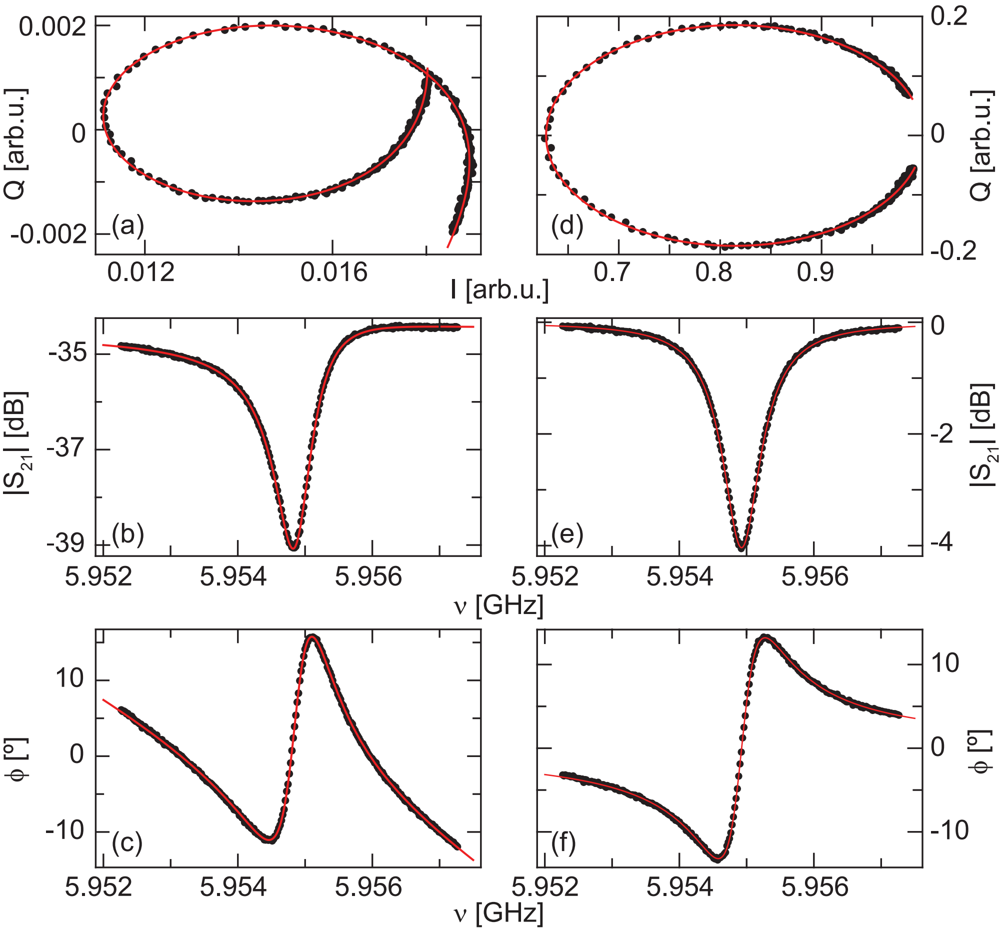

Figure 4.6: Microwave transmission data (black points) of a $\lambda/4$ resonator capacitively coupled to a transmission line. Red lines are best-fit curves using Eq. 4.8. (a-c) Different representations of the raw data: (a) I-Q representation, (b) transmission amplitude and (c) transmission phase data. (d-f) Different data representations with setup specific background subtracted, (d) I-Q representation, (e) transmission amplitude and (f) transmission phase data.

(Q_{int}) for resonators on sapphire is around one order of magnitude larger than on GaAs. We also note that Q_{int} on GaAs has the trend to increase with frequency whereas for the sapphire substrate it is the opposite. This points out that different loss mechanisms limit the internal quality factor on different materials.

While we could not identify the dominant loss mechanisms of the microwave resonators on GaAs substrates in these experiments, we speculate that the piezoelectricity of GaAs causes the coupling of microwave photons to phonons. This might be the dominant limiting factor for Q_{int}. To verify this speculation the influences of trenches, etched into the gaps of the resonators, on the quality factor could be investigated. Due to the trenches the field distribution will change resulting in less field lines penetrating the GaAs wafer and therefore a smaller effect of the

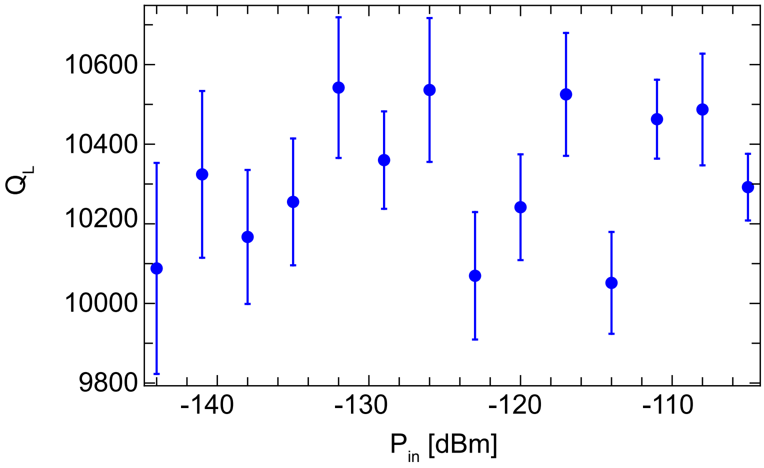

Figure 4.7: Measurement of the loaded quality factor Q_{L} of an undercoupled $\lambda/2$ resonator in dependence on the applied input power. The error bars represent the uncertainty in the fit of the Lorentzian line.

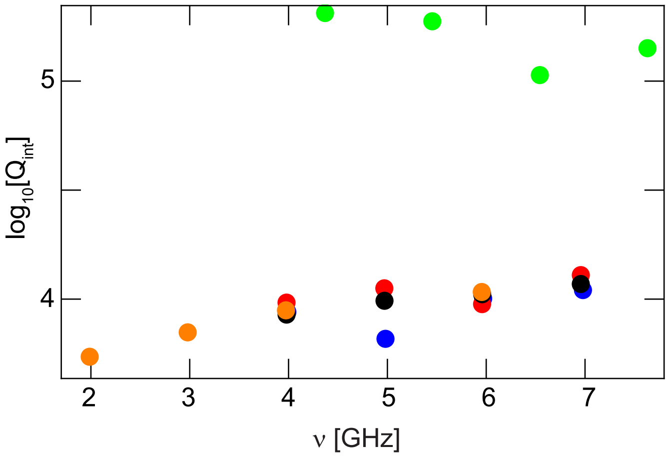

Figure 4.8: Logarithmic plot of the internal quality factor Q_{int} versus frequency for different $\lambda/4$ resonators. Green points mark data points acquired with a sapphire substrate. All other data points were acquired on GaAs wafers.

piezoelectric coupling would be expected. For other material systems, e.g. NbTiN on silicon, improvements of the quality factor were reported using the etching of trenches [70, 71].

Chapter 5

Characterization of a microwave resonator via a nearby quantum dot

In this chapter first measurements of a hybrid system consisting of a microwave transmission-line resonator and a lateral quantum dot defined on a GaAs heterostructure are presented. The two subsystems are characterized separately and their interaction is studied by monitoring the electrical conductance through the quantum dot. The presence of a strong microwave field in the resonator is found to reduce the resonant conductance through the quantum dot, and is attributed to electron heating and modulation of the dot potential. We use this interaction to demonstrate a measurement of the resonator transmission spectrum using the quantum dot.

5.1 Sample design

The sample used in the experiment is shown in Fig. 5.1 (a). It consists of a laterally defined quantum dot positioned at an antinode of the electric field of a microwave transmission-line resonator. The dot is realized on an $\mathrm{Al_xGa_{1-x}As}$ heterostructure with a two-dimensional electron gas (2DEG) residing at the heterointerface about 35 nm below the surface. The device is fabricated by three stages of optical lithography followed by local anodic oxidation (LAO) with an atomic force microscope (AFM) to define the quantum dot. Details of the fabrication techniques are described in chapter 3.

The minimum distance from the mesa edge to the center conductor of the resonator is around 2 μm. The coplanar waveguide resonator is designed to have a fundamental frequency $\nu_0 \approx 7$ GHz and is coupled to the input/output lines by two planar finger capacitors (Fig. 5.1 (b)). The capacitance, determined in a finite element calculation, corresponds to an external quality factor [60] of $Q_{\mathrm{ext}} \approx 8000$.

In Fig. 5.1 (d) the AFM defined nano-structure is shown. It consists of the quantum dot connected by two tunnel barriers to the source (S) and drain (D) contacts used to measure the conductance of the dot. In addition a left side gate (LSG), a plunger gate (PG), and a right side gate (RSG) are used to tune the potential of the quantum dot. The lithographic diameter of the quantum dot is approximately 230 nm.

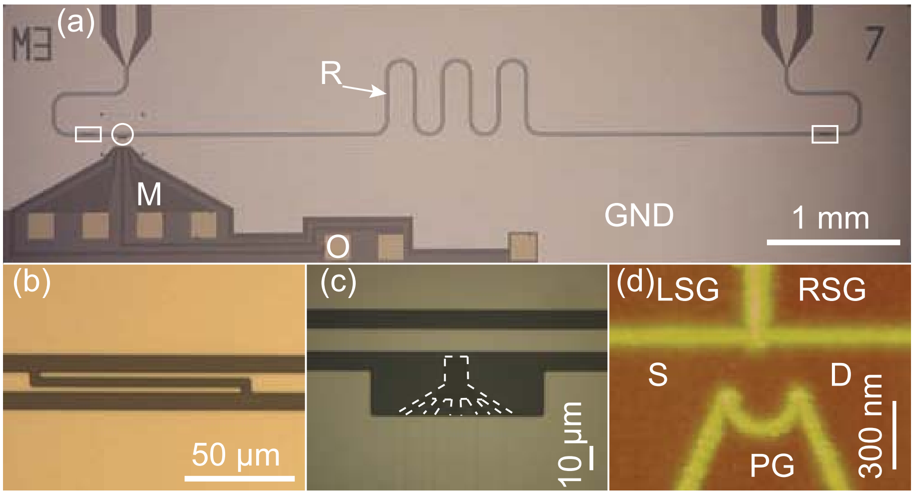

Figure 5.1: (a) Optical micrograph of a microwave resonator (R) with an integrated quantum dot, (GND): ground plane of the resonator, (O): ohmic contact, (M): 2DEG mesa. (b) Magnified view of a coupling capacitor, location on the chip marked with rectangles in (a). (c) Enlarged view of the 2DEG mesa, location on the chip marked with a circle in (a). Edge of the mesa highlighted with a dashed line. (d) AFM picture of the measured quantum dot, realized on the 2DEG mesa. Source and drain contacts are labeled (S), (D), the plunger gate (PG), and the left and right side gate (LSG), (RSG).

5.2 First quantum dot resonator interaction measurements

Coulomb blockade diamonds of the quantum dot with no microwave power applied, measured via lock-in techniques, are shown in Fig. 5.2 (a). The charging energy (E_C) of the quantum dot extracted from the size of the Coulomb blockade diamonds in bias voltage (V_SD) direction is found to be approximately 3 meV. The diameter of the dot is estimated with the disc capacitor model $E_\mathrm{C} = e^2/C_\Sigma = e^2/4\epsilon_0\epsilon_\mathrm{GaAs}d$, with C_Σ the self-capacitance of the quantum dot, e the electric charge, d the diameter of the quantum dot, ϵ_GaAs the relative dielectric constant of GaAs and ϵ_0 the vacuum permittivity. The diameter is found to be $d \approx 115$ nm. Excited state resonances are observable, indicated by white arrows. The typical single-particle level spacing that was resolved is about 350 μeV. Using the constant density of states of the 2D system

[1], the single-particle level spacing can be utilized to estimate the diameter of the quantum dot to be about 110 nm. The value is in good agreement with the dot size calculated using the disc capacitor model. The electron temperature extracted by fitting a thermally broadened Coulomb resonance [4] is found to be $T_\mathrm{e} \lesssim 200$ mK for this sample. Using the maximum of the Coulomb resonance at position A in Fig. 5.2 (a), the total tunnel coupling of the quantum dot energy level to the leads is estimated to be smaller than the thermal energy of the electrons. The measured Coulomb resonances do not have simple thermally broadened line shapes, indicating that the quantum dot is not deep in the single-level transport regime.

Before studying the interaction between the quantum dot and the microwave field, the transmission of the resonator is characterized using a standard network analyzer. A loaded quality factor [60] of $Q_\mathrm{L} \approx 2900$ is found for the fundamental mode, at a frequency $\nu_0 \approx 6.878$ GHz.

In a next set of experiments, the effect on the conductance of the quantum dot circuit of driving the microwave resonator is investigated. The quantum dot is swept at zero DC bias through the Coulomb resonance (position A in Fig. 5.2 (a)) by changing the voltage on the plunger gate (PG) and the dot conductance is recorded via lock-in techniques. The measurement is repeated with the addition of a microwave tone applied to the resonator at ν_0 for a range of different microwave powers (Fig. 5.2 (b)). The applied powers are specified at the output port of the microwave generator, and the total attenuation of the microwave signal from the generator to the sample is estimated to be about -30 dB. A reduction in the conductance of the quantum dot and a broadening of the Coulomb resonance with increasing microwave power are observed. We have performed the same measurement on another Coulomb resonance and found similar behavior.

We now investigate the conductance of the quantum dot at the Coulomb resonance (position A, Fig. 5.2 (a)), while sweeping the frequency of the signal applied to the resonator. In Fig. 5.2 (c) the change of the conductance ΔG at the Coulomb resonance is plotted as a function of the applied microwave frequency ν at a power of -27 dBm. The change ΔG is measured relative to the conductance value obtained when the applied microwave frequency is detuned by several GHz from an eigenfrequency of the resonator. Sharp minima in the conductance signal of the quantum dot are observed at frequencies of 6.878 GHz, 13.773 GHz, 20.658 GHz, 27.517 GHz, labeled (1) to (4) in Fig. 5.2 (c). They correspond to the fundamental frequency (ν_0) and the first three harmonics (ν_1, ν_2, ν_3) of the resonator within a relative error of $E_\mathrm{n} = (\nu_\mathrm{n} - n \cdot \nu_0)/\nu_\mathrm{n} \approx 0.1$ %. The two small additional resonances, marked with arrows, are likely to be caused by sample holder resonances [65]. The conductance measurement through the quantum dot is sensitive enough to observe higher harmonic modes of the microwave resonator that are outside of the frequency range of up to approximately 20 GHz for which the present microwave setup is designed.

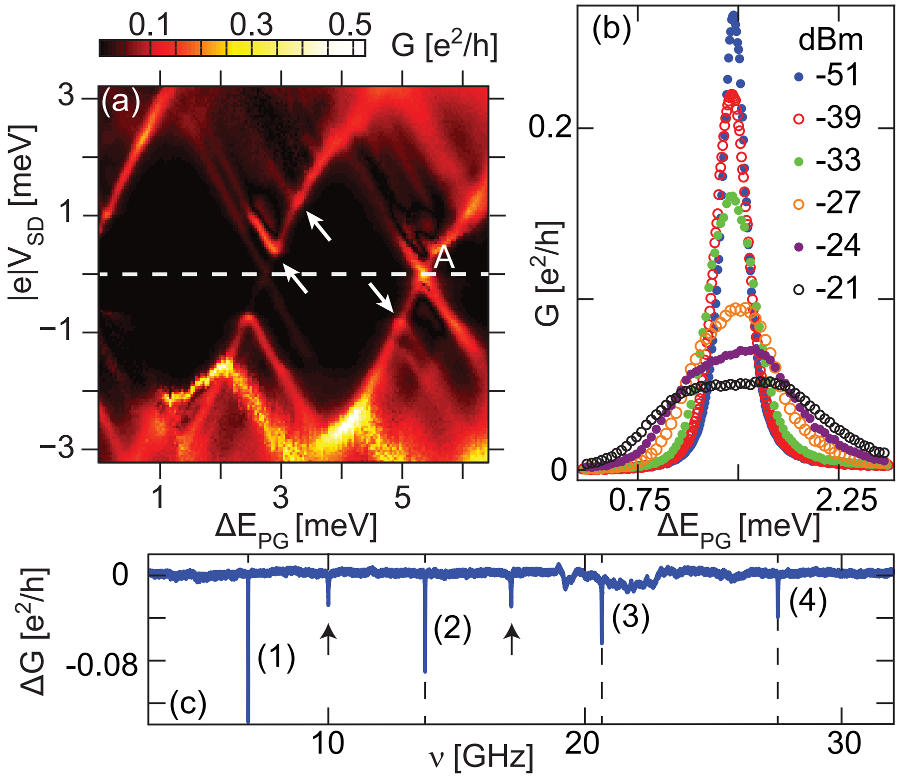

Figure 5.2: (a) Charge stability diagram of the quantum dot without applied microwave power. White arrows indicate excited states. (b) Conductance through the quantum dot in the vicinity of point A in (a) as a function of the PG voltage, for different microwave powers applied to the resonator. (c) Relative change in conductance ΔG of the quantum dot as a function of the microwave frequency applied to the resonator. The resonator modes are numbered (1)-(4), and arrows indicate additional spurious modes.

5.3 Quality factor of the resonator obtained measuring quantum dot properties

In a next step the quantum dot conductance is analyzed at a small applied bias of 75 μV in the vicinity of ν_0. The frequency of the tone applied to the feed lines of the resonator is swept and the conductance through the dot is measured with the quantum dot tuned to position A. To relate the influence of the strength of the electromagnetic field to the quantum dot conductance, the measurement is repeated for microwave powers ranging from −55 dBm to −20 dBm. In Fig. 5.3 (a) the change in conductance ΔG of the quantum dot is plotted versus the frequency applied to the resonator. The minimum of the conductance is found at the resonance frequency of the resonator and the change of the conductance ΔG increases with microwave power.

In Fig. 5.3 (b) the minima of ΔG, extracted from datasets as shown in Fig. 5.3 (a), are plotted as a function of the applied microwave power to establish a relation between the two quantities. The fact that the curve in Fig. 5.3 (b) levels off for small microwave power is ascribed to the finite sensitivity of the quantum dot. Note that the smallest input power that is clearly detectable as a change in conductance is $P_{\mathrm{min}} = -50$ dBm, corresponding to a resonator population of $n \approx 15 \cdot 10^4$ photons. Hence a stronger coupling between the two systems would be required to realize a more sensitive detection potentially at the single-photon level. To extract the scattering matrix element S_{21} from the dataset with $P = -20$ dBm, the conductance scale of Fig. 5.3 (a) is now converted into a power scale using Fig. 5.3 (b) and then normalized so that the transmission peak is at 0 dB. A Lorentzian line shape is obtained, blue points in Fig. 5.3 (c). The coupling between the dot and the resonator is assumed to be constant over the narrow frequency range covered in the dataset. Also shown with open circles in Fig. 5.3 (c) is the S_{21} signal measured with a network analyzer, offset from the other curve by -5 dB for clarity. Both curves are fitted with a Lorentzian line shape to extract the loaded quality factor Q_{L} [60] of the resonator. The obtained values are $Q_{\mathrm{L}} = 2896 \pm 22$ for the network analyzer measurement, and $Q_{\mathrm{L}} = 2890 \pm 30$ for the dot conductance based measurement, in very good agreement with each other, supporting the assumption of the constant coupling between resonator and dot.

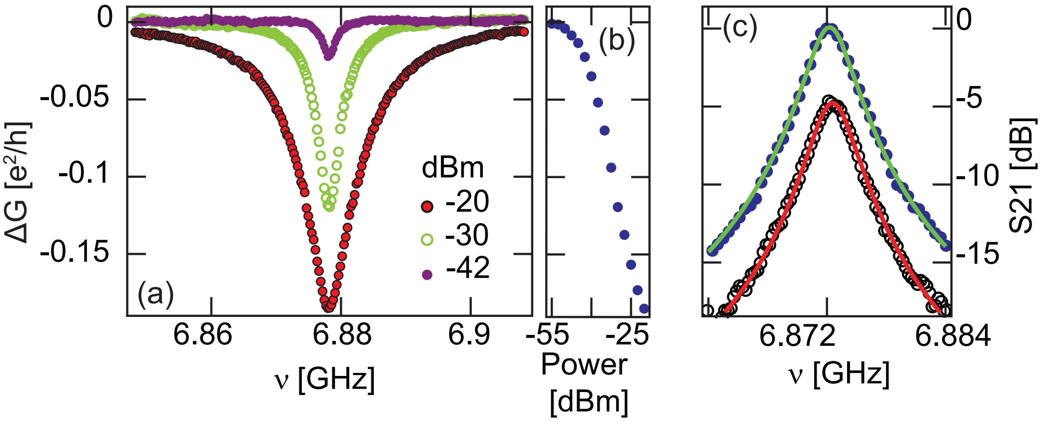

Figure 5.3: (a) Conductance measurement at Coulomb resonance A in Fig. 5.2 (a) versus frequency of the driving tone in the vicinity of the fundamental mode, for indicated microwave drive powers. (b) Maximum conductance change ΔG versus microwave power. (c) Resonator spectrum extracted from the dot conductance signal (blue dots) fitted with a Lorentzian line shape (green line). The dark circles are data points obtained using a network analyzer and are fitted with a Lorentzian line shape as well (red curve). The two curves are offset for clarity.

We now discuss the potential coupling mechanics between the quantum dot and the microwave resonator. Due to the large extension of the resonator in comparison to the quantum dot, there is not only a coupling of the microwave to the quantum dot itself but also to the surrounding 2DEG areas. The direct coupling capacitance between the resonator and the dot in the present geometry is of the order of 1 aF, much smaller than the coupling capacitances between the resonator and the leads, which are in the range of $0.1 - 1$ fF (estimated from DC characterization measurements and finite element simulations). The conductance peaks in Fig. 5.2 (b) both decrease in height and broaden with increasing microwave power. These features can be explained as a thermal broadening of the conductance resonance [1] which can arise due to heating of the 2DEG by the microwave. In addition the line shapes of the conductance resonances for the higher microwave powers (-24 dBm and -21 dBm, Fig. 5.2 (b)) indicate that the peak form is a superposition of two resonances. These line shapes are consistent with a modulation of the voltage on one or more of the gates and leads of the quantum dot by the microwave. The coupling of the cavity to the quantum dot may therefore be explained as a combination of heating and gate modulation.

Chapter 6

Single dot admittance probed with an on-chip resonator at microwave frequencies

In this chapter microwave frequency measurements of the dynamic admittance of a quantum dot, which is tunnel coupled to a two-dimensional electron gas, are presented. The measurements are made via a high-quality 6.75 GHz on-chip resonator capacitively coupled to the dot. The resonator frequency is found to shift both down and up close to conductance resonance of the dot, corresponding to a change of sign of the reactance of the system from capacitive to inductive. The observations are consistent with a scattering matrix model. The sign of the reactance depends on the detuning of the dot from a conductance resonance and on the magnitude of the tunnel rate to the lead with respect to the resonator frequency. Inductive response is observed on a conductance resonance, when tunnel coupling and temperature are sufficiently small compared to the resonator frequency. Previous experiments at frequencies smaller than tunnel coupling and temperature have shown good correspondence to theory when the quantum dot circuit is modeled as a capacitor and a resistor connected in series [43].

6.1 Sample design and setup

The sample we have investigated for the experiments presented in chapter 6 and chapter 7 is shown along with an electrical circuit diagram of the sample and of the setup in Fig. 6.1. A $\lambda/2$ microwave resonator (see Fig. 6.1 (a)), also discussed in chapter 4, is realized on the chip and allows the investigation of microwave transmission spectra. The double quantum dot (see Fig. 6.1(c)) is positioned at an anti-node of the standing wave field distribution of the resonator. The left and right dots (LD, RD) are arranged in series with respect to the source and drain (S, D) contacts. The quantum dots are realized on an $\mathrm{Al_xGa_{1-x}As}$ heterostructure in which the two-

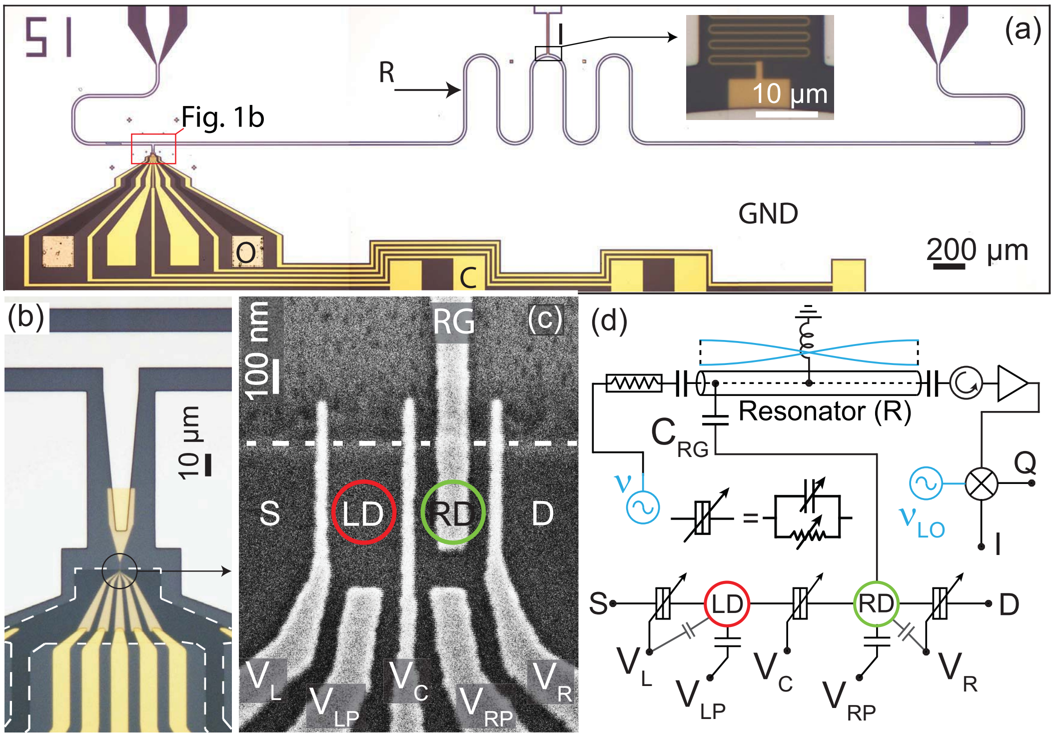

Figure 6.1: a) Optical micrograph of the microwave resonator (R), with integrated double quantum dot, ohmic contacts (O), top gates (C), ground plane (GND), and on-chip inductor (I). Inset: magnified view of inductor (I). (b) Enlarged view of the device near the double quantum dot. The mesa edge is highlighted with a dashed line. (c) Scanning electron micrograph of the gate structure defining the double quantum dot (LD, RD). RG marks the gate connected to the resonator, (V_{L}, V_{LP}, V_{C}, V_{RP}, V_{R}) label top gate voltages, and S, D, the 2DEG source and drain. (d) Electric circuit representation of the double quantum dot coupled to the resonator. The double quantum dot is tuned with voltages V_{L}, V_{LP}, V_{C}, V_{RP}, V_{R} and connected to the resonator via the capacitance C_{RG}. The resonator is driven with a microwave signal at frequency ν. The transmitted signal passes through a circulator, is amplified and mixed with the local oscillator at frequency ν_{LO} to obtain the field quadratures I and Q.

dimensional electron gas (2DEG) is formed at a depth of about 35 nm below the surface.

A selective capacitive coupling between the two systems which is mediated by a gate (RG) extending from the resonator to the right quantum dot only (Fig. 6.1 (b,c)) is engineered for this chip in contrast to the sample used in chapter 5. This coupling is independently confirmed at DC by biasing the resonator through an on-chip inductor (Fig. 6.1 (a), inset). The on-chip inductor consists of a meandering line about 250 nm wide with a thickness of around 3 nm titanium (Ti) and around 40 nm of gold (Au). It is positioned at the voltage node of the fundamental mode to disturb the standing wave electric field distribution in the resonator as little as possible. The possibility to bias the center conductor has the advantage that there is no floating gate. Floating gates otherwise might charge over time and hence cause drifts in the measurements [72]. In addition the resonator gate can also be used to tune the quantum dot potential via the inductor. Note however that adding an additional voltage source to the sample might lead to an increase of the decoherence of the quantum dot charge states and is subject of further investigations.

The implemented coupling scheme results in a strong microwave frequency dipole interaction of the resonator with two charge states which differ by one electron being either on the left or right quantum dot. But also tunneling processes of an electron between the dots and the leads can be detected via the resonator. In order to accommodate the gate (RG), the dots are placed at the edge of a mesa (beyond which the 2DEG is etched away), used as part of the confining potential. Negative voltages are applied to metallic top gates (Fig. 6.1(a)) below which the 2DEG is then depleted to complete the formation of the dots.

The experiments are performed in a dilution refrigerator with a base temperature of approximately 10 mK. During the cooldown of the sample we apply a negative voltage of about -250 mV to the 2DEG contacts with all other gates grounded but the resonator gate (RG) which is set to around -150 mV. This method named prebias cooldown is known to reduce charge noise [73]. The voltage difference between the gates and the 2DEG leads to an increase of the population of the DX centers [74] in the vicinity of the gates which remains at low temperatures without prebias applied. In the literature DX centers name localized defect centers which are charged negatively [75]. The prebias cooldown has the effect that a less negative potential is needed on the gates for operating the quantum dot. The resonator gate is set to -150 mV as the electron density underneath should not be minimized due to an expected decrease of the resonator quantum dot coupling strength but still potential leakage through the Schottky barrier should be diminished [76]. The voltages are applied with a 1 GΩ resistor in series to minimize the leakage current through the gates due to thermally activated electrons in the semiconductor at the beginning of the cooldown.

For the quantum dot measurements the static potential on the dots is tuned via two plunger gate voltages V_{LP} and V_{RP}. To allow electron transport, the two dots are connected to each other and to the source (S) and drain (D) contacts through tunnel barriers, tunable by applied voltages V_{L}, V_{C} and V_{R} (see Fig 6.1 (c,d)). These tunnel barrier gates also tune the dot potentials with a similar lever arm as the plunger gates due to finite capacitive cross coupling. The charging energies of both quantum dots are $E_{\mathrm{C}} \approx 1$ meV $\approx h \times 240$ GHz as extracted from Coulomb diamond measurements.

For the microwave measurements, we apply a coherent signal at frequency ν to the resonator (R) to extract the amplitude A and phase ϕ of the transmitted signal from the measured field quadratures I and Q, as described in chapter 3. The microwave resonator has a fundamental frequency $\nu_0 \approx 6.755$ GHz and a loaded quality factor [60] $Q_{\mathrm{L}} \approx 2630$ corresponding to a decay rate $\kappa/2\pi \approx 2.6$ MHz, measured with all gates grounded such that no quantum dots are formed. The resonator is approximately prepared in its ground state with average thermal photon number $n < 1$ by using appropriate filtering and attenuation in the microwave lines, as discussed in chapter 3.

6.2 Double dot charge stability diagram obtained with microwave and direct current measurement techniques

We first investigate the dependence of the quality factor and resonant frequency of the resonator on the charge configuration when forming the double quantum dot. The measured transmission amplitude and phase are displayed in Fig. 6.2 (a,b) for two different gate voltage settings. For these and all the other microwave measurements shown in this chapter the source and drain contacts are grounded. In the first case, marked (1) in Fig. 6.2 (a,b), the quantum dot is tuned into Coulomb blockade (see chapter 2) where the number of electrons is fixed in both dots. In the second case (2), the double quantum dot is tuned to a triple point. In this configuration the chemical potentials in the leads and in each dot are aligned such that it is energetically possible for an electron to propagate elastically from one lead through the quantum dot into the other lead. The gate voltage settings of the two measurements (1) and (2) are indicated in Fig. 6.3 (a). A reduction in amplitude and a change in phase are observed between the two cases while the line shapes remain Lorentzian (Fig. 6.2 (a,b)). This fact can be exploited to save measurement time; instead of measuring the full resonance spectrum for every value of V_R and V_L, a microwave tone at a fixed frequency $\nu_M = \nu_0$ is applied to the resonator and the difference in amplitude ΔA and in phase $\Delta\phi$ is recorded.

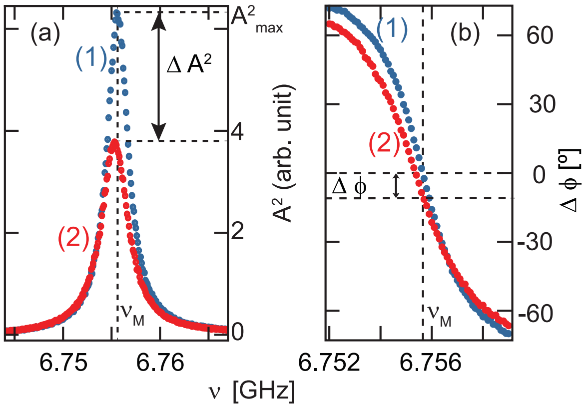

Figure 6.2: Transmission amplitude (a) and phase (b) of the resonator as a function of the frequency ν of the applied microwave signal in Coulomb blockade (1) and on a conductance resonance (2).

In Fig. 6.3 the change in amplitude (a) and phase (b) are shown for several different electron configurations in the two dots. No major undesired background charge rearrangement is visible over the whole investigated gate voltage region. In Fig. 6.3 (d) the sketch of a double dot charging diagram (chapter 2) is shown along with the corresponding quantum dot level structure in the vicinity of two triple points, as indicated in Fig. 6.3 (a). Using this schematic, we can identify different characteristic regions by taking a closer look at Fig. 6.3 (a). In region I charge transfer between the two dots and between each dot and its adjacent lead is observed. In region II (III) only charge transfer to the right (left) lead is discernible together with interdot charge transfer. The resonances to the right lead are more pronounced than those to the left lead. This is expected because the resonator is more strongly capacitively coupled to the right quantum dot than to the left, leading to a higher sensitivity to the tunnel coupling between the right dot and its lead. In region IV, no charge transfer between the dots and the leads is visible. Microwave measurements in this region are discussed in detail in chapter 7.

In this chapter, we focus on region II in which we specifically study the interaction between the right dot and the right lead. Fig. 6.3 (b) shows that the finite frequency response of the quantum dot-lead circuit does not only consist of a change in amplitude when an electron in the right dot can tunnel resonantly to the lead, but also a change in phase is observed. Since the measurement frequency is set to ν_0, such a change in phase corresponds to a change in resonance frequency. For high quality resonators this frequency shift is mainly caused by reactive changes in the impedance of the right dot tunnel-coupled to its lead, discussed in more detail below.

We compare the microwave frequency response with standard DC transport measurements (chapter 2 and Ref. [4]) as shown in Fig. 6.3 (c) to understand the origin of the finite frequency response of the quantum dot-lead circuit. Voltages V_L and V_R are swept as in Fig. 6.3 (a,b), but now a small source-drain bias $V_\mathrm{SD} \approx 50\ \mu\mathrm{V}$ is applied. In Fig. 6.3 (c) clear hexagon patterns are observable. The size of the hexagons and their position in gate voltage are the same as in the microwave measurements. For less negative gate voltages, the coupling to the leads is strong enough to lead to a finite current within the hexagons, indicating that the dots are not deep in the Coulomb blockade regime. With decreasing gate voltages V_L and V_R, and therefore decreasing tunnel rates, the resonances to the leads become smaller and finally disappear.

Although the microwave and transport measurements show equivalent charging diagrams, differences are observable, such as good or poor visibility of the interdot charging line and of the resonances to the different leads. This indicates that the physical origin of the signal is different for the two measurement techniques. We discuss this aspect in more detail below.

In the DC measurement (Figs. 6.3 (c), 6.4 (a)), the interdot charging lines at which $\mu_1(M, N-1) = \mu_2(M-1, N)$ (Fig. 6.3 (d)) are not observed because here transport is suppressed due to Coulomb blockade [2].

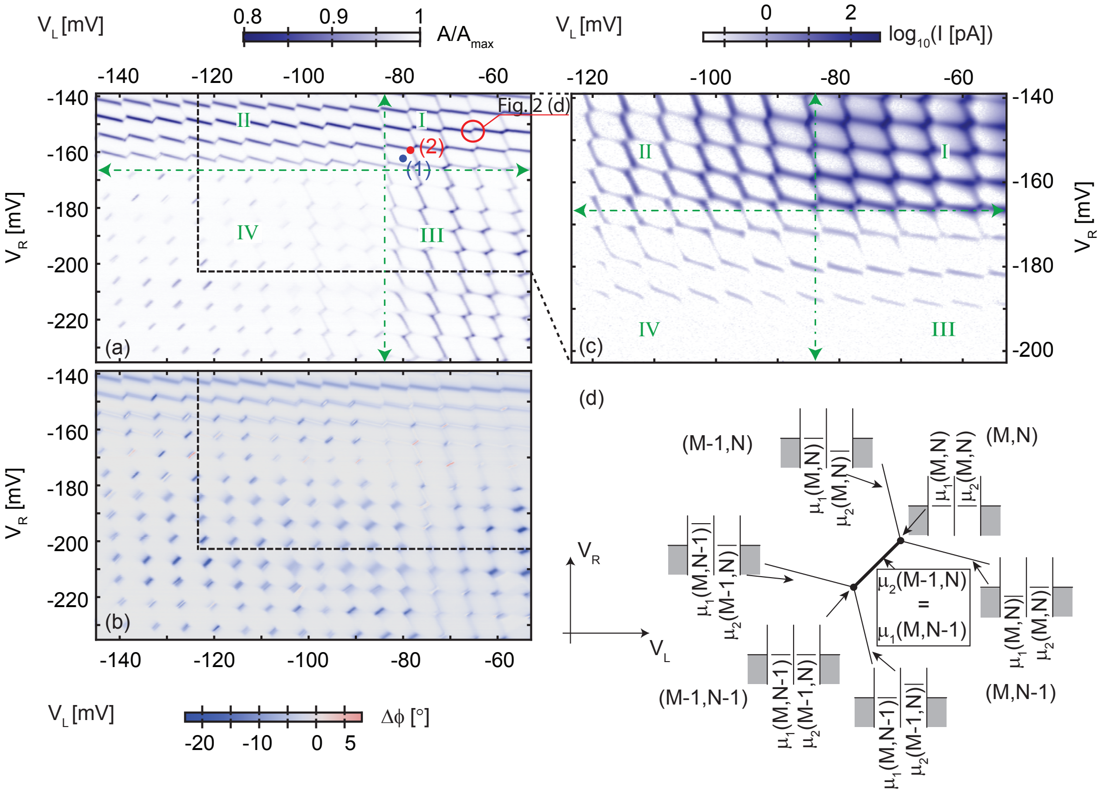

Figure 6.3: (a) Relative resonator transmission amplitude A/A_{max} at fixed measurement frequency ν_{M} as a function of V_{L} and V_{R}. Points labeled (1) and (2) mark gate voltage positions where the full resonance spectra shown in Fig. 6.2 (a,b) are measured. Green roman numerals label four different measurement regions separated by dash-dotted green lines (see text for details). (b) Phase change of the microwave resonator for the same gate voltage ranges as in (a). (c) Direct current measurement through the double quantum dot for gate voltage settings V_{L} and V_{R} within the dashed region highlighted in (a). (d) Schematic of the charging diagram of a double quantum dot for (M,N) electrons close to the two triple points as a function of V_{L} and V_{R}.

Sketches visualizing a possible explanation for the difference in the signals of the dot-lead resonances are shown in Fig. 6.4 (c,d). The transport data in region III (Fig. 6.3 (c)) shows mainly cotunneling lines [2] with the right dot being in resonance with the lead with decreasing V_{R}. In the corresponding microwave measurement however, the resonances to the left lead are more pronounced. Equivalent features can also be found in region II with decreasing V_{L}, as shown in Fig. 6.4 (a,b). This time the resonance to the left lead is seen in the transport data and the resonance to the right lead in the microwave measurements. This indicates that the microwave signal strength related to the process of an electron tunneling between the dot and the lead depends strongly on the tunnel rate to this lead (Fig. 6.4 (d)).

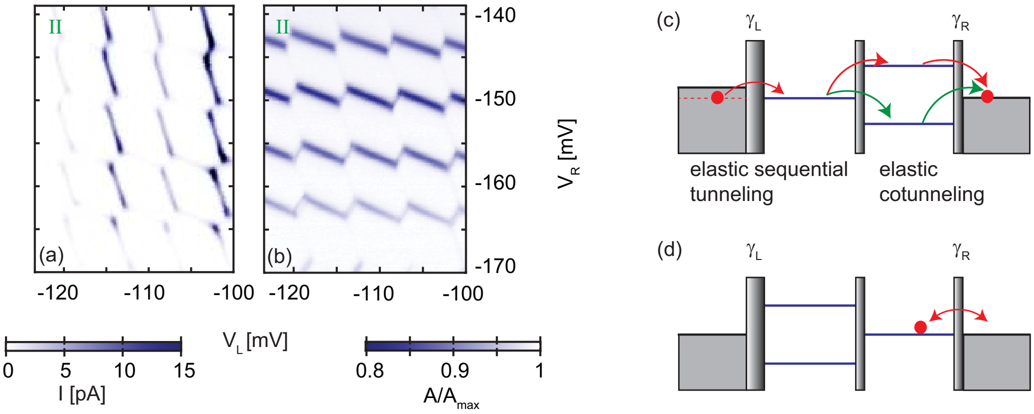

Figure 6.4: (a) Zoom of the direct current measurement in region II. (b) Magnified view of the relative transmission amplitude change in the same gate voltage range as in (a). (c,d) Schematic of the double quantum dot for the direct current measurement (c) and for the microwave measurement (d). γ_L and γ_R are the tunnel rates to the left and right lead, respectively.

For the transport measurements however, an electron must pass through both quantum dots for a current to be measured (Fig. 6.4 (c)). For sufficiently negative left side gate voltages ($V_L \lesssim -100$ mV), a cotunneling current can only be observed along two of the boundaries of the hexagon (Fig. 6.4 (a)). Along these lines the tunnel rate to the left dot is small, but since a dot level is resonant with the lead, first order tunneling is possible and the electron can enter the left dot. In order to now pass through the right dot, a cotunneling process needs to occur which requires a strong coupling between the right dot and lead [1]. An analogue explanation also holds for region III.

We conclude that the dominant mechanism for a change in the microwave transmission signal is the tunneling process of an electron back and forth between the lead and the dot, if only one of the dots is resonant with a lead and if the two dots are tuned more than the energy of a microwave photon apart, to exclude interdot photon assisted tunneling [7].

6.3 Measurement of the complex admittance for dot-lead tunneling processes

We have further investigated the response of the resonator close to dot-lead resonances (see Fig. 6.5). We now operate V_L and V_C at more negative gate voltages than in Fig. 6.3, in order to focus on tunneling events occurring between the right lead and the right quantum dot. This results in smaller tunnel rates to the left lead and between the dots. Whenever an electron in the right dot can resonantly tunnel to the lead, a drop in transmission amplitude is visible (6.5 (a,b)). We see

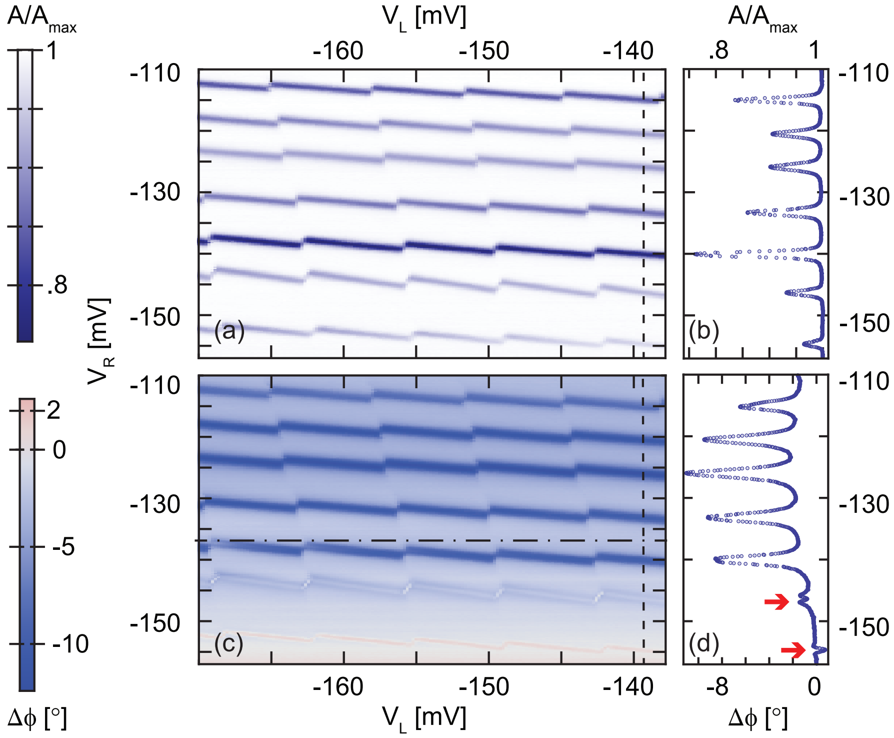

Figure 6.5: (a) Relative resonator transmission amplitude A/A_{max} at fixed measurement frequency as a function of V_{L} and V_{R}. (b) Relative amplitude change versus V_{R} along the dashed line shown in (a). (c) Phase change $\Delta\phi$ for the same gate voltage range as shown in (a) for a fixed measurement frequency ν_{M}. Dash-dotted line marks the upper border of the region displayed in detail in Fig. 6.6 (a). (d) Change of transmission phase along V_{R} as indicated in (c).

more interesting features however in the transmission phase (6.5 (c,d)), in which a characteristic change in the response occurs with decreasing V_{R} (i.e. decreasing tunnel rate to the lead). At first the change in phase $\Delta\phi$ is negative, indicating that the resonance frequency shifts to lower values. But at $V_{\text{R}} \approx -145$ mV, we observe a double peak in the phase response and for even smaller tunnel rates, the phase response becomes positive (highlighted in Fig. 6.5 (d) by red arrows).

This characteristic change in the phase response is seen for a range of different electron numbers in the left dot (Fig. 6.6 (a)). A further dataset indicating that this change in the phase signal depends on the tunnel rate between the right dot and the lead is shown in Fig. 6.6 (b). This is a dataset acquired in a similar regime, but the gate voltage parameters have slightly changed compared to Fig. 6.6 (a) due to a charge rearrangement in the system. Here the positive phase shift of the resonator evolves into a negative phase shift as the same dot-lead resonance is followed to more positive V_{R}, corresponding to an increasing tunnel rate (indicated by an arrow).

We have found that the width of the double peak in the phase signal does not depend on the microwave power over several orders of magnitude (Fig. 6.7 (a,b)).

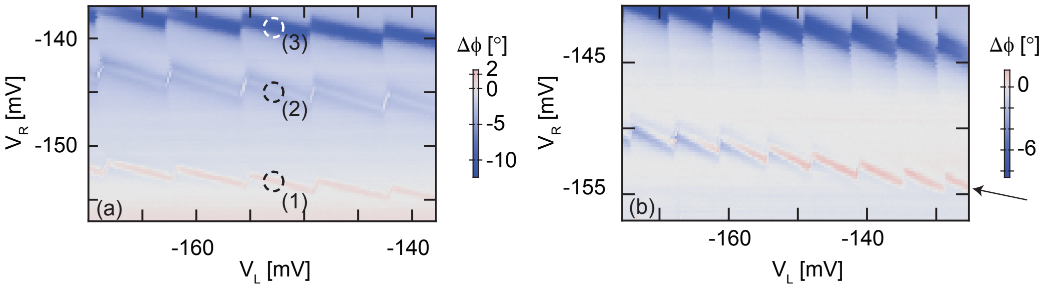

Figure 6.6: (a) Detailed view of the transmission phase in a selected region of V_{R} as indicated by a dash-dotted line in Fig. 6.5(c). Dashed circles refer to gate voltage settings investigated in more detail in Fig. 6.10. (b) Change of transmission phase $\Delta\phi$ at fixed ν_{M} as a function of V_{R} and V_{L} for a dataset acquired in a similar regime, but with slightly different gate voltages.

The indicated microwave powers in the figure refer to the power level at the output of the microwave generators.

We have also confirmed experimentally that the origin of the double peak in the phase signal is not caused by a current rectification process, as follows. We have measured the transmission phase with a low-frequency sinusoidal voltage signal (19.193 Hz) added to the drain-lead (D in Fig. 6.1) or the resonator gate (RG) via the inductor. As a result, the double peaked phase signal is smeared out and for increasing amplitudes of the sine signal, a double peak in the transmission amplitude of the resonator is observed. The transmission amplitude and phase when applying the low frequency signal to the drain contact is shown exemplarily in Fig. 6.8. The onset of a double peak structure in the amplitude signal can be observed for voltage amplitudes of around 120 μV or higher. The phase signal starts to flatten out for AC voltages of around 30 μV added to the drain contact.

We now discuss three characteristic measurements of the transmission phase in more detail which are recorded at the gate voltages highlighted by dashed circles in Fig. 6.6 (a). For these datasets, there is a nontrivial dependence of the frequency shift on the gate voltage V_{R}. We have measured the full microwave transmission spectra when tuning the right quantum dot through resonance with the lead for these three cases. We find for all measurements, that the transmission amplitude can be fitted with a Lorentzian from which we obtain the resonance frequency. For small shifts ($\Delta\nu \ll \kappa/2\pi$) it is directly proportional to the change in the transmission phase. In Fig. 6.10 (d) we plot the resonant frequency shift $\Delta\nu_0$ versus the change in right side gate voltage, where the resonances have been horizontally offset for better comparison. A small linear background phase (visible in Fig. 6.5 (d)) has been subtracted from the data in Fig. 6.10 (d). It is likely to originate from a slight change in direct capacitance between the resonator and the right lead.

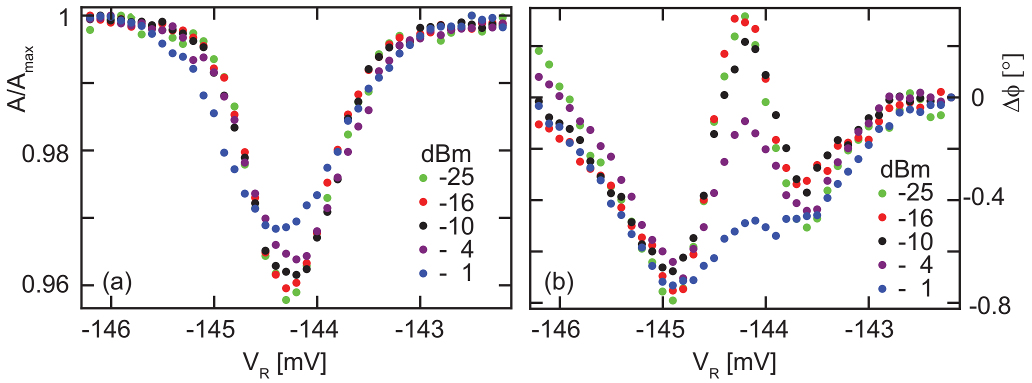

Figure 6.7: (a) Dependence of the relative amplitude signal $A/A_{\max}$ around a dot-lead resonance on the microwave powers applied to the resonator. (b) Phase shift $\Delta\phi$ of the microwave resonator for the same experimental settings as in (a). The datasets are acquired for the dot-lead resonance marked 2 in Fig. 6.6 (a), but with slightly different gate voltages for V_{L} and V_{R}.

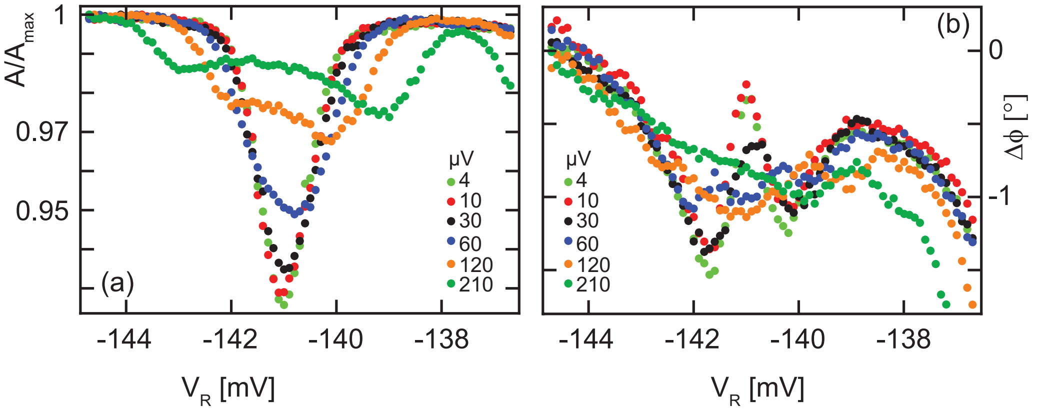

Figure 6.8: (a) Dependence of the relative amplitude signal $A/A_{\max}$ around a dot-lead resonance on the root mean square (rms) voltage strength of a low frequency 19.193 Hz signal applied to the drain contact. (b) Phase shift $\Delta\phi$ of the microwave resonator for the same experimental settings as in (a). The datasets are recorded for the dot-lead resonance marked 2 in Fig. 6.6 (a), but with slightly different gate voltages for V_{L} and V_{R}.

6.4 Modelling and interpretation of the results

For the interpretation of our data we use a scattering matrix approach [77], applicable for different kinds of coherent transport phenomena at DC but also for the case of finite frequencies (AC) (section 6.4.1). In section 6.4.2 we specify the finite frequency scattering matrix model for our experiment and compare the results of the calculations with the experimental data. An attempt to give an intuitive explanation of the observed complex admittance behavior concludes this section.

6.4.1 Scattering matrix model at finite frequencies

With decreasing sample sizes and setups operated in the millikelvin temperature range, it is possible to perform experiments where the phase coherence length (l_ϕ) becomes equal or even larger than the electronic structure (l_{es}) of the sample. In this situation, only elastic scattering plays a role in transport experiments and therefore phenomena related to wave-like transport can be studied. For these parameter settings ($l_\phi > l_{\mathrm{es}}$) transport is called coherent and was investigated e.g. in interference experiments of a single electron with itself, realized in a semiconductor heterostructure [42]. The scattering matrix approach known as the Landauer-Büttiker formalism has proven to be very useful to treat coherent transport theoretically [78].

In this section we summarize the basics of the scattering matrix model at finite frequencies developed by A. Prêtre, H. Thomas and M. Büttiker in Ref. [79]. A more detailed description can be found in this paper and the references therein, especially in Ref. [80].

The goal is to find a self-consistent algebraic expression, fulfilling charge and current conservation, for the AC conductance matrix in a mesoscopic conductor (see Fig. 6.9 (a)) using the scattering matrix formalism. In the DC case the conductance is fully described by the transmission probabilities. However, at finite frequencies the relative phases of the scattering matrices also play a role.

The conductor is connected via contacts to electron reservoirs which are at equilibrium described by a Fermi distribution function. In the contacts emission and absorption including, e.g., the relaxation process of the electrons, take place. To investigate the properties of the mesoscopic conductor, different voltage sources can be attached to the contacts.

Gates can be capacitively coupled to the conductor to tune it electrostatically. For clarity only one gate is plotted in Fig. 6.9 (a). The treatment of these gates must be included in the model used for finite frequency investigations: in contrast to the DC case they do not only have an electrostatic effect on the conductor but the dynamics in the system are also affected because of AC currents that can flow between the gates and the conductor.

The response of the system measured at one of the contacts (e.g. the oscillating current) due to a small perturbation, for example an AC voltage excitation on another contact, is computed in two steps. In the first step the response of the electrons, treated as noninteracting particles for now, caused by the external perturbation is considered. In the second step internal shifts in the potential (δU) due to Coulomb interaction between the electrons are taken into account self-consistently, ensuring charge conservation. For simplicity, we assume the presence of only one channel in each arm of the circuit in the following.

We start by motivating the equation for the first step of the calculations. An incoming wave from a particular contact, e.g. contact 1, can be either transmitted

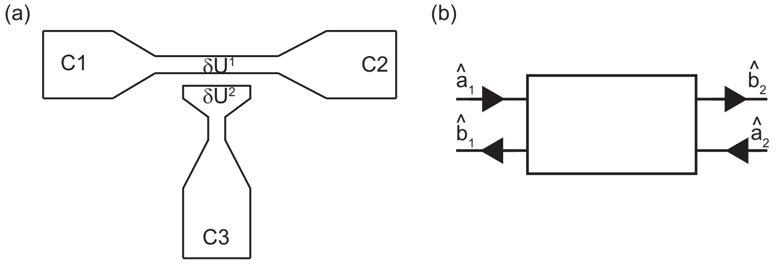

Figure 6.9: (a) Schematic of a mesoscopic conductor connected via two contacts C_1 and C_2. The conductor is capacitively coupled to a nearby gate tuned by contact C_3. Voltage perturbations can be applied to the contacts, leading to a change of the internal potentials δU^1 and δU^2. (b) Schematic of the scattering matrix approach in second quantization. Operators $\hat{a}_{\mathrm{x}}$ annihilate incoming particles, $\hat{b}_{\mathrm{x}}$ annihilate outgoing particles. The subscript x labels the contact the conductor is connected to.

through the mesoscopic conductor to another contact or reflected back. The outgoing signal to contact 1 is therefore the sum of the reflected wave and all the waves transmitted from the other contacts. Here this situation is described using second quantization with number operators $\hat{a}$ and $\hat{b}$ as shown in Fig. 6.9 (b). Operators $\hat{a}$ annihilate incoming states impinging on the electronic structure and operators $\hat{b}$ annihilate outgoing states. The two sets of operators are related to each other via the scattering matrix s:

$$\hat{b}_\alpha = \sum_\beta s_{\alpha\beta}\hat{a}_\beta, \tag{6.1}$$

where α, β label the contacts.

In order to calculate the oscillating current δI in linear response due to an external voltage perturbation, an expression for the current operator $\widehat{I}(t)$ is needed. The current density operator in the Heisenberg picture of quantum mechanics is defined as [81]:

$$\hat{j}(\mathbf{r},t) = \frac{\hbar}{2mi}[\hat{\Psi}^\dagger(\mathbf{r},t)\nabla\hat{\Psi}(\mathbf{r},t) - (\nabla\hat{\Psi}^\dagger(\mathbf{r},t))\hat{\Psi}(\mathbf{r},t)], \tag{6.2}$$

and the current is given by integrating $\hat{j}(\mathbf{r},t)$ over the cross section of the reservoir.

The field operator $\hat{\Psi}_\alpha$ in each contact is the sum of incoming and outgoing waves:

$$\hat{\Psi}_\alpha(\mathbf{r},t) \propto \int dE e^{i(k(E)x-\omega(E)t)}\hat{a}_\alpha(E) + e^{-i(k(E)x+\omega(E)t)}\hat{b}_\alpha(E). \tag{6.3}$$

Evaluating Eq. 6.2 using Eq. 6.3, and performing the integration over the cross section yields the following expression for the current in contact α:

$$\hat{I}_\alpha = \frac{e}{h}\int dEdE'[\hat{a}^\dagger_\alpha(E)\hat{a}_\alpha(E') - \hat{b}^\dagger_\alpha(E)\hat{b}_\alpha(E')]e^{i(E-E')t/\hbar}. \tag{6.4}$$

Expressing the $\hat{b}$ operators in Eq. 6.4 in terms of $\hat{a}$ operators using the scattering matrix (Eq. 6.1) results in

$$\hat{I}_\alpha = \frac{e}{h}\int dEdE' \sum_{\beta,\gamma} \hat{a}^\dagger_\beta(E) A_{\beta,\gamma}(\alpha, E, E')\hat{a}_\gamma(E')e^{i(E-E')t/\hbar}, \tag{6.5}$$

with the matrix $A_{\beta,\gamma}(\alpha, E, E')$ given as

$$A_{\beta,\gamma}(\alpha, E, E') = 1_\alpha \delta_{\alpha,\beta}\delta_{\alpha,\gamma} - s^\dagger_{\alpha,\beta}(E)s_{\alpha,\gamma}(E') \tag{6.6}$$

and the identity matrix 1_α.

So far we have calculated the full current operator. Now we continue using linear response theory to evaluate the current variation $\langle\delta I\rangle$ due to a voltage perturbation. It is assumed that the reference state is an equilibrium state with zero current in the leads.

The general formula for a linear response function of the observable $\hat{B}$ due to a perturbation in $\hat{A}$, also named Kubo formula in the literature, reads [82]:

$$\chi_{\mathrm{A,B}}(\mathbf{r}-\mathbf{r'}, t-t') = -\frac{i}{\hbar}\Theta(t-t') < [\hat{B}_{\mathrm{H}}(\mathbf{r}, t), \hat{A}_{\mathrm{H}}(\mathbf{r'}, t')] >, \tag{6.7}$$

where the index H indicates that the operators are expressed in the Heisenberg representation and the brackets $\langle\rangle$ stand for an ensemble average and the Θ function assures causality.

In our system the Hamiltonian of the perturbation reads

$$\hat{H} = \sum_\beta \hat{Q}_\beta \delta V_\beta, \tag{6.8}$$

where $\hat{Q}_\beta$ describes the total charge in reservoir β. The linear response equation using Eq. 6.7 and Eq. 6.8 becomes

$$\kappa^V_{\alpha,\beta}(\tau) = -\frac{i}{\hbar}\langle[\hat{I}_\alpha(\tau), \hat{Q}_\beta(0)]\rangle\Theta(\tau). \tag{6.9}$$

With Eq. 6.9 the function for the fluctuation of the current δI in linear response in Fourier space reads

$$\langle\delta I_\alpha(\omega)\rangle = \sum_\beta g^{\mathrm{ext}}_{\alpha,\beta}(\omega)\cdot\delta V_\beta(\omega), \tag{6.10}$$

with the external response

$$g^{\mathrm{ext}}_{\alpha,\beta}(\omega, \mu, kT, \gamma) = \frac{e^2}{h}\int dE\ \mathrm{Tr}[1_\alpha\delta_{\alpha,\beta} - \mathrm{s}^\dagger_{\alpha,\beta}(\mathrm{E},\gamma)\mathrm{s}_{\alpha,\beta}(\mathrm{E}+\hbar\omega,\gamma)]\left(\frac{\mathrm{f}_\beta(\mathrm{E})-\mathrm{f}_\beta(\mathrm{E}+\hbar\omega)}{\hbar\omega}\right). \tag{6.11}$$

In Eq. 6.11 the replacement $E' - E = \hbar\omega$ was used and the Fermi distribution functions originate from the quantum statistical average indicated with $\langle\rangle$ in Eq. 6.9.

After having dealt with the linear response of the system due to an external perturbation, leading to an accumulation of charge in the conductor, the resulting change of the local potential landscape is treated in the second step. The local potential landscape is modified by the redistributed electron configuration caused by electron-electron interactions. It is treated via geometrical capacitances $C_{\mathrm{m,n}}$. The letters m, n label the different conductors. For the example shown in Fig. 6.9 (a) we have two conductors so that $m, n = 1, 2$.

The total dynamic admittance then reads

$$g_{\alpha,\beta}^{(m,n)}(\omega) = \delta_{\mathrm{m,n}}\, g_{\alpha,\beta}^{\mathrm{ext(m)}}(\omega) - \left[\sum_{\gamma} g_{\alpha,\gamma}^{\mathrm{ext(m)}}(\omega)\right] (M^{-1})_{\mathrm{m,n}}(\omega) \left[\sum_{\delta} g_{\delta,\beta}^{\mathrm{ext(n)}}(\omega)\right]. \quad (6.12)$$

The matrix $M_{\mathrm{m,n}}(\omega) = \delta_{\mathrm{m,n}} \sum_{\alpha,\beta} g_{\alpha,\beta}^{\mathrm{ext(m)}}(\omega) - i\omega C_{\mathrm{m,n}}$ takes the interaction between the electrons into account and therefore assures charge conservation.

6.4.2 Comparison between model and experiment

In order to understand the observed frequency shifts of the resonator at different tunnel rates, we model the system using the scattering matrix approach described in the previous section. We neglect the presence of the left quantum dot in our model as the center gate voltage V_{C} is set so negative that electron tunneling between the dots is negligible. In addition, as the capacitance between the right plunger gate and the center gate and their capacitance to ground are much larger than their respective capacitances to the dot, we assume that they are always on the same microwave potential. This allows us to model the capacitive coupling of these two gates to the right dot by a single effective gate with a capacitance C_{Gs} (Fig. 6.10 (a)). In the model circuit, depicted in Fig. 6.10 (a), the resonator gate is coupled via a capacitor C_{RG} to the quantum dot and the drain contact (D) is tunnel coupled to the dot. The voltages V_{x} (x = dot, Gs, RG) are applied with external sources, and the voltage U_{dot} denotes the internal electrostatic potential of the quantum dot. This quantity arises due to the Coulomb interaction between charged particles in the dot, the lead and the gates and results in a local potential energy of electrons on the quantum dot as discussed in section 6.4.1. The dynamic admittance (Eq. 6.12) can be further simplified by approximating the density of states in the metal leads as being infinite, since it is much larger than the density of states in the quantum dot [83]. We calculate the dynamic admittance $g^{\mathrm{QD}}(\omega)$ of the quantum dot circuit in this approximation and find that the current flowing into the resonator gate is given by:

$$I_{\mathrm{RG}} = \left(\frac{1}{-i\omega C_{\mathrm{RG}}} + \frac{1}{g_{\mathrm{dot}}^{\mathrm{ext}}(\omega) - i\omega C_{\mathrm{Gs}}}\right)^{-1} \cdot V_{\mathrm{RG}} = g^{\mathrm{QD}}(\omega) \cdot V_{\mathrm{RG}}. \quad (6.13)$$

In this chapter we adopt the sign convention of previous authors [79], who define the Fourier transform of the current $I(t)$ as $I(\omega) = \int dt I(t) e^{-i\omega t}$. Therefore the complex admittance of a capacitor is $G(\omega) = -i\omega C$. The dynamic admittance $g^{\mathrm{QD}}(\omega)$ is capacitive for $\mathrm{Im}[\mathrm{g}^{\mathrm{QD}}(\omega)]/(-\omega) > 0$, and inductive for $\mathrm{Im}[\mathrm{g}^{\mathrm{QD}}(\omega)]/(-\omega) < 0$. Equivalent relations hold for the inductive or capacitive behavior of $g_{dot}^{ext}(\omega)$.

The lumped element representation of $g^{\mathrm{QD}}(\omega)$ (Eq. (6.13)) is shown in Fig. 6.10 (b). It consists of the parallel circuit of the capacitor C_{Gs} and the complex admittance of $g_{\mathrm{dot}}^{\mathrm{ext}}(\omega)$ in series with the coupling capacitor C_{RG}. In Eq. (6.13),

$$g_{\mathrm{dot}}^{\mathrm{ext}}(\omega, \mu, kT, \gamma) = \frac{e^2}{h} \int d\epsilon [1 - s^{\dagger}(\epsilon, \gamma) s(\epsilon + \hbar\omega, \gamma)] \left(\frac{f(\epsilon) - f(\epsilon + \hbar\omega)}{\hbar\omega} \right) \tag{6.14}$$

describes the external response of the quantum dot (Eq. 6.11) coupled to a single lead with an excitation with frequency $\omega/2\pi$. The two functions in $g_{\mathrm{dot}}^{\mathrm{ext}}$ are the scattering matrix $s(\epsilon, \gamma) = (1+i\epsilon/\gamma)/(1-i\epsilon/\gamma)$, describing in our analysis resonant reflection of Breit-Wigner type with the tunnel coupling strength γ, and the Fermi distribution $f(\epsilon, \mu, kT) = 1/(e^{[(\epsilon-\mu)/kT]} + 1)$. Here, μ describes the detuning in energy between the quantum dot level and the Fermi energy in the lead. It translates into a side gate voltage via $\mu = \alpha_{\mathrm{R}} V_{\mathrm{R}}$, where α_{R} is the lever arm of the right side gate. The external response $g_{\mathrm{dot}}^{\mathrm{ext}}(\omega, \mu, kT, \gamma)$ can be rewritten in terms of energy ratios $\hbar\omega/\gamma$, $\hbar\omega/kT$ and μ/kT. Its functional form is therefore completely determined by these three values. As C_{GND} is much larger than any other capacitances and as the dot is only modulated by the gate connected to the resonator, we assume that the source contact and the other gates are at microwave ground.

We also map the resonator to a lumped element model, (see Eq. (11-12) in [60]) and assume that the impedance of the coplanar waveguide resonator is 50 Ω to obtain the circuit model shown in Fig. 6.10 (c). To investigate the frequency shift $\Delta\nu$ of the resonator we evaluate the following equation

$$\Delta\nu = \frac{1}{4 \cdot 50\ \Omega (C_{\mathrm{rb}} + Y_{\mathrm{QD}})} - \nu_{\mathrm{offset}} \tag{6.15}$$

with $Y_{\mathrm{QD}} = \mathrm{Im}[\mathrm{g}^{\mathrm{QD}}(\omega)]/(-\omega)$ and ν_{offset} is a constant offset subtracted to obtain $\Delta\nu$.

Since the results of Eq. (6.13), (6.14), (6.15) depend on a number of parameters (C_{RG}, C_{Gs}, $\hbar\omega$, γ, kT, C_{rb}, α_{R}), we determine as many parameters as possible either by directly extracting their values from experimental data or using reasonable values, due to the given boundary conditions. We take $C_{\mathrm{RG}} = 56$ aF and $C_{\mathrm{Gs}} = 30$ aF, obtained from gate characterization measurements, and $C_{\mathrm{rb}} \approx 0.74$ pF, calculated from the resonator impedance and frequency. The electron temperature is estimated from Coulomb peak width measurements to be 135 mK and ω is set to $2\pi\nu_0$. A constant lever arm $\alpha_{\mathrm{R}} = 0.05$ is used to convert the energy scale to a gate voltage. This value of α_{R} is within less than a factor of two equal to the value obtained from finite bias measurements in another regime. The tunnel coupling γ is the only adjustable parameter. It is chosen to match the different data sets best and is in agreement with an upper bound obtained from the DC pinch off curve of the right side gate with the center gate and the left side gate open.

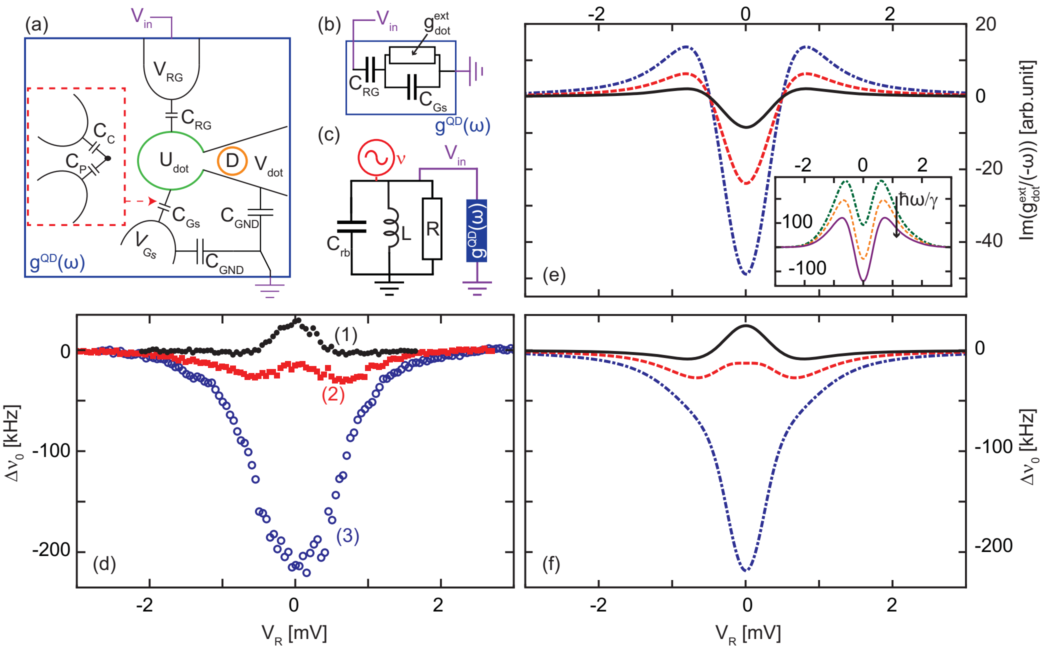

Figure 6.10: (a) Schematic of the right quantum dot tunnel-coupled to the drain lead (D). The dot is capacitively coupled to the resonator gate (RG) and to a capacitor (C_{Gs}) formed by the capacitive coupling of the center gate (C_{C}) and the right plunger gate (C_{P}). This circuit model is used to calculate the dynamic admittance $g^{\mathrm{QD}}(\omega)$ of the dot coupled to the lead. The V_{x} refer to the voltages applied by external voltage sources with x = dot, Gs, RG. U_{dot} describes the locally induced potential in the quantum dot. (b) Circuit representation of the schematic in (a), see Eq. (6.13) in the text. (c) Lumped element model (inductor L, resistor R, capacitor C_{rb}) of the microwave resonator with the dynamic admittance of the quantum dot connected in parallel. (d) Measured change of resonator frequency $\Delta\nu_0$ for the dot lead resonances (1-3) indicated by dashed circles in Fig. 6.6 (a). (e) Calculated imaginary part of the external admittance $g^{\mathrm{ext}}_{\mathrm{dot}}$ of the quantum dot (Eq. (6.14)) for tunnel couplings $\gamma_1/h = 20$ MHz (black), $\gamma_2/h = 58$ MHz (red), $\gamma_3/h = 125$ MHz (blue). Inset: Imaginary part of the external admittance for tunnel couplings $\gamma_4/h = 2$ GHz, $\gamma_5/h = 1.5$ GHz, $\gamma_6/h = 1$ GHz from top to bottom. (f) Results of the model calculations accordind to Eq. (6.15), for the three different tunnel couplings from top to bottom as in (e).

To compare the results of Eq. (6.15) with the data in Fig. 6.10 (d), we first show the complex admittance $g^{\mathrm{ext}}_{\mathrm{dot}}(\omega)$ for different ratios $\hbar\omega/\gamma$ between the energy of a microwave photon and the tunnel coupling. In the inset of Fig. 6.10 (e), the reactance $\mathrm{Im}[\mathrm{g}^{\mathrm{ext}}_{\mathrm{dot}}(\omega)]/(-\omega)$ is plotted for increasing values of $\hbar\omega/\gamma$. For the topmost curve, the response is capacitive for all gate voltages V_{R}. As the tunnel coupling is decreased, inductive behavior begins to develop close to resonance ($V_{\mathrm{R}} \approx 0$). The inductive response of the system is strong in the regime where $kT \ll \hbar\omega$ and $\gamma \ll \hbar\omega$. It starts to appear at $\gamma \approx \hbar\omega$ and $\gamma \gtrsim kT$.

The main part of Fig. 6.10 (e) shows the external response of the dot-lead system for parameters as used for the calculation of the resonator frequency shift in Fig. 6.10 (f). In all three cases an inductive behavior is observed close to resonance which turns into a capacitive response with detuning from the resonance.

The results of the evaluation of $\Delta\nu$ using Eq. (6.15) are shown in Fig. 6.10 (f). We compare the three different data sets in Fig. 6.10 (d) with these calculations and observe that the characteristic features of our measurements are well reproduced within this model. We find a dynamic admittance $g^{\mathrm{QD}}(\omega)$ with only a capacitive component for the most transparent tunnel barrier ($\gamma_3/h = 125$ MHz) of the three measurement sets presented in Fig. 6.10. The model also reproduces the crossover from a capacitive to an inductive behavior as the tunnel rate is reduced. For $g^{\mathrm{QD}}(\omega)$ the frequency γ/h where the transition between inductive and capacitive behavior occurs is shifted down from the GHz to the few tens of MHz-range due to the presence of the additional capacitances C_{Gs} and C_{RG}.

Comparing Figs. 6.10 (d) and (f) we find the measured curve (3) to be slightly broader in gate voltage than the corresponding calculated trace. Also the capacitive reactance in case (1) is slightly less pronounced in the measurement than in the calculated curve. Such differences between the scattering matrix model and the measurements could have a number of reasons. First, the model does not consider any sources of decoherence and noise. Second, the assumption of a Breit-Wigner-type phase dependence [1, 84], which is based on a single resonance, may be an oversimplification.

Detailed analysis of the resonator linewidth gives access to dissipative effects described by the real part of the dynamic admittance. For dataset (2) we obtain good agreement between model and data (Fig. 6.11) using the same parameters which describe the resonator frequency shift in Fig. 6.10. The model underestimates the dissipation by around a factor 2 in the other two cases. However, a comparison of the measured phase and amplitude changes in Figs. 6.5 (b) and (d) already suggests that the dissipative effects may be more difficult to describe than the reactive effects. While the latter show a systematic and steady evolution from the case of purely capacitive response to the case of inductive response with decreasing gate voltage, the dissipative effects vary strongly in the same gate voltage range. While we do not have a clear explanation for this effect at present, we point out that charge relaxation, which is still under investigation [85–87], is believed to play an essential role for high frequency resistance measurements.

6.4.3 Intuitive explanation of the complex admittance

In the following we propose an intuitive explanation for the appearance of an inductive and a capacitive response in the vicinity of a conductance resonance. The decisive parameter for the external response to be inductive or capacitive close to resonance with the lead, is the ratio between the photon energy $\hbar\omega$ and the tunnel coupling γ. As γ decreases at fixed frequency ω, the dwell time in the dot of a

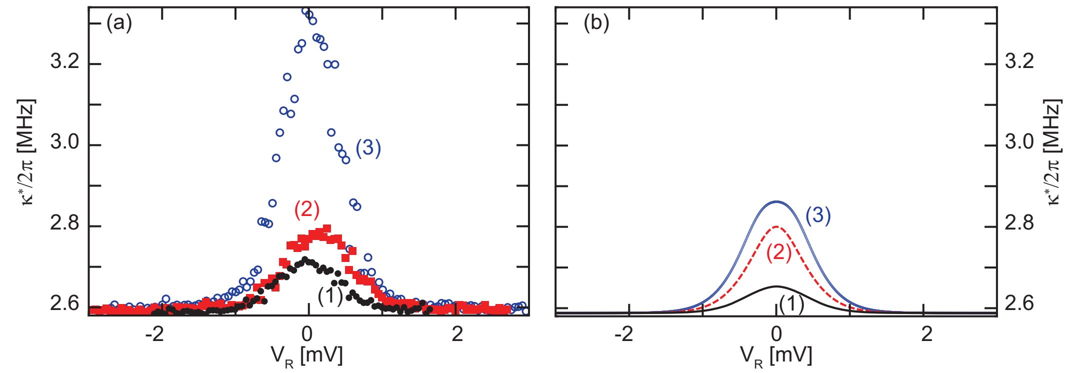

Figure 6.11: (a) Broadened linewidth κ^* for the three characteristic cases indicated in Fig. 6.6. Result of the model calculation using the real part of the complex impedance with the same parameters as stated in the caption of Fig. 6.10.

resonantly tunneling electron becomes longer. If this dwell time exceeds the period of the driving field, the electron can no longer follow the drive, the resulting current lags behind the voltage, and the response tends to be more and more inductive. This behavior may be interpreted as the quantum tunneling analogue of the kinetic inductance of an electron gas, which is due to the inertia of the electrons, and which causes a similar lag between current and voltage. However, in our resonant structure this inductive effect competes with the well-known contribution of the quantum capacitance to the response caused by the tunnel-broadened spectral density of the resonant state. The capacitive response prevails with increasing detuning from resonance, where tunneling of electrons into the dot has an increasing character of virtual transitions (elastic cotunneling) happening on very short time scales given by the detuning energy. This intuitive interpretation follows the discussion presented in Ref. [83].

Chapter 7

Dipole coupling of a double quantum dot to a microwave resonator

In this chapter we present measurements using the hybrid solid state quantum device introduced in chapter 6 to explore the dipole coupling between the semiconductor double quantum dot and the microwave field of the superconducting resonator. Both the observed frequency shift and the line width broadening of the resonator, recorded in the vicinity of an interdot charge transfer line of the double quantum dot, are explained by treating the double dot as a charge qubit coupled to the resonator with a strength of several tens of MHz.

7.1 Investigation of the interdot charge transfer line

We start with measurements investigating the properties of the double quantum dot for small tunnel coupling to the leads labeled region IV in chapter 6. The DC transport properties of the double quantum dot in this region are recorded by applying a source-drain voltage of $V_{\mathrm{SD}} \approx 50\ \mu\mathrm{V}$. To change the electrostatic potentials on the quantum dots the side gate voltages V_{L} and V_{R} are varied while all other gate voltages are kept constant. The voltages V_{L} and V_{R} are operated for these measurements close to their lowest possible value where the signal to noise ratio ($I_{\mathrm{min}} \gtrsim 80$ fA) still allows resolving the transmitted current (see Fig. 7.1 (a)).

We observe the typical hexagonal charge stability pattern, noticing that the signal starts vanishing due to the decreasing tunnel rates to the leads. The properties of the hexagons are discussed in chapters 2 and 6. This is why here we only point out the two hexagon boundaries, indicated by red arrows in Fig. 7.1 (a), at which no DC current is observed. These boundaries are named interdot charge transfer lines. Here two quantum dot energy levels with the same total number of electrons

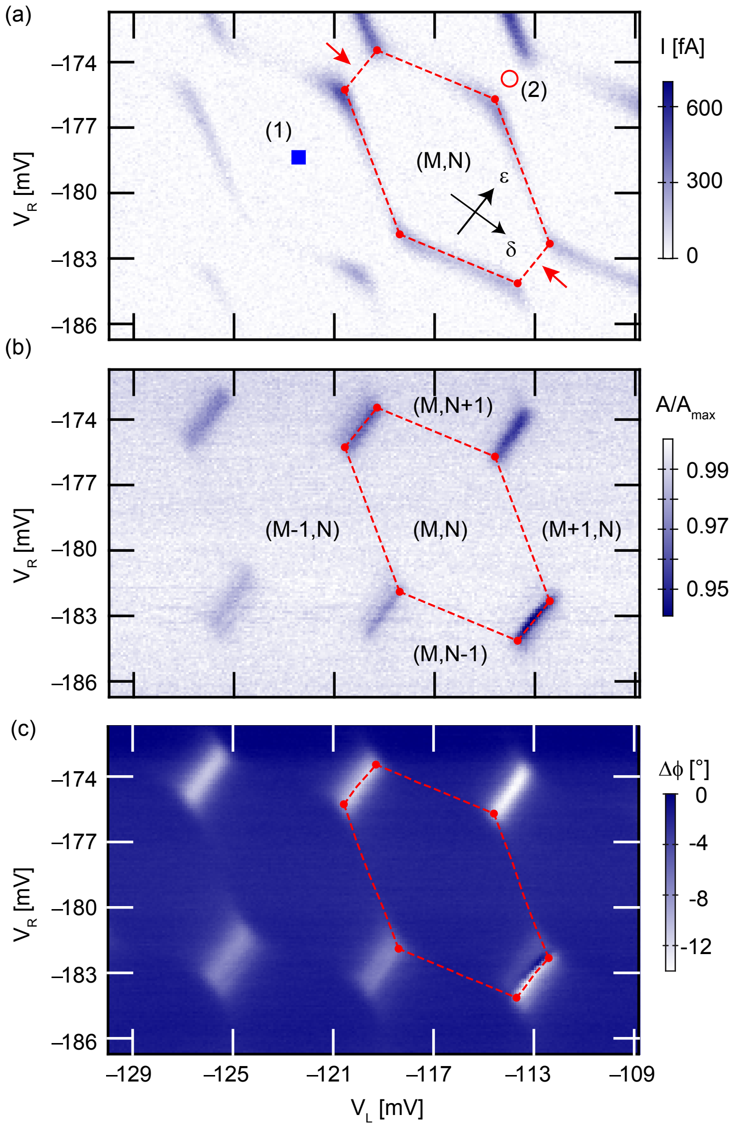

Figure 7.1: (a) Measurement of the direct current (I) through the double quantum dot versus V_{L} and V_{R} (no microwave signal applied). A small background current is subtracted from each horizontal line of the dataset. The dashed line outlines a region with fixed electron number (M,N). The ϵ and δ axes indicate the direction of the mean energy and the energy detuning of the two quantum dots. (b) Resonator transmission amplitude at fixed measurement frequency ν_{M} in the same gate voltage range as in (a). The red dashed lines highlight the same hexagon as in (a). (c) Transmission phase change with respect to the measurement tone of frequency ν_{M}, gate voltages as in (a). Red dashed lines as in (a).

are degenerate [2]. Along the interdot charge transfer line (Fig. 7.1(a)), the mean energy (ϵ) of the two quantum dots is tuned with respect to the chemical potentials of the leads. The energy detuning (δ) between the charge states of the quantum dots is changed along a second axis indicated in the same figure. The charging energies of both quantum dots are $E_\mathrm{C} \approx 1$ meV $\approx h \times 240$ GHz as extracted from Coulomb diamond measurements. We operate the quantum dots in the many electron regime where both quantum dots contain on the order of 100 electrons.

In Fig. 7.2(a) and (b), the amplitude and phase of the microwaves transmitted through the resonator are shown for the two voltage settings indicated with (1) and (2) in Fig. 7.1(a). Similar measurements are shown in chapter 6 (Fig. 6.2) but here in both configurations (1) and (2), transport is blocked between the leads and the quantum dots due to Coulomb blockade. However, in (1), the electron number in both dots is fixed, whereas in (2), a pair of left and right dot charge states are degenerate and hybridized states are formed. In the two cases, different resonance frequencies and maximum transmission amplitudes are observed. In contrast to the datasets shown in Fig. 6.2, the phase shift is more pronounced whereas the change in height of the amplitude is smaller. The modified resonator response indicates that the double dot couples with significant interaction strength to the resonator and that the coupling mechanism of the interdot charge transfer to the resonator is more of a reactive and less of a dissipative type. Remember that in all microwave transmission measurements presented in this chapter no source-drain bias is applied to the double dot.

For the same gate voltage ranges as shown in Fig. 7.1(a), we have measured the dependence of the amplitude and phase of microwaves transmitted through the resonator at fixed probe frequency ν_M with high resolution (Fig. 7.1(b,c)). We observe a clear reduction of the transmission amplitude and a change of the transmission phase at the charge triple points and along the inter-dot charge transfer lines connecting

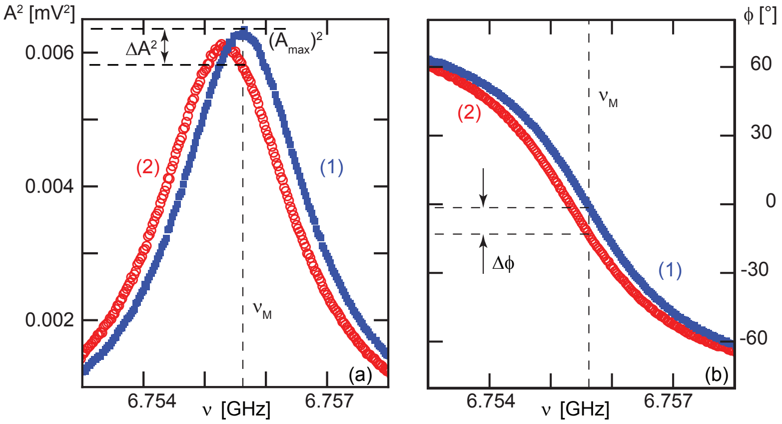

Figure 7.2: (a,b) Measured transmission spectra of the microwave resonator at positions (1) (blue rectangles) and (2) (red open points), indicated in Fig. 7.1(a). (a) Transmission amplitude and (b) phase.

pairs of triple points, but not in the regions with fixed electron numbers in both dots. Also, no change of the microwave signal is observed along the dot-lead resonant lines with these transmission settings of the tunnel barriers to the leads. In conclusion, in this parameter regime, a resonator response only occurs at gate voltages at which charges can be transferred between the two dots, leading to a dipole coupling to the resonator. Further details of the coupling mechanism are discussed below.

We double check that the charge stability diagram in the microwave measurement is well aligned in gate voltage with the one in the transport measurements, as indicated by the hexagon-patterns shown as red dashed lines in Figs. 7.1(a-c). Similar stability diagrams have been observed over a range of more than 10 electrons in both left and right dot. This range covers gate voltage settings at which the tunnel rates were so small that the DC current through the double quantum dot could not be detected in direct transport measurements ($I \lesssim 80$ fA) but also larger tunnel rates to the leads where a signal for dot-lead resonances could be detected in the microwave measurement (Fig. 6.3).

7.2 Influence of the interdot tunnel coupling on the resonator signal

We have examined in more detail the phase of the transmitted microwave signal in the vicinity of one particular interdot charge transfer line, for different values of interdot tunnel coupling energy t (Fig. 7.3). The coupling energy t can be tuned using V_C. Decreasing V_C reduces t. For these sets of measurements the two plunger gates $V_\mathrm{LP,RP}$ are swept (rather than $V_\mathrm{L,R}$), to minimize the change of the tunnel rates to the leads. The two side gates $V_\mathrm{L,R}$ are set such that the tunnel rates to the leads are too small to allow DC transport measurements.

At the largest tunnel-coupling between the two dots (least negative center gate voltage V_C) only a negative phase shift is observed in Fig. 7.3 (a). By decreasing the tunnel coupling, the size of the phase shift along the charge transfer line becomes smaller and finally changes the sign. At the smallest tunnel coupling (Fig. 7.3(f)) a clear positive phase shift is observed along the interdot charge transfer line. A negative phase is recovered with increasing detuning δ between the two dots. A quantitative discussion of these characteristic observations as well as model calculations are presented in the next section.

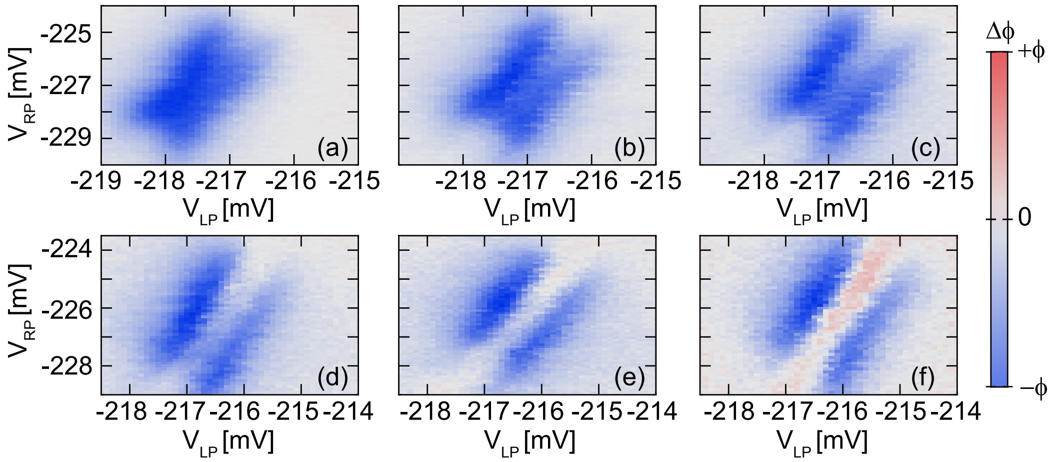

Figure 7.3: (a-e) Transmission phase measurements in dependence of the two plunger gate voltages V_LP and V_RP for different center gate voltages V_C and thereby different tunnel coupling between the dots. From (a-f) V_C is decreased in steps of 0.1 mV.

7.3 Interpretation of the measurement results

To interpret the data presented in this chapter, master equation simulations based on the Jaynes-Cummings model are performed.

First, we give an introduction to the master equation simulation on which the theoretical curves shown in Fig. 7.5 are based. Then we compare the results of the calculations with the measurements and discuss where they are in agreement and possible sources of deviations.

7.3.1 Jaynes-Cummings Model

This section is mainly based on private communications with Alexandre Blais, who set up the model used for simulations of our data, and on the references [13, 88].

To model the measurement data of our resonator quantum-dot device, we write down the total Hamiltonian of the system which reads

$$H_{\mathrm{total}} = H_{\mathrm{r}} + H_{\mathrm{q}} + H_{\mathrm{qr}} + H_{\mathrm{drive}} + H_{\mathrm{r,env}} + H_{\mathrm{q,env}}. \tag{7.1}$$

Here H_{r} is the Hamilton operator for the resonator, H_{q} describes the double quantum dot and H_{qr} takes the resonator double quantum dot coupling into account. H_{drive} models the coherent tone which we apply to the resonator with the microwave generator in the experiment. The operators $H_{\mathrm{r,env}}$ and $H_{\mathrm{q,env}}$ deal with the coupling of the resonator and the coupling of the double quantum dot to the environment, respectively.

We start out with the discussion of a Hamiltonian which only consists of the first three terms of H_{total} and in a later step present how we take the drive term and the interaction to the environment into account.

For the interpretation of our experiments the double quantum dot is modeled as a two-level system. It is therefore considered as a charge qubit [89] and the corresponding Hamiltonian reads

$$H_{\mathrm{q}} = \frac{\delta}{2}\sigma_{\mathrm{z}} + t\sigma_{\mathrm{x}}. \tag{7.2}$$

Here δ represents the energy detuning between the charge states of the quantum dots, t is the interdot tunnel coupling energy and $\sigma_{\mathrm{x,z}}$ are Pauli operators for the charge qubit. Diagonalizing the above Hamiltonian H_{q} leads to

$$H_{\mathrm{q}} = \frac{\hbar\omega_{\mathrm{q}}}{2}\sigma_{\mathrm{z}}, \tag{7.3}$$

where the qubit transition frequency $\omega_{\mathrm{q}}/2\pi$ is given by $\hbar\omega_{\mathrm{q}} = \sqrt{\delta^2 + (2t)^2}$ and $\tan\theta = 2t/\delta$.

The spectrum of the resonator consists of quantized light modes which we model as

$$H_{\mathrm{r}} = \hbar\omega_0\left(a^\dagger a + \frac{1}{2}\right) = \hbar\omega_0\left(\hat{n} + \frac{1}{2}\right), \tag{7.4}$$

where $\hat{n} = a^{\dagger}a$ is the photon number operator, and $\omega_0/2\pi$ the resonance frequency of the resonator.

We now focus on the coupling term H_{qr} between the resonator and the double quantum dot. The microwave photon field in the resonator leads to a small variation of the detuning (δ) between the two charge states in the double quantum dot. In our model this variation is described by a term acting along the direction of the σ_{z} operator. In the eigenbasis of the qubit defined by Eq. 7.3 the coupling term is found to be

$$\begin{aligned} H_{\mathrm{qr}} &= \hbar g(\sigma_{\mathrm{z}}\cos\theta - \sigma_{\mathrm{x}}\sin\theta)(a^{\dagger} + a) \\ &\approx -\hbar g \sin\theta (a^{\dagger}\sigma_{-} + a\sigma_{+}) \end{aligned} \tag{7.5}$$

where $\sigma_{+/-} = 0.5(\sigma_{\mathrm{x}} \pm i\sigma_{\mathrm{y}})$ and $\sigma_{\mathrm{x,y,z}}$ are the Pauli operators for the qubit. The maximal coupling strength g between the two systems is proportional to the dipole moment of the double quantum dot and the vacuum field fluctuations of the electric field (E_{rms}) of the resonator. For zero detuning ($\delta = 0 \Rightarrow \theta = \pi/2$) the coupling strength ($g\sin\theta$) of our setup can be estimated by [88]

$$g = \frac{\beta e}{\hbar}\sqrt{\frac{\hbar\omega_0}{cL}}. \tag{7.6}$$

Here β is defined as $\beta = \Delta\alpha$ and $\Delta\alpha$ is the difference between the leverarm of the resonator gate on the left dot and the leverarm of the resonator gate on the right dot. The smaller the capacitance per unit length (c) of the resonator and the shorter the resonator length (L) the larger the coupling strength becomes which amounts to reducing the mode volume.

In the second line of Eq. 7.5 we have performed the rotating wave approximation (RWA), meaning that only terms that keep the total number of excitations in the system constant are considered. This approximation is valid as long as $\omega_0 + \omega_{\mathrm{q}} \gg g$ [90].

In conclusion, the sum of the Hamiltonian of the resonator, the double quantum dot and their interaction reads

$$H_{\mathrm{JC}} = \hbar\omega_0\left(\hat{n} + \frac{1}{2}\right) + \hbar\frac{\omega_{\mathrm{q}}}{2}\hat{\sigma}_{\mathrm{z}} - \hbar g \sin\theta(\hat{a}^{\dagger}\hat{\sigma}^{-} + \hat{a}\hat{\sigma}^{+}). \tag{7.7}$$

Note that for a single qubit the sign of g can be chosen arbitrarily. In general models treating the interaction between a quantized light mode and a two-level system, as described above, are referred to be of Jaynes-Cummings type [91].

In Fig. 7.4, the two lowest eigenenergies of the coupled system described by H_{JC} are shown schematically as a function of δ for the two cases (a) $2t < h\nu_0$ and (b,c) $2t > h\nu_0$. Here the energies are offset in such a way that $E = 0$ corresponds to the energy of the vacuum field. In the presence of an interaction of strength g, the bare resonator frequency ν_0 (dashed green line) and the bare charge qubit transition frequency ν_{q} (dotted red line) are coupled by the interaction to give the solid black

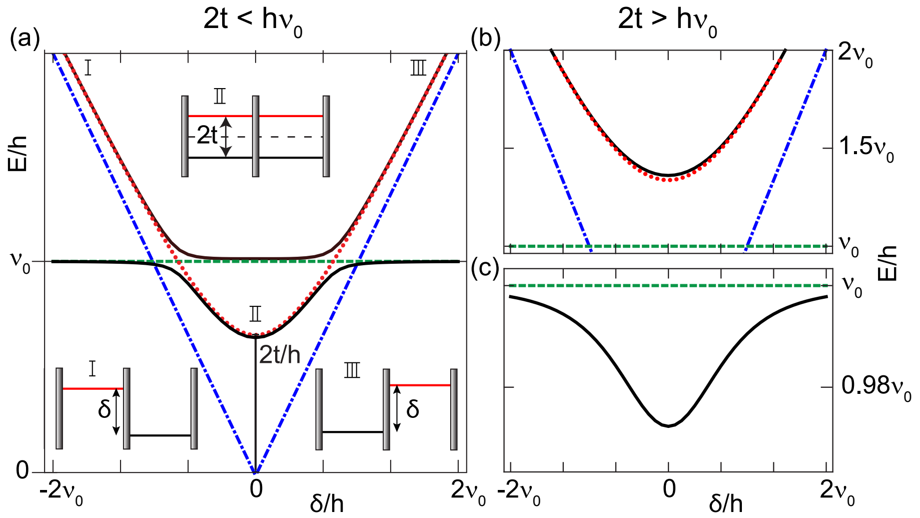

Figure 7.4: (a) Schematic of the two lowest eigenenergies of the coupled system (black line) for $2t < h\nu_0$. Horizontal green dashed line indicates the bare resonator frequency ν_0. Red dotted line shows the bare transition frequency ν_q between the double dot charge states. The two sloped blue dashed-dotted lines indicate the detuning δ. Insets I, III: Schematic of the two double dot charge states detuned by energy δ, in the limit $\delta \gg t$. Inset II: Schematic of the hybridized charge states in the double quantum dot, split by $2t$ at $\delta = 0$. (b) Transition energy of the charge qubit for $2t > h\nu_0$ in the presence of the nearby resonator (black line). Dashed and dotted lines as in (a). (c) Resonator frequency in the presence of the nearby charge qubit transition (black line) for the same case as in (b).

lines shown in Fig. 7.4(a). In the absence of decoherence, this model displays an avoided level crossing at $\nu_\mathrm{q} = \nu_0$ known as the vacuum Rabi mode splitting [92].

In the following we now discuss how the coupling of our system to the environment is treated. We begin with the presentation of the master equation and continue with the discussion of the individual parameters entering it.

As mentioned above the resonator and the double quantum dot also couple to the environment leading to an open quantum system [93]. On the one hand interaction with the environment is necessary in the experiment because the resonator needs to couple to the leads to be able to measure the transmission signal. On the other hand there are also unwanted coupling mechanisms of the resonator to the environment reducing its quality factor (see chapter 4 for details) and also unwanted coupling of the double quantum dot to the environment leading to dissipation and dephasing of its charge states. Possible processes of charge states coupling to the environment leading to decoherence are e. g. gate voltage fluctuations, phonons and fluctuators within the wafer [89, 94–99].

If we take the interaction with the environment into account the evolution is no longer reversible and we use a Markovian master equation approach instead of the Schrödinger equation to describe the dynamics of the system. The master equation reads [92]

$$\begin{aligned}\dot{\rho} &= -\frac{i}{\hbar}[H,\rho] + \kappa\mathcal{D}[a]\rho + \gamma_1\mathcal{D}[\sigma_-]\rho + \gamma_\varphi\mathcal{D}[\sigma_z]\rho/2 \\ &\equiv \mathcal{L}\rho,\end{aligned} \tag{7.8}$$

with $\mathcal{D}[O]\rho = (2O\rho O^\dagger - O^\dagger O\rho - \rho O^\dagger O)/2$ which is named in the literature as the Lindblad operator and discussed further below.

The first part in Eq. 7.8 takes the unitary evolution of the system into account. H is the sum of the Jaynes-Cummings Hamiltonian H_{JC} (Eq. 7.7) and the drive of the resonator H_{drive}. For the Hamiltonian of the drive we use

$$H_{\mathrm{drive}} = \hbar\epsilon\cos(\omega_{\mathrm{d}}t)(a^\dagger + a), \tag{7.9}$$

where ϵ is the drive strength and $\omega_{\mathrm{d}}/2\pi$ the frequency of the drive. The three other terms in the master equation account for decay of photons from the resonator at a rate κ, decay of the qubit state at a rate γ_1, and qubit pure dephasing at a rate γ_φ.

The decay rates will be treated in more detail below but first we want to come back to the Lindblad operator and mention the essentials for its derivation. We refer the interested reader for more details to the literature e. g. Ref. [13] and Ref. [92]. We start out by having a closer look at Hamiltonians $H_{\mathrm{s,env}}$ describing interaction between a quantum system (s) and an environment (env). For a weak coupling they can be written in the form

$$H_{\mathrm{s,env}} \propto k(a^\dagger b + ab^\dagger). \tag{7.10}$$

The operators a ($a^\dagger$) create (annihilate) an excitation in the quantum system (s) and b ($b^\dagger$) are the corresponding operators for the environment (env). The coupling strength between quantum system and environment is proportional to k. The corresponding equation for the the density matrix $\zeta(t)$ of the quantum system plus environment in an interaction picture [92] reads

$$\frac{d\zeta(t)}{dt} = -\frac{i}{\hbar}[H_{\mathrm{s,env}}(t),\zeta(t)]. \tag{7.11}$$

This equation can be solved iteratively and approximated by only considering perturbations up to second order which is justified due to the weak coupling. In the next step of the calculation the trace over the degrees of freedom of the environment is taken, assuming that at time zero the density matrix of our system and the environment are uncorrelated. In the last step of the derivation of the Lindblad operator we apply the Markov approximation. In essence this implies that the environment has a short memory meaning no correlations between the environment and the quantum system are built up.

In the case of $\delta \gg t$, we calculate expressions for the energy relaxation (γ_1^{b}) and for the pure dephasing rate ($\gamma_\varphi^{\mathrm{b}}$), using the above discussed approximations. We obtain

$$\begin{aligned}\gamma_1^{\mathrm{b}} &= \frac{S_{\mathrm{x}}(\omega=\delta/\hbar)}{\hbar^2}\\ \gamma_\varphi^{\mathrm{b}} &= \frac{S_{\mathrm{z}}(\omega\to 0)}{\hbar^2},\end{aligned} \tag{7.12}$$

where $S_{\mathrm{i}}(\omega)$ stands for the spectrum of the reservoir being of relevance for the $i=\{x,z\}$ qubit axis. Examples of the calculations of the spectra can be found in Ref. [100] and Ref. [101].

As pure dephasing and relaxation are specified for the eigenstates of the system, we have to calculate the corresponding rates in the diagonalized basis of the qubit Hamiltonian H_{q} (Eq. 7.3). Further, we implement the first assumption that the noise sources acting on the detuning axis and on the tunneling coupling axis are considered to be independent. Note that the validity of this and the further assumptions is discussed at the end of section 7.3.2 when we compare the theory to the experiment. We obtain for the two rates

$$\begin{aligned}\gamma_1 &= \sin^2\theta\frac{S_{\mathrm{z}}(\omega=\delta/\hbar)}{\hbar^2}+\cos^2\theta\frac{S_{\mathrm{x}}(\omega=\delta/\hbar)}{\hbar^2},\\ \gamma_\varphi &= \cos^2\theta\frac{S_{\mathrm{z}}(\omega\to 0)}{\hbar^2}+\sin^2\theta\frac{S_{\mathrm{x}}(\omega\to 0)}{\hbar^2}.\end{aligned} \tag{7.13}$$

The basis transformation implemented for the above calculations can be conceived as a rotation on the Bloch sphere around the y-axis which leads to the substitutions

$$\begin{aligned}\sigma_{\mathrm{z}} &\to \sigma_{\mathrm{z}}\cos\theta-\sigma_{\mathrm{x}}\sin\theta\\ \sigma_{\mathrm{x}} &\to \sigma_{\mathrm{z}}\sin\theta+\sigma_{\mathrm{x}}\cos\theta.\end{aligned} \tag{7.14}$$

The second assumption is that the spectrum of the noise is approximated to be white. This leads to the following new equations for the rates

$$\begin{aligned}\gamma_1 &= \sin^2\theta\gamma_\varphi^{\mathrm{b}}+\cos^2\theta\gamma_1^{\mathrm{b}},\\ \gamma_\varphi &= \cos^2\theta\gamma_\varphi^{\mathrm{b}}+\sin^2\theta\gamma_1^{\mathrm{b}}.\end{aligned} \tag{7.15}$$

The photon decay rate κ is defined in Eq. 4.2. It is the larger the stronger the capacitive coupling between resonator and the leads of the resonator are and the higher the internal loss in the resonator is, as discussed in detail in chapter 4.

To simplify the calculations, the system is investigated in a rotating frame using a unitary transformation with the corresponding operator U defined as

$$U(t)=e^{i\omega_{\mathrm{d}}t(a^\dagger a+1/2\sigma_{\mathrm{z}})}. \tag{7.16}$$

As a consequence the eigenstates of the system ($|\Psi>$) transform to the new eigenstates in the rotating frame ($|\widetilde{\Psi}>$) according to the equation

$$|\widetilde{\Psi}>=U(t)|\Psi>, \tag{7.17}$$

and the corresponding transformation of the Hamiltonian reads

$$\widetilde{H} = U(t)HU^{\dagger}(t) - U(t)i\hbar\frac{d}{dt}U^{\dagger}(t). \tag{7.18}$$

To evaluate Eq. 7.18 the relations

$$e^{i\omega_{\mathrm{d}}ta^{\dagger}a}ae^{-i\omega_{\mathrm{d}}ta^{\dagger}a} = ae^{-i\omega_{\mathrm{d}}t} \tag{7.19}$$

and

$$e^{i\omega_{\mathrm{d}}t\sigma_z/2}\sigma_{+}e^{-i\omega_{\mathrm{d}}t\sigma_z/2} = \sigma_{+}e^{i\omega_{\mathrm{d}}t} \tag{7.20}$$

are used.

Due to the unitary transformation H_{JC}, as defined in Eq. 7.7, is changed to

$$H_{\mathrm{JC}} = \hbar(\omega_0 - \omega_{\mathrm{d}})\left(\hat{n} + \frac{1}{2}\right) + \hbar\frac{(\omega_{\mathrm{q}} - \omega_{\mathrm{d}})}{2}\hat{\sigma}_{\mathrm{z}} - \hbar g\sin\theta(\hat{a}^{\dagger}\hat{\sigma}^{-} + \hat{a}\hat{\sigma}^{+}), \tag{7.21}$$

and the drive term using again the rotating wave approximation, as already discussed in Eq. 7.5, is modified to

$$H_{\mathrm{drive}} = \hbar\frac{\epsilon}{2}(a^{\dagger} + a). \tag{7.22}$$

All the other terms in the master equation are not altered by the unitary transformation. For the simulation in the rotating frame we therefore only have to replace H in the master equation Eq. 7.8 with the sum of Eq. 7.21 and Eq. 7.22.

In the last part of this section we want to focus on the evaluation of the density matrix ρ obtained from the employment of the discussed master equation approach. In the simulations, the steady state of the system (ρ_{s}) ($\dot{\rho}$ is set to zero in Eq. 7.8) is calculated with a fixed drive strength (ϵ) for different sets of drive frequency ($\omega_{\mathrm{d}}/2\pi$) and detuning between the two dots (δ). Further input parameters for the simulation are the bare resonance frequency ($\omega_0/2\pi$) and the decay rate (κ) which are experimentally determined. The parameters tunneling energy (t), maximal coupling strength (g), dissipation rate (γ_1) and pure dephasing rate (γ_{φ}) are chosen to fit the experimental datasets best. Another input parameter of the simulation is the considered number of photon states (n_{num}) in the resonator.

In the experiment the resonator is driven with a coherent tone. This leads to a Poissonian distributed population of the photon number states in dependence of the drive strength (ϵ). For $\delta \gg t$ the mean number of photons (n_{mean}) in dependence of the drive strength (ϵ) and the resonator linewidth (κ) can be estimated using [102]

$$n_{\mathrm{mean}} = \frac{(\epsilon/2)^2}{(\omega_0 - \omega_{\mathrm{d}})^2 + (\kappa/2)^2}. \tag{7.23}$$

Therefore the choice of the input parameter (n_{num}) must be correlated with n_{mean} to obtain a correct simulation result.

The transmission amplitude through the resonator is obtained by calculating $\langle a\rangle_s = \mathrm{Tr}[a\rho_s] = I + iQ$, where the index s indicates the steady state. From the square of the calculated transmission amplitude signal, the shift of the resonance frequency ($\Delta\nu_0$) and the broadened linewidth of the resonator (κ^*) can be obtained and compared with the experimental data.

Note that in the simulation used for explaining our data, we did not consider the influence of thermal photons in the resonator and also not the excited state population of our two-level system due to its finite temperature. The setup for the measurements (see chapter 3) is engineered such that these parameters have a minor influence on the measurement results.

7.3.2 Comparison between experiment and theory

For two different values of interdot tunnel coupling energy t, we have examined the phase of the transmitted microwaves in the vicinity of one particular interdot charge transfer line in more detail. The tunnel coupling is tuned using V_{C}. In order to discuss the experimental data as clearly as possible, we assume in the following that $2t$ can be larger or smaller than the resonator energy $h\nu_0$. We justify this assumption after the presentation of the data with the quantitative model based on the Jaynes-Cummings Hamiltonian presented in section 7.3.1. To change the detuning δ between the two quantum dots, the two plunger gates $V_{\mathrm{LP,RP}}$ are swept (rather than $V_{\mathrm{L,R}}$), in order to minimize the change of the tunnel rates to the leads. $V_{\mathrm{L,R}}$ are set such that the tunnel rates to the leads are too small to measure DC transport. The data shown in the left (right) column of Fig. 7.5 has been acquired with the center gate set to $V_{\mathrm{C}} = -120$ mV(-119 mV) corresponding to $2t$ smaller (larger) than $h\nu_0$, as discussed below. Despite the small change in V_{C} between the two measurements, the two phase signals are clearly different. Note that in these measurements the sweep ranges of the two plunger gates are chosen such that the detuning $\Delta = \nu_{\mathrm{q}} - \nu_0$ between the resonator frequency ν_0 and the qubit transition frequency ν_{q} is changed over a frequency range larger than the resonator frequency. In Fig. 7.5(a), two regions of negative phase shift are observed on either side of a region of positive phase shift along the interdot charge transfer line. In Fig. 7.5(b) however, a single region of negative phase shift is seen, similar to the features shown in Fig. 7.1(c) and Fig. 7.3. Negative/positive phase shifts translate directly to negative/positive resonance frequency shifts (see Fig. 7.2(a) and (b)).

To characterize the interaction between the two systems in more detail, we have measured the full resonator transmission spectrum for a set of gate voltages across the interdot charge transfer line (black line in Fig. 7.5(a,b)). For all parameters, the measured spectra are well approximated by a single Lorentzian line. The extracted frequency shifts $\Delta\nu_0$ relative to ν_0 and the extracted linewidths κ^* are plotted in Fig. 7.5(c-f) for the two different interdot tunnel coupling strengths. In agreement with the data in Fig. 7.5(a,b), for $2t < h\nu_0$ both negative and positive frequency shifts are observed in the left panel whereas for $2t > h\nu_0$ only negative frequency shifts are seen in the right panel. In both cases an increase in κ^* is observed when the energy difference between two charge states is close to the resonator frequency.

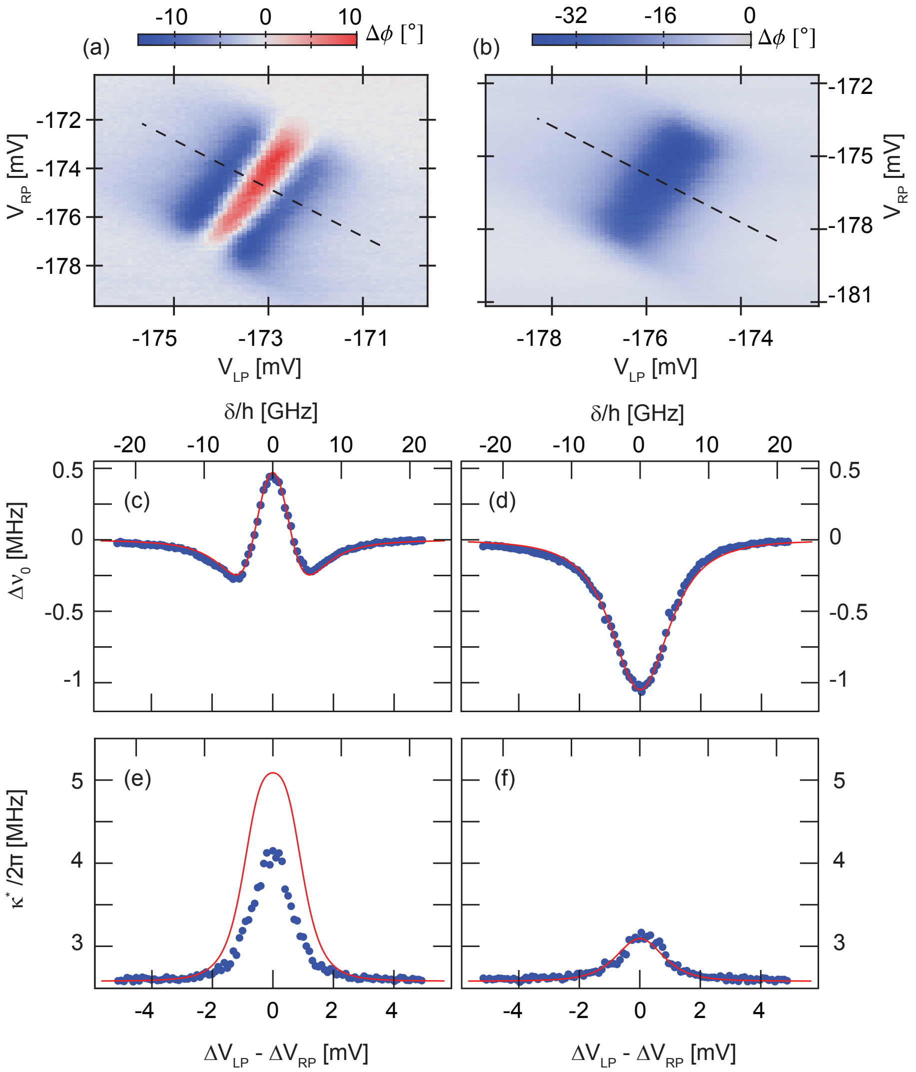

Figure 7.5: a) Measured transmission phase as a function of V_{LP} and V_{RP} at $V_C = -120$ mV (with $2t < h\nu_0$, as extracted from simulations). Black dashed line indicates axis swept in (c,e). (b) Transmission phase measured at $V_C = -119$ mV (with $2t > h\nu_0$ from simulations). Black dashed line indicates axis swept in (d,f). (c,d) Measured resonator frequency shift $\Delta\nu_0$ (blue points) along the axes shown in (a) and (b) respectively. (e,f) Broadened resonator linewidth κ^* (blue points) measured along the axes shown in (a) and (b) respectively. Solid red lines in (c-f) are results of numerical simulations.

In the following we compare these observations with model calculations. We use the Markovian master equation approach described in section 7.3.1 to obtain a steady-state numerical solution of the Hamiltonian Eq. (7.7) including resonator and qubit energy relaxation and qubit pure dephasing [100]. This approach allows us to explain the characteristic features of the data shown in Fig. 7.5(c-f). Indeed, using the measured values of ν_0 and κ, choosing an energy relaxation rate at $\delta \gg t$

of $\gamma_1/2\pi = 100$ MHz typical for charge qubits [103], and using a constant factor related to the difference between lever arms of the left and right quantum dot to convert gate voltage to detuning energy (δ), we find that all simulations are in reasonable agreement with the data, see red lines in Fig. 7.5(c-f). To achieve this agreement, we consider a maximal coupling strength of $g/2\pi = 50$ MHz for all data sets but take a tunnel energy $2t/h = 6.1$ GHz $< \nu_0$ and a pure dephasing rate $\gamma_\varphi/2\pi = 3.3$ GHz at $\delta \gg t$ for Fig. 7.5(c,e) and $2t/h = 9$ GHz $> \nu_0$, and a smaller value of $\gamma_\varphi/2\pi = 0.9$ GHz at $\delta \gg t$ for Fig. 7.5(d,f). The order of magnitude of the values found for the dephasing rates at $\delta = 0$ within our model are comparable to those found in other quantum dot charge qubit experiments [89]. The estimated value of g considered here agrees within an order of magnitude with an estimate obtained from the capacitive coupling between qubit and resonator using Eq. 7.6. Since the qubit pure dephasing rate γ_φ is in both cases significantly larger than the maximal coupling strength g we do not observe a vacuum Rabi mode splitting, but rather a single spectral line broadened and shifted from its original frequency. At detunings Δ between the double dot charge states and the resonator that are on the order of or larger than the qubit linewidth we can clearly observe frequency shifts induced by the non-resonant coupling [88]. We conclude that the size of the observed shifts is in good agreement with our model.

For this set of extracted parameters, we also note that the measured linewidth (Fig. 7.5(e)) is lower than the one found from our calculation and the rate for the pure dephasing (γ_φ) changes between the two investigated cases. This discrepancy is potentially due to the frequency dependence of the noise that leads to decoherence which is not considered in our model where the noise was considered to be white. This is probably an oversimplification and a better knowledge of $S_\mathrm{x}(\omega)$ and $S_\mathrm{z}(\omega)$ in dependence of ω is required for a better noise treatment. In addition the fluctuations of the tunnel coupling were considered to be independent of the fluctuations of the detuning which might be a vague assumption as the noise on e.g. the center gate voltage V_C changes the tunnel coupling but due to the cross capacitive effects also the detuning between the two dots. To increase the validity of the simulation results, in future experiments more of the input parameters should be extracted by experimental means e. g. by performing microwave spectroscopy of the double quantum dot as previously demonstrated with superconducting qubits [104].

To double check the conclusions from our simulations, we have confirmed both experimentally and in simulation that the results in Fig. 7.5 are independent of changes in the resonator population due to coherent or thermal fields with a mean occupation of below approximately 10 photons. This observation is reasonable, since the large pure dephasing rate makes the rather small changes due to the nonlinearities arising at larger photon numbers [105] unobservable in the current experiments.

Chapter 8

Conclusion and Outlook

In this thesis we have designed novel hybrid devices consisting of quantum dots and microwave resonators integrated on one chip. The cleanroom processes necessary to fabricate such samples were developed and employed successfully. A setup was built to be able to perform measurements on the hybrid quantum devices in the sub-kHz regime and at microwave frequencies.

The properties of the two building blocks (quantum dot, microwave resonator) were investigated individually and the coupling between the two systems was explored in two different manners.

On the one hand, the effect on the transport properties of the quantum dot in dependence on an electromagnetic field in the resonator, which is capacitively coupled to the quantum dot system, was characterized. The presence of the microwave field leads to a decrease of the conductance through the quantum dot which increases with the field strength. This property could be explored to detect harmonic modes of the cavity over a frequency range of around 30 GHz measuring the DC transport signal. From these results, the quality factor of the fundamental mode of the resonator was extracted [106].

On the other hand we have successfully demonstrated the dipole coupling of a double quantum dot to an on-chip superconducting microwave resonator, and probed the double dot charge stability diagram by measuring resonator frequency shifts. Two different characteristic regimes with interdot tunnel coupling frequencies above or below the resonator frequency could be observed and interpreted consistently with a master equation simulation approach based on the Jaynes-Cummings model [107].

We also explored the tunneling process between a quantized state in a single dot and the 2DEG continuum for different tunnel rates. Carrying out these measurements using a microwave frequency resonator enabled us to observe a crossover from a capacitive to an inductive response [108]. The observations are well described within the scattering matrix model of Ref. [79]. Our interpretation of the phase shift data is of particular relevance for similar experiments coupling a microwave resonator to a single [109] or double quantum dot [110, 111]. In particular, Ref. [110] reports similar phase shifts but without discussion or interpretation.

Our measurements demonstrated that our architecture offers a new way to probe semiconductor quantum dot systems in the microwave regime, and may be used, for example, for high energy-resolution measurements of double quantum dots [112], in addition to being a promising platform for potentially scalable hybrid solid-state quantum information processing. The presented scheme could be extended to other material systems, manipulating and reading out spin qubits [3, 111] and coupling them to a microwave resonator using either ferromagnetic leads [113] or spin orbit effects [114] or coupling to the interdot tunnel gate [115].

Moreover our measurement scheme promises the feasibility of future experiments in which the sensitivity of the resonator is further exploited, e.g., in measuring the shot noise properties [116, 117] of a quantum point contact in more detail.

Appendices

A Double quantum dot measurements with a microwave resonator at finite source-drain bias

In this section we investigate the influence of a source-drain voltage V_{SD} on the charge stability diagram of the hybrid quantum dot resonator sample shown in Fig. 6.1. Finite bias triangles can be measured in transport experiments, as already discussed in chapter 2, for $eV_{\mathrm{SD}} > k_{\mathrm{B}}T_{\mathrm{e}}$ and eV_{SD} larger than the energy broadening of the Coulomb resonances of the quantum dots due to tunnel coupling. We compare the results of the DC measurements with the corresponding microwave measurements for which we use the techniques described in chapter 6.

In Fig. A.1 a set of current measurements through the double quantum dot is shown for different source-drain voltages (V_{SD}). We vary the two side gate voltages V_{L} and V_{R} (see Fig. 6.1) to change the electrostatics in the double quantum dot. The onset of finite bias triangles is observed. Their size and the current through the dots increase with V_{SD}. As the voltages applied to the two side gates do not only change the electrostatic potential of the two dots but also decrease the tunnel coupling to the leads, the current for more pinched off gate voltages is smaller.

We observe additional structures in the current signal through the quantum dots in some of the triangles. These features are especially pronounced for the triangles in the upper left corner when a negative bias voltage is applied (Fig. A.2 (b,d,f)). The most likely origin of these discrete resonances in the current signal is a tunneling process involving an excited state [2].

The edges of the triangles are smeared out due to the finite electron temperature (T_{e}). We also recognize that the cotunneling lines become more pronounced with bias voltage which can also lead to a deformation of the triangles.

We repeat measurements at different finite source-drain voltages for the same topgate voltages as shown in Fig. A.1 but record the relative transmission amplitude and phase (see Fig. A.2) through the resonator. We observe that the positions in gate voltage space of the interdot charge transfer lines, which form the base lines of the triangles, are at the same position as in the DC measurements. In addition the lengths of the base lines increase with the applied bias voltage. In the transmission amplitude signal in Fig. A.2 (a-f) a faint outline of finite bias triangles can be recognized. In all triangles the base lines cause the most pronounced change in the

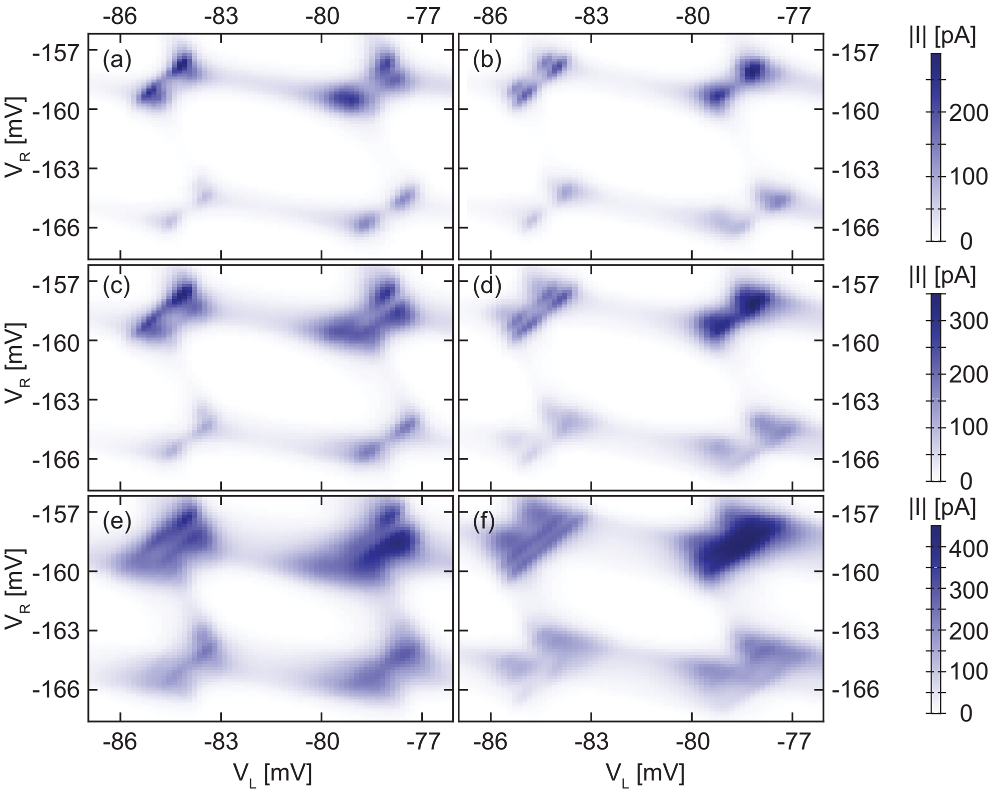

Figure A.1: Current measurements through the double quantum dot shown in Fig. 6.1 for the following six different voltages (V_{SD}) applied between the source and the drain contacts. (a) $V_{\mathrm{SD}} = 100\ \mu$V, (b) $V_{\mathrm{SD}} = -100\ \mu$V, (c) $V_{\mathrm{SD}} = 150\ \mu$V, (d) $V_{\mathrm{SD}} = -150\ \mu$V, (e) $V_{\mathrm{SD}} = 250\ \mu$V and (f) $V_{\mathrm{SD}} = -250\ \mu$V.

amplitude signal and in some cases the tips of the triangles (e. g. in (d,e)) are also visible. Our interpretation for this observation is that in these cases electrons can resonantly leave or enter the quantum dots leading to a change of the transmission amplitude signal. For some of the triangles, especially the top right triangle in (c,f), there is also a slight reduction of the transmission amplitude observable within the triangles. We guess that due to the limited electron lifetime in the quantum dots by the non-resonant current flow within the triangles, an additional loss channel for the resonator is created leading to a reduction of the transmission amplitude. For the bottom right and top left triangles in (a), the tips of the triangles are not pronounced but a rather well distinct continuous line parallel to the base line can be observed.

A discrete set of lines is visible in the transmission phase (Fig. A.2 (g-l)) but not the outline of the triangles. We observe that the distance between the lines does not change with the applied bias. As for the transmission amplitude the base line is clearly detectable. The origin of the signal can be explained due to the presence of two quantum dot states with an energy difference close to the energy of the

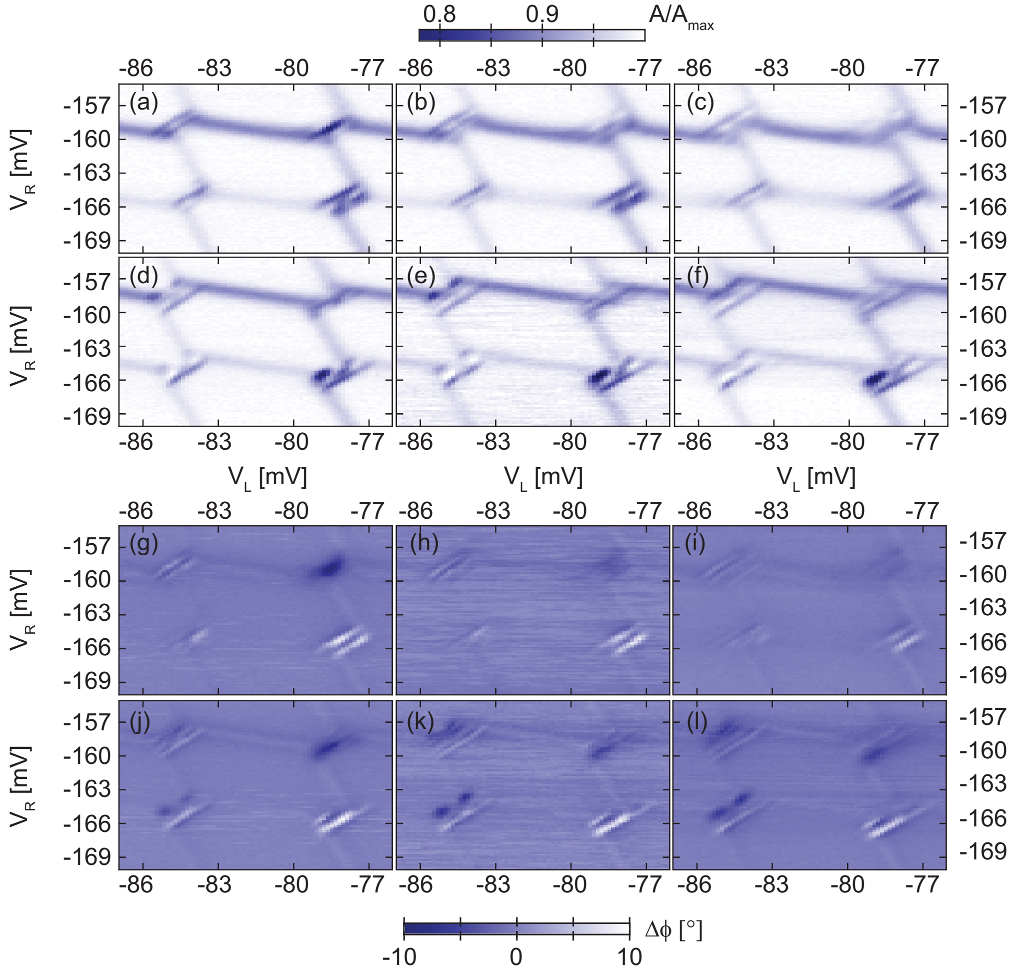

Figure A.2: Relative transmission amplitude and transmission phase change measurement of the microwave resonator for different source-drain voltages (V_{SD}) for the same topgate voltage settings (V_{C}, V_{LP}, V_{RP}) as used for the measurements shown in Fig. A.1; (a,g) $V_{\mathrm{SD}} = 100\ \mu$V, (b,h) $V_{\mathrm{SD}} = 150\ \mu$V, (c,i) $V_{\mathrm{SD}} = 200\ \mu$V, (d,j) $V_{\mathrm{SD}} = -100\ \mu$V, (e,k) $V_{\mathrm{SD}} = -150\ \mu$V, (f,l) $V_{\mathrm{SD}} = -200\ \mu$V.

microwave photons. This causes a shift of the resonator as explained in chapter 7.

We speculate that the discrete lines of the transmission phase change or transmission amplitude change within the finite bias triangles are related to the presence of possible transitions between the two dots involving excited states. Our assumption is motivated by comparing the top left triangle in the DC measurement (Fig. A.1 (a)) with the corresponding microwave measurement in Fig. A.2 (a). The distance between the resonance within the triangle and the base line in the gate voltage space is about the same in the DC case and in the microwave case. This suggests a relation of the resonances within the triangles of the microwave measurements to excited states. The reason why there is additional structure seen in the microwave measurements but not in direct current measurements could be explained by the fact that these excited states do not couple to the leads well and therefore cannot be detected in transport experiments.

We also measure the microwave signal at zero source-drain bias for the same topgate voltages as used in Figs. A.1, A.2 and plot the results of the relative transmission amplitude in Fig. A.3 (a) and the change in phase in Fig. A.3 (b).

In the phase signal we observe that in three cases it changes sign when crossing the interdot charge transfer line whereas in one case there is only a negative phase shift in the vicinity of the interdot charge transfer line. The origin of the characteristic behavior in the phase signal is assumed to be the same as discussed for the data in chapter 7. In the amplitude signal (Fig. A.3 (a) top left) two pronounced lines, caused by a change in the transmission amplitude, are measured. They are parallel to the interdot charge transfer line.

We investigate this double feature in the amplitude signal in more detail. The measurement results are displayed in Fig. A.3 (c,d). In (d) we again see the change of the sign of the phase when we cross the interdot charge transfer line. We note that the shift in the phase signal is more pronounced between the two triple points than in the vicinity of the triple point. We therefore speculate that the size of the phase shift is related to the coherence time of the charge state which is longer between than at the triple points. This is plausible because between the triple points electron exchange with the leads is prohibited to first order [2].

We obtain a split interdot charge transfer line in the amplitude signal. The bottom end of the upper line is more pronounced than the top end and the opposite is observed for the lower line. A measurement doubling the power sent through the microwave resonator did not change the size of the splitting.

To continue our investigation we measure full resonator transmission spectra along the black dashed line indicated in Fig. A.3 (c,d). The resonance spectra always display a Lorentzian line shape and the corresponding fit allows us to extract the change of the resonance frequency ($\Delta\nu_0$) and the broadened resonator line width κ^*. We observe the characteristic change of the resonance frequency as discussed in detail in chapter 7. A double peak structure is clearly visible for the resonator linewidth κ^* which is different from the other datasets which we obtained so far. The splitting is estimated to be roughly the energy of the microwave photons by comparing it to gate characterization measurements at DC.

The shift of the resonator frequency, around 100 kHz at maximum, and the change of the resonator linewidth κ^* are rather small compared with the datasets shown in Fig. 7.5. We know from the simulations done for the datasets shown in Fig. 7.5 that a double peak structure in the resonator linewidth signal indicates a smaller decoherence rate than used for the simulations of the datasets in chapter 7. The splitting between the two peaks would be related to the detuning between the energy of the photons in the resonator and the tunnel coupling energy between the two dots.

An increase of the coherence would however be rather surprising because in this

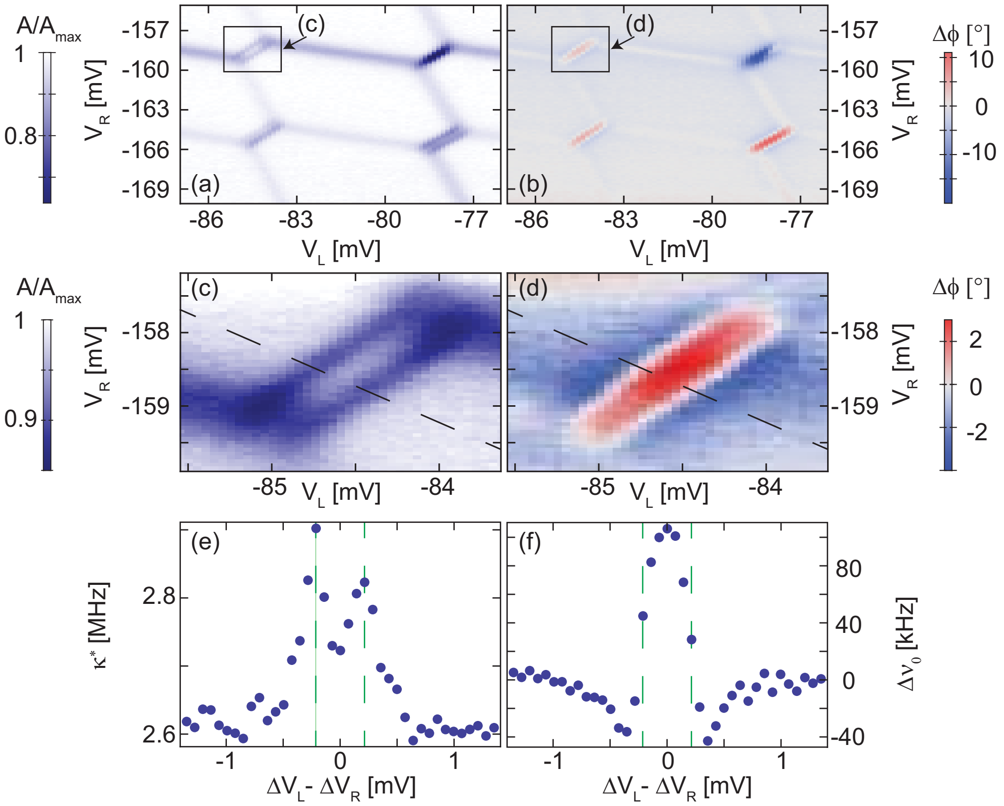

Figure A.3: (a) Relative transmission amplitude measurement for the same topgate voltages as used in Fig. A.2 but $V_{\mathrm{SD}} = 0$ V and (b) corresponding transmission phase measurement. (c,d) Zoom-in measurement of the relative transmission amplitude (c) and the transmission phase (d) as indicated in (a), (b) respectively. (e) Broadened resonator linewidth κ^* measured along the dashed line shown in (c,d). (f) Measured resonator frequency shift $\Delta\nu_0$ along the dashed line shown in (c,d).

region the coupling to the leads is stronger than for the previously examined datasets (Fig. 7.5), and cotunneling currents were claimed to be a major source of decoherence for charge qubits [89]. Concerning the other sources of decoherence for charge states such as coupling to phonons, fluctuations in the wafer material etc., it is not obvious why they should change compared to the corresponding measurements performed in this thesis.

While we do not have a clear explanation for the double feature in the linewidth and future investigations are necessary to clarify the origin of this signal, a possible explanation is that an excited state is involved in these measurements. The energy difference between an excited state and the ground state could be similar to that of the microwave photons. In the finite bias case we concluded that excited states can cause a change of the microwave signal.

For completeness we mention that split interdot charge transfer lines in double quantum dot structures were also observed in charge sensing measurements using quantum point contacts [118].

B Microwave measurements of quantum dot properties for very low tunnel coupling to the leads

In this section we present measurements in which the tunnel coupling to the leads is significantly decreased in comparison to the settings used in chapter 7. The aim is to improve the coherence properties of the charge states by increasing the isolation of the quantum dots from the environment.

The two side gate voltages V_L and V_R (Fig. 6.1) are swept and the relative change of the transmission amplitude and the relative change in phase are recorded as shown in Fig. B.4. The two side gate voltages mainly modify the tunnel coupling to the leads. Due to the finite capacitive cross coupling they also tune the electrostatic potential in the dots, which alters the number of electrons in the quantum dots as discussed in chapter 6.

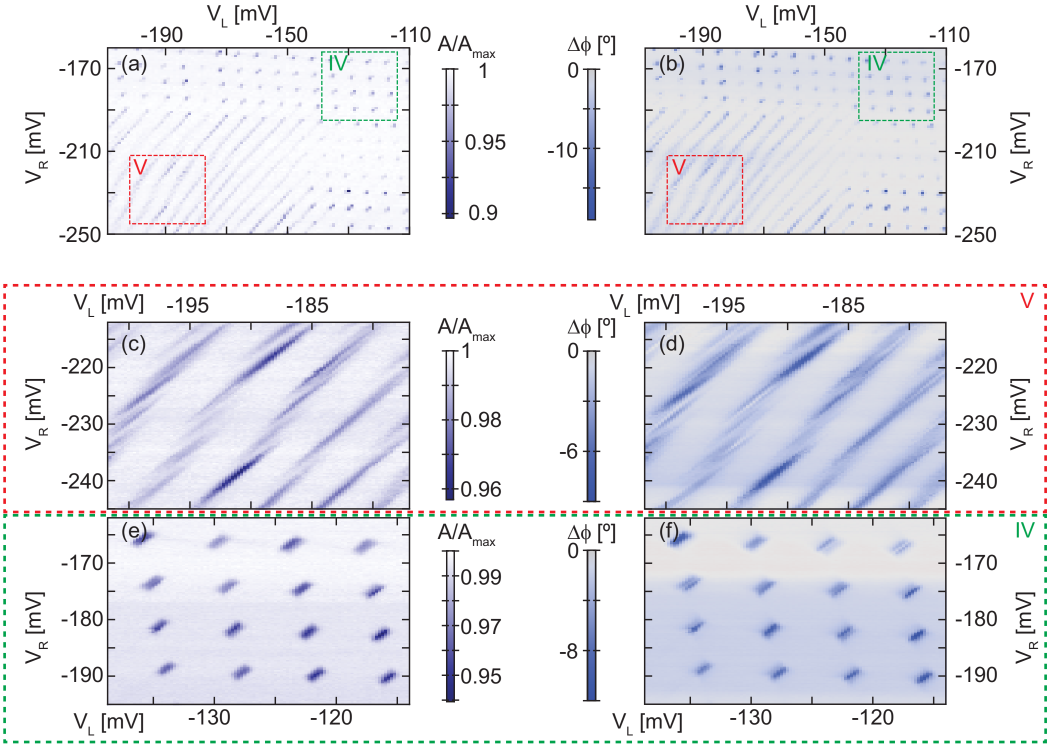

Figure B.4: Microwave transmission measurements of the double quantum dot charge stability diagram using the sample shown in Fig. 6.1. Relative amplitude transmission measurements (a,c,e) and corresponding measurements of the phase change (b,d,f) in dependence on the side gate voltages V_L and V_R. Rectangles in (a) and (b) mark regions for the detailed measurements shown in (c,d) (red) and (e,f) (green).

At around $V_\mathrm{L} \lesssim -130$ mV and $V_\mathrm{R} \lesssim -190$ mV we notice a characteristic change in the amplitude as well as in the phase signal. For less negative voltages and therefore larger tunnel coupling we only observe the interdot charge transfer lines as discussed in the context of Fig. 6.3. However, for smaller tunnel coupling the area where we measure a change of the microwave transmission signal begins to extend and a set of parallel lines shows up.

We investigate this region with the small dot-lead tunnel rates, which we refer to as region V from now on, in more detail and compare it to the other region labeled IV defined in Fig. 6.3. The two positions for the detailed measurements are outlined with a green dashed rectangle for region IV and a red dashed rectangle for region V. The corresponding data is shown in Fig. B.4 (c,d) for region V and (e,f) for region IV.

In region IV a set of distinct interdot charge transfer lines are visible in the amplitude and in the phase signal as expected from the overview measurement. We refer to chapter 7 for the interpretation of the origin of the signal.

For region V a set of parallel distinct lines is visible both in the amplitude as well as in the phase signal as anticipated from Fig. B.4 (a) and (b). The individual lines have a substructure consisting of a set of shorter lines especially pronounced in the gate voltage region for $V_\mathrm{L} = -185$ mV to $V_\mathrm{L} = -195$ mV and $V_\mathrm{R} = -220$ mV to $V_\mathrm{R} = -235$ mV.

We continue to investigate region V to explore the properties of this novel observations in the charge stability diagram. A set of experiments, in which the averaging time of the microwave signal as well as the sweep direction of the gate voltages were changed, are presented in Fig. B.5. The influence of these parameters on the transmission properties of the microwave resonator is investigated in detail. The results in Fig. B.4 suggest that the transition between the two regions is related to the tunnel coupling rate to the leads in comparison to the inverse of the measurement time.

For the measurements shown in Fig. B.5, the side gate voltages are fixed at $V_\mathrm{R} = -200$ mV and $V_\mathrm{L} = -155$ mV - close to the transition between regions IV and regions V. The two plunger gates are used to change the electrostatic potential in the quantum dots. The use of the plunger gates has the benefit that the modification of the tunnel coupling to the leads is minimized.

The dataset, which is shown in Fig. B.5 (a,b), is used as a reference measurement. The left plunger gate voltage (V_LP) is always swept in the same direction, afterwards the right plunger gate voltage V_RP is stepped before a new sweep of the left plunger gate is started. The sweep and step direction is towards more negative gate voltages. All datasets, which are shown in Fig. B.5, are recorded with an estimated average photon number of the order of 20 in the resonator. To extract the I- and Q-quadratures from a single time trace without averaging would take about 20 μs. In (a,b) each measured point is averaged 4096 times to increase the signal to noise ratio resulting in a total measurement time per point of approximately 82 ms.

We observe that the microwave signal consists of extended lines with discrete

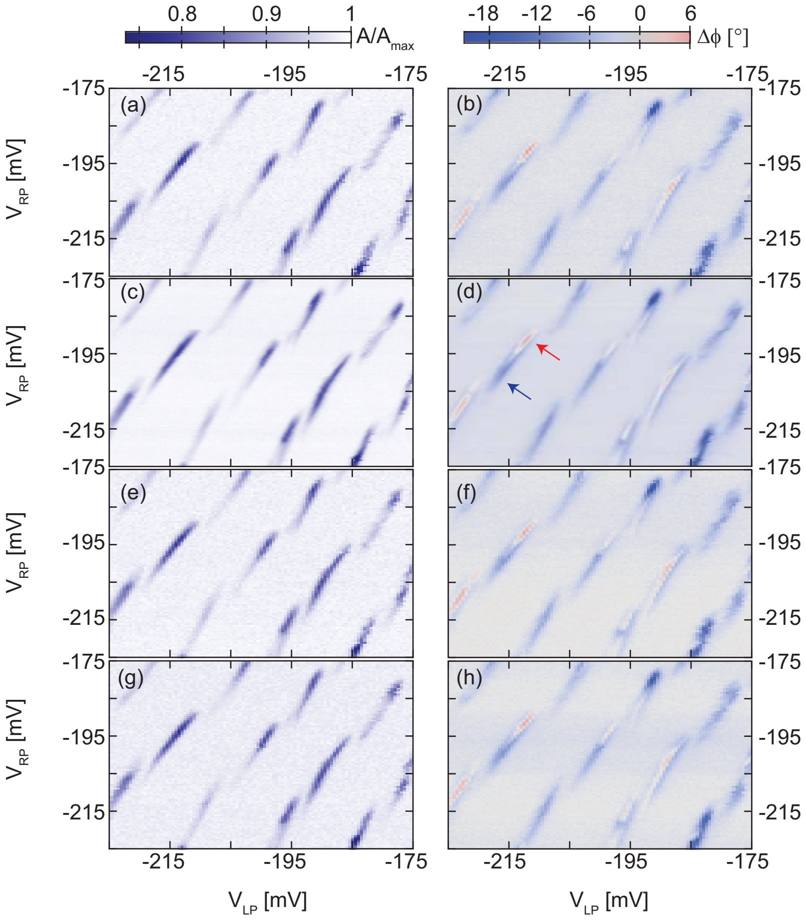

Figure B.5: Measurement of the relative transmission amplitude (a,c,e,g) and the corresponding change in phase (b,d,f,h) in dependence on the right and left plunger gate ($V_{\mathrm{LP}}, V_{\mathrm{RP}}$) for different parameters (stated further below) for the sample shown in Fig. 6.1. Roman numbers indicate different characteristic measurement regions (see text for details). (a,b) Reference measurement with $V_{\mathrm{R}} = -200$ mV, $V_{\mathrm{L}} = -155$ mV, $V_{\mathrm{C}} = -120$ mV. To record one single point of the measurement takes approximately 82 ms. (c,d) as (a,b) but averaging the microwave signal four times more and double the number of points along each axis. (e,f) as (a,b) but inverse the stepping direction of the right plunger gate (V_{RP}). (g,h) as (a,b) but both gates (V_{LP}, V_{RP}) swept in opposite direction.

jumps at the start of a new line. The amplitude signal of the majority of these lines is the most pronounced at the beginning of each line. The interspace between the start of two different lines is about equal to the distance between two sets of neighboring triple points in region IV. This indicates that the discrete jumps are related to a new set of charge states in the quantum dots which are energetically possible to be occupied by electrons tunneling from the leads.

A peculiarity in the phase signal is that some of the observed lines change their characteristics. This is most pronounced for the signal starting at around $V_{\mathrm{LP}} = -208$ mV and $V_{\mathrm{RP}} = -188$ mV in Fig. B.5 (b). At the beginning of the line (indicated with a red arrow in Fig. B.5 (d)) we observe a change of the sign in the phase when the line is crossed. However, only a negative phase shift is measured when the plunger gate voltages are further reduced (blue arrow in in Fig. B.5 (d)). We use the same interpretation as in chapter 7 for the origin of the phase sign change. In one case the resonator is above the transition frequency of the involved quantum dot charge states and vice versa. We conclude that the tunnel rate between the two dots changes for these measurements. A possible explanation for the different tunnel coupling strengths could be that due to the different electrostatic potential, the position of the wave functions of the two charge states is altered leading to a stronger coupling between them. Another reason could be that the tunnel coupling between the two dots is not independent of the mean energy ϵ of the double quantum dot, but gets stronger with ϵ. Note that we also changed the microwave power by a factor of four but no influence on the measurements could be detected.

In Fig. B.5 (c,d) we increase the number of points by a factor of two along each axis and increase the number of averages by a factor of 4 to check the influence of the time during which the electron has the possibility to tunnel into the leads. We observe that the signal to noise increases but otherwise no significant change can be found.

The influence of the sweep and step direction is investigated in Fig. B.5 (e,f) and (g,h). In (e,f) the step direction of the right plunger gate is reversed but the sweep direction of the left plunger gate is kept as in (a,b). In (g,h) the step and the sweep direction are inverted in comparison to the measurements shown in (a,b). In both cases we cannot find any influence on the measurement results due to these parameters. We conclude that time-constants related to loading of the quantum dots are not relevant for these sets of experimental data.

To further explore the properties of region V we use the same measurement parameters as in Fig. B.5 (a) but add a bias voltage of 100 μV or -100 μV. The results of the two bias voltages are overlayed in Fig. B.6 to simplify the comparison. No onset of finite bias triangles can be observed which is ascribed to the small tunnel rate to the leads. The difference between the two measurement sets is a slight offset which we interpret as the capacitive influence of the leads.

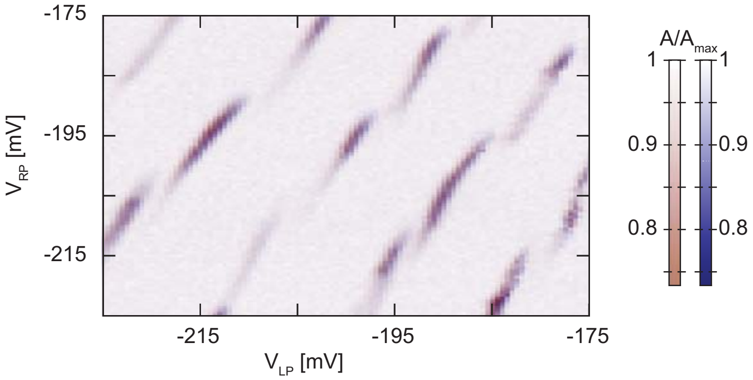

Figure B.6: Overlay of two microwave transmission measurements for two different DC voltages - 100 μV (red color scale) and -100 μV (blue color scale) - applied between the source and the drain contact. The rest of the settings are the same as used in Fig. B.5 and further details are discussed in the text.

C Single electron double quantum dot devices

In the next step of the experiment the goal is to study if there is an influence of the number of electrons in the double quantum dot on the coherence properties of the hybrid quantum devices. Double quantum dots operated at the last electron have been implemented in a variety of experiments [103, 119]. Recently the decoherence properties of a double quantum dot tuned to contain only one electron were studied in detail [97]. A coherence time of about 7 ns was found at the charge degeneracy point using a quantum point contact as charge detector.

We start with a gate geometry proven to be tunable to the last electron [119] as starting point for our device design implementation. The corresponding resonator double-quantum dot sample is shown in Fig. C.7 (a). The resonator design is slightly modified in comparison to the design shown in Fig. 6.1. The coupling of the resonator to the microwave leads is increased. According to simulations the resonator should be overcoupled, which is beneficial for the signal to noise ratio. In addition the on-chip inductor is now fabricated on the other side of the resonator, so that the DC signals come from one side of the chip and the microwave signals come from the other side. This simplifies the bonding step in the fabrication process of the sample. The double quantum dot is shown in Fig. C.7 (b). It is orientated on the mesa such that it is possible to couple the left plunger gate to the resonator. This way we keep the specific coupling of the microwave signal to only one of the dots as discussed in chapter 6. The DC voltage on the left plunger gate is set via the on-chip inductor. The two plunger gates have extensions that partially cover the dots to increase the coupling strength between the resonator and the double quantum dot. This is expected to help in reaching the strong coupling regime. A nearby quantum point contact is implemented in the design as well, to be able to detect the last electron with charge detection techniques.

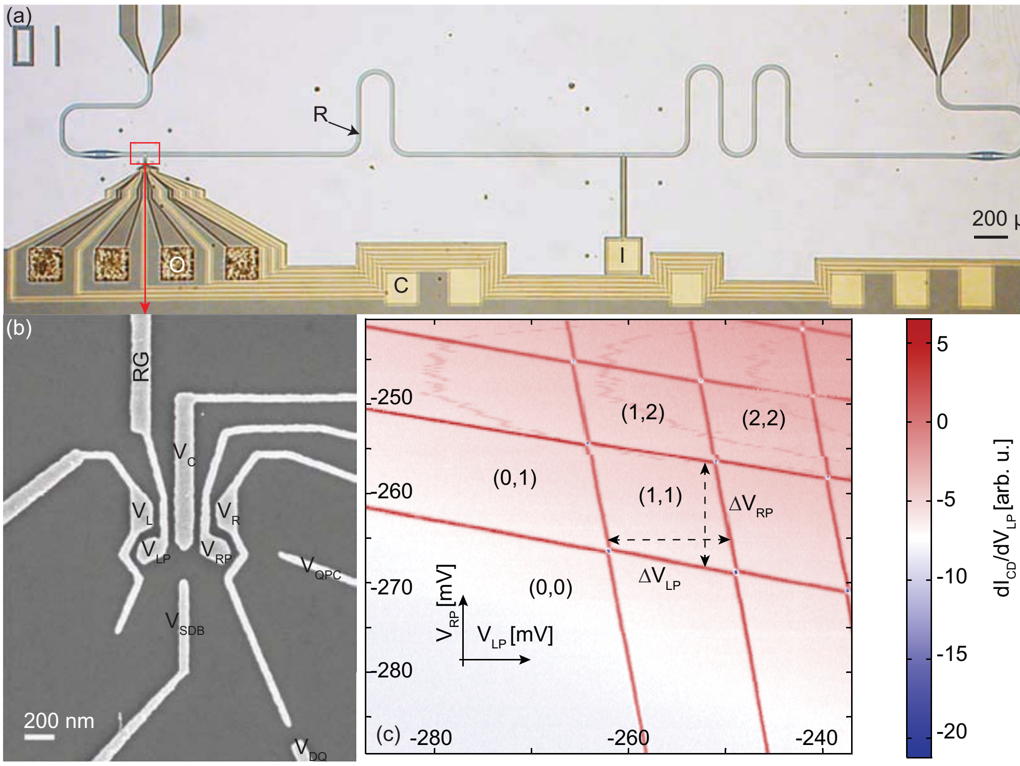

Figure C.7: Photography of a hybrid quantum device, displaying the microwave resonator (R) and the quantum dot circuit, consisting of a two dimensional electron gas (2DEG) (dark brown parts) with the four corresponding ohmic contacts (O). The golden squares mark topgate contacts (C). The center conductor of the resonator can be DC biased using an on-chip inductor with the corresponding contact marked (I). (b) Scanning electron microscope picture of the double quantum dot structure and the nearby quantum point contact (QPC) tuned using the voltage V_{QPC}. The resonator gate (RG) connects the center conductor of the microwave resonator to the left plunger gate (LP). The other gate voltages are used to form the appropriate potential landscape for the double quantum dot. (c) Charge stability diagram of a similar double quantum dot structure as shown in (b) recorded with the nearby charge detector. The electron number within each hexagon is indicated by (M,N) for the (left, right) dot. Parts of (b) and (c) adapted from [120].

In Fig. C.7 the transconductance signal of the charge detector is plotted versus the two plunger gates for a similar sample as the one shown in Fig. C.7. Both dots could be emptied to the last electron as illustrated with the numbers (M,N) in the hexagons. However, we could not measure finite bias triangles. This indicates that the two plunger gates do not only change the electrostatic potential in the dots, but also decrease the tunnel coupling between the two quantum dots. The charge detector is sensitive to the occupation of an additional electron on the quantum dot. However, based on our measurements shown in Fig. C.7 (c) it is not possible to distinguish between a process where the electron only tunnels between the lead and the dot back and forth and a process where the electron actually traverses the quantum dot. This problem could be solved in recent measurements by careful tuning of the tunnel barrier between the two dots [121].

To further study the influence the plunger gates have on the tunnel coupling, we form only the left quantum and investigate Coulomb diamonds as shown in Fig. C.8. By careful tuning it is possible to observe resonances to the leads down to the last electron at finite bias voltages. But the visibility of the outlines of the diamonds changes with electron number. This indicates that the tunnel coupling to the leads is changed. The resonance of the first electron with the source contact is visible (indicated with a white arrow in Fig. C.8) but not with the drain contact. For the transition between the third and the fourth electron only the resonance to the drain lead is observable (indicated with a black arrow). This indicates that the tunnel rates are modified by the change of the plunger gate voltage between these two situations, resulting in a non symmetric coupling. Therefore the complete outline of the diamonds is not visible in the charge detector signal. More details on the tunability of double quantum dots to the last electron can be found in Ref. [120], in which different double quantum dot designs are investigated and compared.

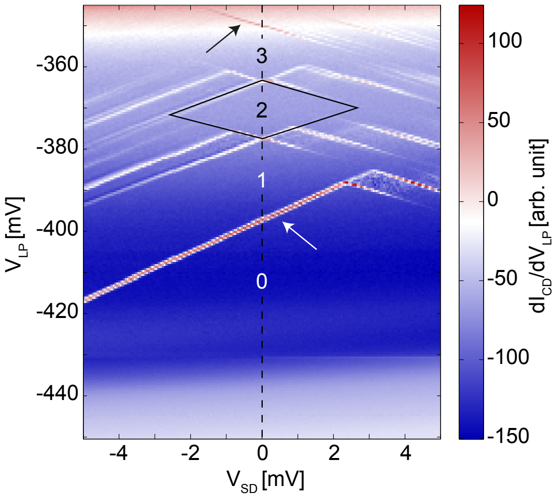

Figure C.8: Coulomb diamond measurements of a similar structure as shown in Fig. C.7(b) forming only the left quantum dot. The data is recorded with charge detection techniques. The electron number is indicated in the center of the diamonds and the outline of one diamond is highlighted. Figure partly adapted from Ref. [120].

D Fabrication recipe

In the following we give the explicit parameters that we used to fabricate quantum-dot resonator samples on shallow 2DEG wafers as shown in Fig. 6.1.

Resonator and Quantum Dot Process (with split gates)

1.0 Cleave and clean

	Cleave wafer without resist protection (9x8.2mm)	

2.0 Resist Spinning

	1 min acetone, US power 4, rinse in IPA and dry.	
	Prebake for 5 minutes 117-120 ºC, cool to RT.	
	Setup spinner: 5000/5/45.	
	Spin **AZ5214E**.	
	Touch corners of chip with swab of acetone to remove lumps at the corners. Remove resist from back of wafer as well if necessary.	
	Bake 120 s @ 90 ºC.	

3.0 Mesa Photolithography

	Warm up MA6 mask aligner (20 min to stabilize).	
	Measure UV intensity @ 365 nm.	
	Edge bead removal (EBR), align & expose substrate. MA6 **soft contact**, CP mode. 200 mJ/cm^2 @ 365 nm (typically 30-45 s).	
	Develop: AZ726MIF for ~40 s.	
	Visual inspection and removal of lumps at corners if necessary.	
	MA6 **vacuum** mode, 60 mJ/cm^2 @ 365 nm (typically 10-15 s).	
	Reversal bake 60 s @ 117 ºC (accurate temperature).	
	Flood expose 200 mJ/cm^2 @ 365 nm. Divide into 3 sessions, press **Multisession** on MA6, enter time for a **single** session (around 10-15s).	
	Develop: **AZ726MIF** for around 20 s.	

4.0 Mesa Etch

	Prepare fresh solution of H_2SO_4:H_2O_2:H_2O, 3:1:100.	
	Etch for 30s (should give 40nm etch depth).	
	Stop process in water, blow dry with N_2	
	Remove resist with DMSO @ 80 ºC, 20 mins.	
	Rinse chip in acetone then IPA, moving it well, dry.	

5.0 Ohmic Contacts

	1 min acetone, 10s US power 4, rinse in IPA and dry.	
	Spin as described above.	
	EBR, align and expose as above.	
	Develop: AZ726MIF for ~40 s.	
	Visual inspection, remove corner lumps.	
	MA 6 vacuum mode, 60 mJ/cm^2 @ 365 nm.	
	Bake 60 s @ 117 ºC.	

	Flood expose 200 mJ/cm^2 @ 365 nm, divided into 3 sessions.	
	Develop: AZ726MIF for ~20 s.	
	Do not plasma ash, it is totally unnecessary.	
	HCl dip 1 s, stopped in water, dry with N_2	
	Evaporation Plassys II Ge/Au/Ge/Au/Ni/Au. 15/40/15/40/35/100.	

6.0 Liftoff

	20 min DMSO @ 80 ºC.	
	Blow metal away with pipette – it should come easily away in one piece from each chip.	
	Leave for further 5 min in hot DMSO.	
	10 s ultrasound, power 2, in clean acetone, rinse in IPA.	
	Put chips in petri dish of IPA and check in cheap microscope for remaining metal flakes before drying.	

7.0 Anneal

	Use slow annealer due to the large chip size.	
	Set temperature 430 ºC for 10s when desired temperature is reached, overshoot of temperature up to ~445 ºC, forming gas pressure 0.5 bar, flow 9 cuft/hr.	
	Test contacts with probe station (**without** light in the room).	

8.0 Gates

	1 min Acetone, 10s US power 4, rinse in IPA and dry.	
	Spin as described above.	
	EBR, align and expose as above.	
	Develop: AZ726MIF for ~40 s.	
	Visual inspection, remove corner lumps.	
	MA6 vacuum mode, 60 mJ/cm^2 @ 365 nm.	
	Bake 60 s @ 117 ºC.	
	Flood expose 200 mJ/cm^2 @ 365 nm, divided into three sessions.	
	Develop: AZ726MIF for ~20 s.	
	Visual check and further develop if necessary.	
	Evaporate Ti/Au 5/55nm on Plassys II, at 1/5 A/s rates.	
	Liftoff in hot DMSO as before.	

9.0 E-beam lithography of inductors and alignment marks

	Bake 5 min @ 120 ºC.	
	Check spinner bowl is not strongly contaminated with photoresist, and replace otherwise.	
	Spin **PMMA:EL 4:1** 5000/5/45.	
	Remove resist from back of chip with acetone/swab if necessary.	
	Bake 5 min @ 180 ºC.	
	EBL. 30 kV acceleration, 10 um aperture. Dose 3.0 for	

	250 nm width inductor line and alignment marks. Polygons dose range 2.25-2.75 depending on size. Write field 500 um, step size 8 nm for inductor, WF 100 um, step size 4 nm for alignment marks. Contamination dot diameter 50 nm should be achievable.	
	Develop 50s in 3:1 IPA:MIBK, rinse in IPA.	
	Evap. Ti/Au 3/40nm on Plassys II at 1 / 2.5 A/s rates.	
	Liftoff in hot DMSO as before, taking extra care to check for remaining metal flakes before drying, since PMMA is much harder to remove than photoresist.	

10.0 Resonator processing

	1 min Acetone, 10s US power 4, rinse in IPA and dry.	
	Spin as described above.	
	EBR, align and expose as above.	
	Develop: AZ726MIF for ~40 s.	
	Visual inspection, remove corner lumps.	
	MA6 vacuum mode, 60 mJ/cm^2 @ 365 nm.	
	Bake 60 s @ 117 ºC.	
	Flood expose 200 mJ/cm^2 @ 365 nm, divided into three sessions.	
	Develop: AZ726MIF for ~20 s.	
	Visual check and further develop if necessary.	
	Evap. Ti/Al 3/200nm on Plassys II, at 1/5 A/s rates.	
	Liftoff in hot DMSO as before.	

11.0 E-beam lithography of split gates to define quantum dots

	Bake 5 min @ 120 ºC.	
	Check spinner bowl is not strongly contaminated with photoresist, and replace otherwise.	
	Spin **PMMA:EL 1:1** 5000/5/45.	
	Remove resist from back of chip with acetone/swab if necessary.	
	Bake 5 min @ 180 ºC.	
	EBL. 30 kV acceleration, 10 um aperture. Dose 4.75 for single pixel line tunnel barriers. Polygons dose range 1.75-2.3 depending on size. WF 100 um, step size 4 nm. Contamination dot diameter 25 nm should be achievable.	
	Develop 50s in 3:1 IPA:MIBK, rinse in IPA.	
	Evap. Ti/Au 3/25nm on Plassys II, at 1/1 A/s rates.	
	Liftoff in hot DMSO as before, again taking care to check for remaining flakes due to PMMA liftoff.	

Publications

Publications relevant for the thesis:

- **Quantum dot admittance probed at microwave frequencies with an on-chip resonator**
  T. Frey, P. J. Leek, M. Beck, J. Faist, A. Wallraff, K. Ensslin, T. Ihn, M. Büttiker
  Phys. Rev. B **86**, 115303 (2012)

- **Dipole coupling of a double quantum dot to a microwave resonator**
  T. Frey, P. J. Leek, M. Beck, A. Blais, T. Ihn, K. Ensslin, A. Wallraff
  Phys. Rev. Lett. **108**, 046807 (2012)

- **Characterization of a microwave frequency resonator via a nearby quantum dot**
  T. Frey, P. J. Leek, M. Beck, K. Ensslin, A. Wallraff, T. Ihn
  Appl. Phys. Lett. **98**, 262105 (2011)

Contributions to other publications

- **Transport through a strongly coupled graphene quantum dot in perpendicular magnetic field**
  J. Güttinger, C. Stampfer, T. Frey, T. Ihn, K. Ensslin
  Nanoscale Research Letters, **6**, 253 (2011)

- **Spin States in Graphene Quantum Dots**
  J. Güttinger, T. Frey, C. Stampfer, T. Ihn, K. Ensslin
  Phys. Rev. Lett. **105**, 116801 (2010)

- **Graphene single-electron transistors**
  T. Ihn, J. Güttinger, F. Molitor, S. Schnez, E. Schurtenberger, A. Jacobsen, S. Hellmüller, T. Frey, S. Dröscher, C. Stampfer, K. Ensslin

Materials Today **13**, 44 (2010)

- **Graphene quantum dots in perpendicular magnetic fields**
  J. Güttinger, C. Stampfer, T. Frey, T. Ihn, K. Ensslin
  Physica Status Solidi B **246**, 2553 (2009)

- **Electron-Hole Crossover in Graphene Quantum Dots**
  J. Güttinger, C. Stampfer, F. Libisch, T. Frey, J. Burgdörfer, T. Ihn, K. Ensslin
  Phys. Rev. Lett. **103**, 046810 (2009)

Bibliography

[1] T. Ihn, *Semiconductor Nanostructures: Quantum States and Electronic Transport* (Oxford University Press, New York, 2010).

[2] W. G. van der Wiel, S. De Franceschi, J. M. Elzerman, T. Fujisawa, S. Tarucha, and L. P. Kouwenhoven, Rev. Mod. Phys. **75**, 1 (2002).

[3] R. Hanson, L. P. Kouwenhoven, J. R. Petta, S. Tarucha, and L. M. K. Vandersypen, Rev. Mod. Phys. **79**, 1217 (2007).

[4] L. Kouwenhoven, C. Marcus, P. McEuen, S. Tarucha, R. Westervelt, and N. Wingreen, in *Mesoscopic Electron Transport*, edited by L. Sohn, L. Kouwenhoven, and G. Schön (Kluwer, 1997), Advanced Study Institute.

[5] S. M. Reimann and M. Manninen, Rev. Mod. Phys. **74**, 1283 (2002).

[6] S. Tarucha, D. G. Austing, T. Honda, R. J. van der Hage, and L. P. Kouwenhoven, Phys. Rev. Lett. **77**, 3613 (1996).

[7] T. H. Oosterkamp, T. Fujisawa, W. G. van der Wiel, K. Ishibashi, R. V. Hijman, S. Tarucha, and L. P. Kouwenhoven, Nature **395**, 873 (1998).

[8] T. H. Oosterkamp, L. P. Kouwenhoven, A. E. A. Koolen, N. C. van der Vaart, and C. J. P. M. Harmans, Phys. Rev. Lett. **78**, 1536 (1997).

[9] J. M. Elzerman, R. Hanson, L. H. Willems van Beveren, B. Witkamp, L. M. K. Vandersypen, and L. P. Kouwenhoven, Nature **430**, 431 (2004).

[10] F. H. L. Koppens, C. Buizert, K. J. Tielrooij, I. T. Vink, K. C. Nowack, T. Meunier, L. P. Kouwenhoven, and L. M. K. Vandersypen, Nature **442**, 766 (2006).

[11] K. Ploog, Ann. Rev. Mater. Sci. **12**, 123 (1982).

[12] S. M. Dutra, *Cavity Quantum Electrodynamics: The Strange Theory of Light in a Box* (John Wiley & Sons, 2005).

[13] S. Haroche and J.-M. Raimond, *Exploring the Quantum: Atoms, Cavities, and Photons* (Oxford University Press, Oxford, 2006).

[14] A. Boca, R. Miller, K. M. Birnbaum, A. D. Boozer, J. McKeever, and H. J. Kimble, Phys. Rev. Lett. **93**, 233603 (2004).

[15] P. Goy, J. M. Raimond, M. Gross, and S. Haroche, Phys. Rev. Lett. **50**, 1903 (1983).

[16] Z. M. Wang, *Self-Assembled Quantum Dots: Lecture notes in nanoscale science and technology* (Springer, 2009).

[17] J. P. Reithmaier, G. Sek, A. Loffler, C. Hofmann, S. Kuhn, S. Reitzenstein, L. V. Keldysh, V. D. Kulakovskii, T. L. Reinecke, and A. Forchel, Nature **432**, 197 (2004).

[18] T. Yoshie, A. Scherer, J. Hendrickson, G. Khitrova, H. M. Gibbs, G. Rupper, C. Ell, O. B. Shchekin, and D. G. Deppe, Nature **432**, 200 (2004).

[19] A. Wallraff, D. I. Schuster, A. Blais, L. Frunzio, R.-S. Huang, J. Majer, S. Kumar, S. M. Girvin, and R. J. Schoelkopf, Nature **431**, 162 (2004).

[20] J. M. Chow, J. M. Gambetta, L. Tornberg, J. Koch, L. S. Bishop, A. A. Houck, B. R. Johnson, L. Frunzio, S. M. Girvin, and R. J. Schoelkopf, Phys. Rev. Lett. **102**, 090502 (2009).

[21] L. DiCarlo, J. M. Chow, J. M. Gambetta, L. S. Bishop, B. R. Johnson, D. I. Schuster, J. Majer, A. Blais, L. Frunzio, S. M. Girvin, et al., Nature **460**, 240 (2009).

[22] E. Lucero, R. Barends, Y. Chen, J. Kelly, M. Mariantoni, A. Megrant, P. O'Malley, D. Sank, A. Vainsencher, J. Wenner, et al., Nat Phys **8**, 719 (2012).

[23] A. Fedorov, L. Steffen, M. Baur, M. P. da Silva, and A. Wallraff, Nature **481**, 170 (2012).

[24] D. Bozyigit, C. Lang, L. Steffen, J. M. Fink, C. Eichler, M. Baur, R. Bianchetti, P. J. Leek, S. Filipp, M. P. da Silva, et al., Nat Phys **7**, 154 (2011).

[25] M. Field, C. G. Smith, M. Pepper, D. A. Ritchie, J. E. F. Frost, G. A. C. Jones, and D. G. Hasko, Phys. Rev. Lett. **70**, 1311 (1993).

[26] W. Lu, Z. Ji, L. Pfeiffer, K. W. West, and A. J. Rimberg, Nature **423**, 422 (2003).

[27] D. J. Reilly, C. M. Marcus, M. P. Hanson, and A. C. Gossard, Applied Physics Letters **91**, 162101 (2007).

[28] M. C. Cassidy, A. S. Dzurak, R. G. Clark, K. D. Petersson, I. Farrer, D. A. Ritchie, and C. G. Smith, Applied Physics Letters **91**, 222104 (2007).

[29] T. Müller, B. Küng, S. Hellmüller, P. Studerus, K. Ensslin, T. Ihn, M. Reinwald, and W. Wegscheider, Applied Physics Letters **97**, 202104 (2010).

[30] K. D. Petersson, C. G. Smith, D. Anderson, P. Atkinson, G. A. C. Jones, and D. A. Ritchie, Nano Letters **10**, 2789 (2010).

[31] *Nature insight: Quantum coherence*, vol. 453, 1003-1049 (2008).

[32] S. Amasha, K. MacLean, I. P. Radu, D. M. Zumbühl, M. A. Kastner, M. P. Hanson, and A. C. Gossard, Phys. Rev. Lett. **100**, 046803 (2008).

[33] H. Bluhm, S. Foletti, I. Neder, M. Rudner, D. Mahalu, V. Umansky, and A. Yacoby, Nat Phys **7**, 109 (2011).

[34] R. J. Schoelkopf and S. M. Girvin, Nature **451**, 664 (2008).

[35] J. Majer, J. M. Chow, J. M. Gambetta, J. Koch, B. R. Johnson, J. A. Schreier, L. Frunzio, D. I. Schuster, A. A. Houck, A. Wallraff, et al., Nature **449**, 443 (2007).

[36] L. Childress, A. S. Sørensen, and M. D. Lukin, Phys. Rev. A **69**, 042302 (2004).

[37] J. M. Taylor, H.-A. Engel, W. Dur, A. Yacoby, C. M. Marcus, P. Zoller, and M. D. Lukin, Nat Phys **1**, 177 (2005).

[38] G. Burkard and A. Imamoglu, Phys. Rev. B **74**, 041307 (2006).

[39] J. Taylor and M. Lukin, arXiv:cond-mat/0605144. (2006).

[40] J. J. Sakurai, *Modern Quantum Mechanics* (Addison-Wesley Publishing Company, Inc, New York, 1994).

[41] S. Gustavsson, R. Leturcq, T. Ihn, K. Ensslin, and A. C. Gossard, Journal of Applied Physics **105**, 122401 (2009).

[42] S. Gustavsson, R. Leturcq, M. Studer, T. Ihn, K. Ensslin, D. C. Driscoll, and A. C. Gossard, Nano Letters **8**, 2547 (2008).

[43] J. Gabelli, G. Fève, J.-M. Berroir, B. Plaçais, A. Cavanna, B. Etienne, Y. Jin, and D. C. Glattli, Science **313**, 499 (2006).

[44] C. Ciccarelli and A. J. Ferguson, New Journal of Physics **13**, 093015 (2011).

[45] Y. Nazarov and Y. Blanter, *Quantum Transport: Introduction to Nanoscience* (Cambridge University Press, New York, 2009).

[46] S. De Franceschi, S. Sasaki, J. M. Elzerman, W. G. van der Wiel, S. Tarucha, and L. P. Kouwenhoven, Phys. Rev. Lett. **86**, 878 (2001).

[47] R. E. Williams, *Modern GaAs Processing Methods* (Artech House Inc, 1990).

[48] R. N. Simons, *Coplanar Waveguide Circuits, Components and Systems* (John Wiley and Sons, Inc, New York, 2002).

[49] R. Held, S. Lüscher, T. Heinzel, K. Ensslin, and W. Wegscheider, Applied Physics Letters **75**, 1134 (1999).

[50] A. Fuhrer, A. Dorn, S. Lüscher, T. Heinzel, K. Ensslin, W. Wegscheider, and M. Bichler, Superlattices Microstruct. **31**, 19 (2002).

[51] F. R. Waugh, M. J. Berry, D. J. Mar, R. M. Westervelt, K. L. Campman, and A. C. Gossard, Phys. Rev. Lett. **75**, 705 (1995).

[52] C. Livermore, C. H. Crouch, R. M. Westervelt, K. L. Campman, and A. C. Gossard, Science **274**, 1332 (1996).

[53] F. R. Waugh, M. J. Berry, C. H. Crouch, C. Livermore, D. J. Mar, R. M. Westervelt, K. L. Campman, and A. C. Gossard, Phys. Rev. B **53**, 1413 (1996).

[54] F. Pobell, *Matter and Methods at Low Temperatures* (Springer, New York, 2007).

[55] D. M. Pozar, *Microwave Engineering* (Addison-Wesley Publishing Company, New York, 1993).

[56] D. I. Schuster, Ph.D. thesis, Yale University (2007).

[57] R. Bianchetti, Ph.D. thesis, ETH Zurich (2010).

[58] U. Tietze and C. Schenk, *Halbleiterschaltungstechnik* (Springer-Verlag, Berlin, 2002).

[59] S. Gustavsson, Ph.D. thesis, ETH Zurich (2008).

[60] M. Göppl, A. Fragner, M. Baur, R. Bianchetti, S. Filipp, J. M. Fink, P. J. Leek, G. Puebla, L. Steffen, and A. Wallraff, Journal of Applied Physics **104**, 113904 (2008).

[61] TX-Line, AWR Corporation (El Segundo, CA 90245).

[62] Maxwell12, ANSYS, Inc. (Canonsburg, PA 15317).

[63] H. Wang, M. Hofheinz, J. Wenner, M. Ansmann, R. C. Bialczak, M. Lenander, E. Lucero, M. Neeley, A. D. O'Connell, D. Sank, et al., Appl. Phys. Lett. **95**, 233508 (2009).

[64] C. Song, T. W. Heitmann, M. P. DeFeo, K. Yu, R. McDermott, M. Neeley, J. M. Martinis, and B. L. T. Plourde, Phys. Rev. B **79**, 174512 (2009).

[65] S. Marx, Master's thesis, Qudev group, ETH Zurich (2009).

[66] M. Jerger, S. Poletto, P. Macha, U. Hübner, A. Lukashenko, E. Il'ichev, and A. V. Ustinov, EPL **96**, 40012 (2011).

[67] B. A. Mazin, Ph.D. thesis, California Institute of Technology (2004).

[68] L. Hrivnák, Czechoslovak Journal of Physics B **34**, 436 (1984).

[69] D. P. Morgan, *Surface acoustic wave filters: with applications to electronic communications and signal processing* (Academic Press, Amsterdam, 2007).

[70] R. Barends, N. Vercruyssen, A. Endo, P. J. de Visser, T. Zijlstra, T. M. Klapwijk, P. Diener, S. J. C. Yates, and J. J. A. Baselmans, Appl. Phys. Lett. **97**, 023508 (2010).

[71] R. Barends, N. Vercruyssen, A. Endo, P. J. de Visser, T. Zijlstra, T. M. Klapwijk, and J. J. A. Baselmans, Appl. Phys. Lett. **97**, 033507 (2010).

[72] C. Rössler, T. Krähenmann, S. Baer, T. Ihn, K. Ensslin, C. Reichl, and W. Wegscheider, arXiv:1209.4447 (2012).

[73] C. Buizert, F. H. L. Koppens, M. Pioro-Ladrière, H.-P. Tranitz, I. T. Vink, S. Tarucha, W. Wegscheider, and L. M. K. Vandersypen, Phys. Rev. Lett. **101**, 226603 (2008).

[74] P. M. Mooney, Journal of Applied Physics **67**, R1 (1990).

[75] D. J. Chadi and K. J. Chang, Phys. Rev. B **39**, 10063 (1989).

[76] M. Pioro-Ladrière, J. H. Davies, A. R. Long, A. S. Sachrajda, L. Gaudreau, P. Zawadzki, J. Lapointe, J. Gupta, Z. Wasilewski, and S. Studenikin, Phys. Rev. B **72**, 115331 (2005).

[77] Y. V. Nazarov and Y. M. Blanter, *Quantum Transport: Introduction to Nanoscience* (Cambridge University Press, Cambridge, 2009).

[78] S. Datta, *Electronic transport in mesoscopic systems* (Cambridge University Press, New York, 1997).

[79] A. Prêtre, H. Thomas, and M. Büttiker, Phys. Rev. B **54**, 8130 (1996).

[80] M. Büttiker, Phys. Rev. B **46**, 12485 (1992).

[81] F. Schwabl, *Quantenmechanik - Eine Einführung* (Springer Verlag, Heidelberg, 2007).

[82] H. Bruus and K. Flensberg, *Many-Body Quantum Theory in Condensed Matter Physics: An Introduction* (Oxford University Press, New York, 2007).

[83] J. Wang, B. Wang, and H. Guo, Phys. Rev. B **75**, 155336 (2007).

[84] R. Schuster, E. Buks, M. Heiblum, D. Mahalu, V. Umansky, and H. Shtrikman, Nature (London) **385**, 417 (1997).

[85] S. E. Nigg, R. López, and M. Büttiker, Phys. Rev. Lett. **97**, 206804 (2006).

[86] C. Mora and K. L. Hur, Nat. Phys. **6**, 697 (2010).

[87] M. Filippone and C. Mora, arXiv:1205.2213 (2012).

[88] A. Blais, R.-S. Huang, A. Wallraff, S. M. Girvin, and R. J. Schoelkopf, Physical Review A **69**, 062320 (2004).

[89] T. Hayashi, T. Fujisawa, H. D. Cheong, Y. H. Jeong, and Y. Hirayama, Phys. Rev. Lett. **91**, 226804 (2003).

[90] F. Beaudoin, J. M. Gambetta, and A. Blais, Phys. Rev. A **84**, 043832 (2011).

[91] E. Jaynes and F. Cummings, Proceedings of the IEEE **51**, 89 (1963).

[92] D. Walls and G. Milburn, *Quantum Optics* (Springer Verlag, Berlin, 1994).

[93] H.-P. Breuer and F. Petruccione, *The theory of open quantum systems* (Oxford University Press, 2002).

[94] T. Itakura and Y. Tokura, Phys. Rev. B **67**, 195320 (2003).

[95] S. Vorojtsov, E. R. Mucciolo, and H. U. Baranger, Phys. Rev. B **71**, 205322 (2005).

[96] B. Abel and F. Marquardt, Phys. Rev. B **78**, 201302 (2008).

[97] K. D. Petersson, J. R. Petta, H. Lu, and A. C. Gossard, Phys. Rev. Lett. **105**, 246804 (2010).

[98] D. C. B. Valente, E. R. Mucciolo, and F. K. Wilhelm, Phys. Rev. B **82**, 125302 (2010).

[99] I. V. Yurkevich, J. Baldwin, I. V. Lerner, and B. L. Altshuler, Phys. Rev. B **81**, 121305 (2010).

[100] R. J. Schoelkopf, A. A. Clerk, S. M. Girvin, K. W. Lehnert, and M. H. Devoret, cond-mat/0210247 (2002).

[101] J. M. Martinis, S. Nam, J. Aumentado, K. M. Lang, and C. Urbina, Phys. Rev. B **67**, 094510 (2003).

[102] A. Wallraff, D. I. Schuster, A. Blais, J. M. Gambetta, J. Schreier, L. Frunzio, M. H. Devoret, S. M. Girvin, and R. J. Schoelkopf, Phys. Rev. Lett. **99**, 050501 (2007).

[103] J. R. Petta, A. C. Johnson, C. M. Marcus, M. P. Hanson, and A. C. Gossard, Phys. Rev. Lett. **93**, 186802 (2004).

[104] D. I. Schuster, A. Wallraff, A. Blais, L. Frunzio, R.-S. Huang, J. Majer, S. M. Girvin, and R. J. Schoelkopf, Phys. Rev. Lett. **94**, 123602 (2005).

[105] L. S. Bishop, J. M. Chow, J. Koch, A. A. Houck, M. H. Devoret, E. Thuneberg, S. M. Girvin, and R. J. Schoelkopf, Nat. Phys. **5**, 105 (2009).

[106] T. Frey, P. J. Leek, M. Beck, K. Ensslin, A. Wallraff, and T. Ihn, Applied Physics Letters **98**, 262105 (2011).

[107] T. Frey, P. J. Leek, M. Beck, A. Blais, T. Ihn, K. Ensslin, and A. Wallraff, Physical Review Letters **108**, 046807 (2012).

[108] T. Frey, P. J. Leek, M. Beck, J. Faist, A. Wallraff, K. Ensslin, T. Ihn, and M. Büttiker, Phys. Rev. B **86**, 115303 (2012).

[109] M. R. Delbecq, V. Schmitt, F. D. Parmentier, N. Roch, J. J. Viennot, G. Fève, B. Huard, C. Mora, A. Cottet, and T. Kontos, Phys. Rev. Lett. **107**, 256804 (2011).

[110] H. Toida, T. Nakajima, and S. Komiyama, arXiv:1206.0674v1 (2012).

[111] K. D. Petersson, L. W. McFaul, M. D. Schroer, M. Jung, J. M. Taylor, A. A. Houck, and J. R. Petta, arXiv:1205.6767v1 (2012).

[112] P.-Q. Jin, M. Marthaler, J. H. Cole, A. Shnirman, and G. Schön, Phys. Rev. B **84**, 035322 (2011).

[113] A. Cottet and T. Kontos, Phys. Rev. Lett. **105**, 160502 (2010).

[114] M. Trif, V. N. Golovach, and D. Loss, Phys. Rev. B **77**, 045434 (2008).

[115] P.-Q. Jin, M. Marthaler, A. Shnirman, and G. Schön, Phys. Rev. Lett. **108**, 190506 (2012).

[116] M. Reznikov, M. Heiblum, H. Shtrikman, and D. Mahalu, Phys. Rev. Lett. **75**, 3340 (1995).

[117] A. Kumar, L. Saminadayar, D. C. Glattli, Y. Jin, and B. Etienne, Phys. Rev. Lett. **76**, 2778 (1996).

[118] D. Taubert, Ph.D. thesis, Ludwig-Maximilians-Universität München (2011).

[119] J. M. Elzerman, R. Hanson, J. S. Greidanus, L. H. W. van Beveren, S. D. Franceschi, L. M. K. Vandersypen, S. Tarucha, and L. P. Kouwenhoven, Phys. Rev. B **67**, 161308 (2003).

[120] A. Stockklauser, Master's thesis, Qudev group, ETH Zurich (2012).

[121] D.-D. Jarausch, Master's thesis, Qudev group, ETH Zurich (2013).

Acknowledgements

I would like to thank my advisory board consisting of Prof. Thomas Ihn, Prof. Klaus Ensslin and Prof. Andreas Wallraff for giving me the opportunity to start and work on this joint research project, combining superconducting circuits with semiconductor nanostructures. I appreciated their constant support, the freedom to develop and test my own ideas and the many fruitful and detailed discussions that we had during my time as a Ph.D. student in the two groups.

I would like to thank Prof. Gerd Schön from Karlsruhe for reading my thesis and being part of my exam committee.

A special thank goes to Peter Leek for supervising me and all the hard effort he invested to bring the project forward. I benefited a lot from him teaching me fabrication tricks and sharing his microwave experience with me. He was always a great source of ideas but also open for my suggestions and willing to discuss them in detail with me. Outside of the lab I enjoyed his company as well and I will always remember the barbecue parties that he organized in his garden.

I would like to thank the two theoreticians Prof. Alexandre Blais and Prof. Markus Büttiker for being interested in my project, discussing the data with me and helping me to understand the theory behind my experiments.

Fabricating the quantum dots for my project would not have been possible without the excellent wafers grown and provided by Mattias Beck from the Faist group who I thank a lot for his effort.

My deep gratitude goes to Paul Studerus for teaching me many things about electronics and always having a good idea for an electronic circuit that helped me to perform the measurements. Beside that I really enjoyed a lot our weekly common lunch breaks and the interesting discussions about all kinds of topics that we had.

I would also like to thank Cecil Barengo for his support in the lab with technical tasks and his hints on Chinese medicine against colds or back pain.

For my measurement I shared a dilution fridge with Stephan Bär and Clemens Rössler who conducted their experiments in the same system and I like to thank them for the good atmosphere we had in the lab and the common work we performed to maintain B15 and the corresponding equipment.

Gaby Strahm was always very helpful with all the administrative tasks that I faced during my work and it was always very interesting to talk to her about all her journeys and getting tips where it's nice to go.

Claudia Vinzens also helped me with all kinds of administrative stuff. In addition

Claudia cares a lot about the Ph.D. students in Klaus’ group, she always cheered me up when I came to her office and we had many nice conversations during the last years. She improves the working atmosphere in the group a lot. Thank you so much for all.

During a part of my time as a Ph.D. student I shared an office with Yashar Komijani and I enjoyed the great atmosphere we had in the office and the many interesting discussions. Thomas Müller was always a very helpful person in the lab, eager to discuss about high frequency experiments and a very good volleyball player. It was always great fun to spend time with him. With Susanne Dröscher I went running many rounds along many paths in the forest around ETH Hönggerberg and I would like to thank her a lot for all the nice conversations about all kinds of topics we had and her positive mood that cheered me up when I was stuck with my project.

A big thank goes to all my D17 officemates. It is simply ”close to super-awesome” to have a desk in D17 and I especially like to thank Arjan, Marek and Simon for all the great time that we had together in the office but also in our spare time. An additional special thank goes to Arjan for his never ending enthusiasm to take pictures under different angles and with different light sources and so on of my samples.

Towards the end of my time as a Ph.D. student I supervised two master students, Anna Stockklauser and David-Dominik Jarausch. I would like to thank them for their work and the many questions they asked that always helped me to check whether I understood the topic well enough myself to be able to explain it.

I would also like to thank all the members of the nanophysics and qudev group for creating a nice working atmosphere.

Finally I would like to thank my family a lot for being very supportive during all the years and listening to all my stories about failed fabrication steps, broken equipment and not working measurements and assuring me all the time that things will turn out to be good in the end.